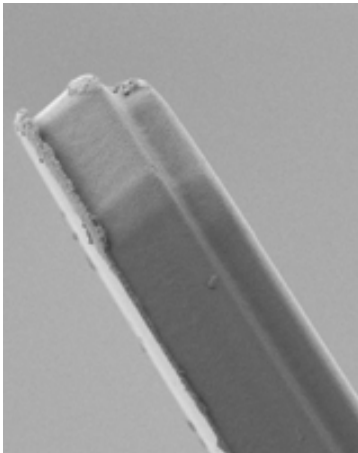


Chapter 4. OPTOTHERMAL ACTUATORS



Polymers have the capability to be functionalized and modified, as it has been already discussed. In previous chapters, the doping with inorganic nanoparticles has shown to improve mechanical properties and stability of the fabricated devices. Using the doping with other polymers it is also possible to tune the properties of the material. An example is shown using a black-colored polymer in order to change the color of the epoxy-based resist, modifying the absorption spectrum in order to make the material sensitive to light in the visible. Using these polymers, opto-thermal actuators have been fabricated. A complete theoretical model has been developed in order to describe accurately the actuation technique and it has been used to determine the material properties of the modified polymers.

4.1 INTRODUCTION

Since their beginnings [1], Micro Electro Mechanical Systems (MEMS) have been gaining importance both in academic and industrial level. The main two applications [2] for MEMS involved the possibility to build micro-sensors and micro-actuators [3]. These two different systems are based in the transformation of one type of energy into another, which is more commonly known as transduction.

Sensors detect a signal that supplies energy to the device, e.g. thermal energy for thermometers, acoustic energy for microphones, gravitational energy for accelerometers, etc. That energy is transduced into another kind of energy, which in MEMS usually is mechanical energy, e.g. deflection of a thermo-couple, vibration of a membrane, displacement of an inertial mass, etc. Finally, that mechanical energy is generally again transduced in a readable type of energy, that generally is electric, e.g. piezoelectric effect, piezoresistive effect, voltage output in a photodiode detector, etc.

On the other hand, actuators receive a given active signal and they transduce it into mechanical energy, causing strains and stresses in the mechanical device and finally moving or applying forces to objects or other devices.

Therefore, for a sensor, the parameter that usually is taken to measure its quality is the so-called sensitivity, i.e. the ratio between the output and the input signal. On the other hand, for an actuator, there are two parameters that are important: the ratio between the final generated displacement and the input signal, and the ratio between the final generated force and the input signal. In this sense, there can be actuators able to generate huge forces but with small displacements or, in the other extreme, huge displacements with small forces [4].

4.1.1 Actuation techniques

Actuation at the micro scale and nanoscale is of high interest in different areas, e.g. the manipulation of micro-objects, cell manipulation, excitation of micro and nano resonators, etc. Different actuation mechanisms and materials are used in order to accomplish this. The most used techniques are piezoelectric, magnetic and thermal actuation.

In the first case, although very precise and fast elements have been achieved, the displacements are very small and the operational voltages are incredibly large. In addition, they present an inherent difficulty when trying to integrate them into a device, given the fact that they involve the deposition of non-CMOS compatible materials that usually present a high difficulty to be

patterned. Some solutions have been found to achieve deposition of piezoelectric materials, e.g. sputtering or pulse laser deposition (PLD) of aluminum nitride (AlN), lead zirconate titanate (PZT), zinc oxide (ZnO), etc.; but the deposition conditions apply some constraints for the rest of the process flow that, together with the high operational voltages needed, are avoiding integrated piezoelectric actuation to spread. However, this is the most used technique as external, non-integrated, actuation.

Magnetic actuation is, at a certain extent, easier to integrate, given the fact that a standard conductive path is needed on the mechanical device in order to generate a force on it. The main drawback is that, apart from that conductive path, it is necessary to have an external magnetic field \vec{B} in order to create a Lorentz force. This technique has been used in order to actuate MEMS sensors [5], AFM probes [6] and all types of NEMS [7].

Finally, thermal actuation allows a real and easy integration in the device. The basis of this technique is the fundamental property of every material to change its volume when the temperature is changed, given by the coefficient of thermal expansion (CTE), or α (4.1).

$$\alpha \equiv \frac{1}{L} \frac{\partial L}{\partial T} \quad (4.1)$$

Therefore, whenever there is an increment in temperature, the material will change in length/volume (usually increasing) and mechanical stresses will be generated, as expressed by the well known *Hooke's law* which, in its one-dimensional form is given by (4.2)

$$\sigma_{th} = E \cdot \epsilon_{th} = E \cdot \frac{\Delta L}{L} = E \cdot \alpha \cdot \Delta T \quad (4.2)$$

where E is the Young's modulus of the material. From (4.2), it can be seen that, in principle, both high actuation stress and strain can be achieved by simply increase more the temperature, although that would lead to high power consumption and high operating energies.

Thermal actuation in the micro- and nano-scale can be achieved using electro-thermal effect, i.e. using resistances that dissipate power by Joule effect while current is passing through them; they become hot and therefore they heat the materials around [4, 8, 9]. Another option is optothermal actuation [10, 11]. When light is absorbed by a material, the energy can produce an internal change (that eventually could lead to an increase or decrease in volume [12]) or just an increase in temperature, which leads to the so-called optothermal actuation [10].

Electro-thermal effect is usually preferred because its integration is easier than its optical counterpart. Electro-thermal actuators can be included into robust and portable devices, whereas optical actuators suffer from misalignment problems that decrease their feasibility. On the other hand, light based actuation can be interesting from several points of view, as for example wireless actuation, easy scaling-down (it is not necessary to include a heating element on top of the mechanical element), low noise (no electromagnetic interference) and, most important, decoupling between electrical and mechanical fields and the possibility of being used in harsh environments [11].

4.1.2 Actuating materials

In any of the cases where thermal actuation is to be used, as it will be explained more in detail below, it is needed a contrast in CTE between the different materials that compose the actuator [13, 14]. In addition, for optothermal actuation, it is also necessary that the incident light is absorbed by the material itself, or no energetic transfer would occur.

Therefore, the material or materials (or at least its properties: CTE, absorption coefficient, Young's modulus,...) composing the actuator will be determining its performance. In fact, as it has been stated [15], the CTE is approximately proportional to the inverse of E . This means, from (4.2), that a compromise should be reached between the obtained output in deformation and in force. Polymeric materials are, in principle, a good option for thermal actuation, given the fact that their CTE is at least twice as large as that of other typical materials in microelectronics (metals). The main drawback that polymers present is its relatively low Young's modulus.

Therefore, if both large movement and forces are required, dedicated designs mixing polymers with other materials as metals or silicon must be realized [4]. However, when the application of large forces is not the most important characteristic, it is possible to use only polymers to build up the device. In addition, as it has been demonstrated in the previous chapter, polymers can be doped by organic or inorganic compounds in order to add some functionalities or special properties, as in this case could be the increase in the CTE or in the Young's modulus.

Up to now in this Thesis it has been described the processing and the fabrication of devices made out of a standard epoxy based photoresist; and also the processing and the fabrication of devices using a modified polymer by doping the standard epoxy based resist using nanoparticles. Both are cases of photostructurable materials, really convenient for micro- and nano-fabrication but, absorbance spectra for those materials present a huge drop around 400 nm, meaning that they remain almost transparent for visible and infrared radiations. As it has been commented, in

order to perform optical actuation, it is necessary to have a material absorbing light in the same wavelength as the light source is emitting. As the most common light sources for actuation are lasers and standard lasers can just be found in the range (500 nm – 10 μm), i.e. visible and IR; it is necessary to modify again the standard epoxy based resist to make it more sensitive to the wavelengths commented.

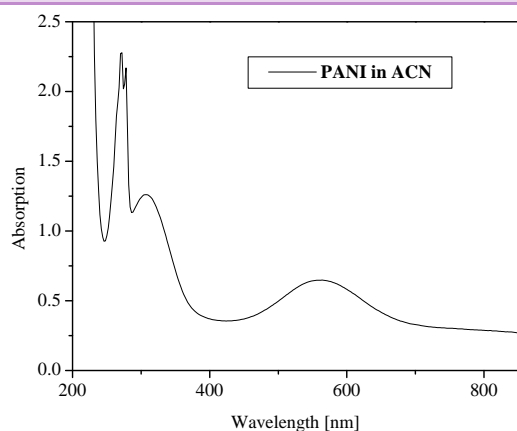
4.1.3 Polyaniline doped epoxy based resist

For a variety of applications a black colored resist is needed or desired, e.g. to adjust a second resist layer on a first layer or as protective layer to absorb undesired light (reflection). In order to change the color of the standard epoxy based resist that has been used up to now and turn it black, there are several possibilities, as the use of pigments or dyes.

In the first place, the use of pigments, e.g. carbon black pigments, is not the best choice given the fact that they are not soluble in the resist, even after treatments to cover the pigments by surfactants or polymeric coatings. As they are not soluble, the likelihood of sedimentation and aggregates formation is high.

Another possibility is the use of organic compounds that are solvent soluble in the resist, and that can confer the black tone to it. Polyaniline emeraldine base (PANI-EB) is an example of a possible organic dye, as can be seen in its absorbance spectrum (Figure 4.1).

Figure 4.1

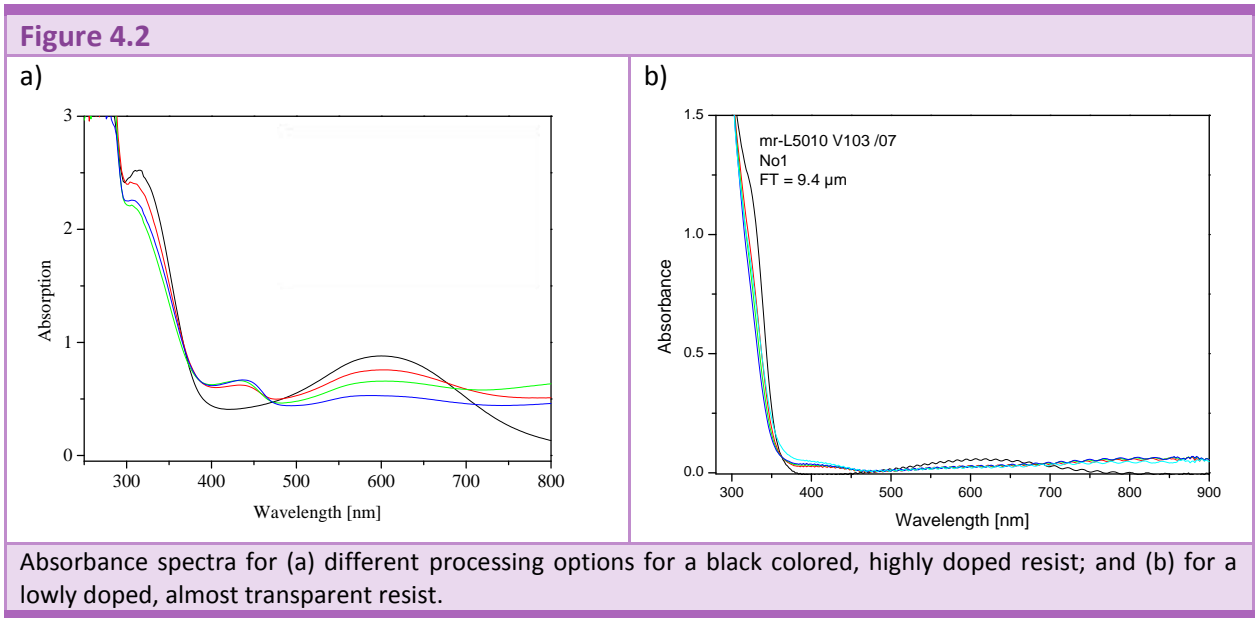


Absorbance spectrum for PANI-EB dissolved in acetonitrile (ACN).

Polyaniline (PANI) is a conductive polymer which has been used as one of the most promising synthetic metals during the last decades [16, 17]. It is very interesting because it has a relatively high electrical conductivity; good mechanical and environmental stability; and it can be

synthesized in a simple way with a very high yield. PANI can be found into two different configurations: a non-conductive but water and solvent soluble form PANI-EB (emeraldine base) and a conductive but much less soluble form PANI-ES (emeraldine salt).

Therefore, PANI-EB can act as the desired dye for the standard epoxy based resist. Its solubility in the typical solvents of the epoxy based resist can be improved by adding N-methylpyrrolidone (NMP), i.e. the best solvent for the PANI-EB. But this leads to difficulties during the filtration of the prepared solutions, i.e. PANI-EB aggregate formation is observed.



PANI-EB doped epoxy resist solutions have been prepared by *microresist technology* [18] with different concentrations of the dye. The filtered resist solutions were initially lithographically investigated in order to proof them as photostructurable. Changes during exposure and bake steps were observed. In all the cases, lithographic patterning was possible, but with different exposure doses. The layers, depending of the concentration of PANI-EB, can adopt different tones, from black colored to an almost transparent layer.

Therefore, during this chapter, a novel resist will be used, doped with PANI-EB, in order to accomplish a black colored polymer and hence demonstrate the possibility of the fabrication of optothermal actuators.

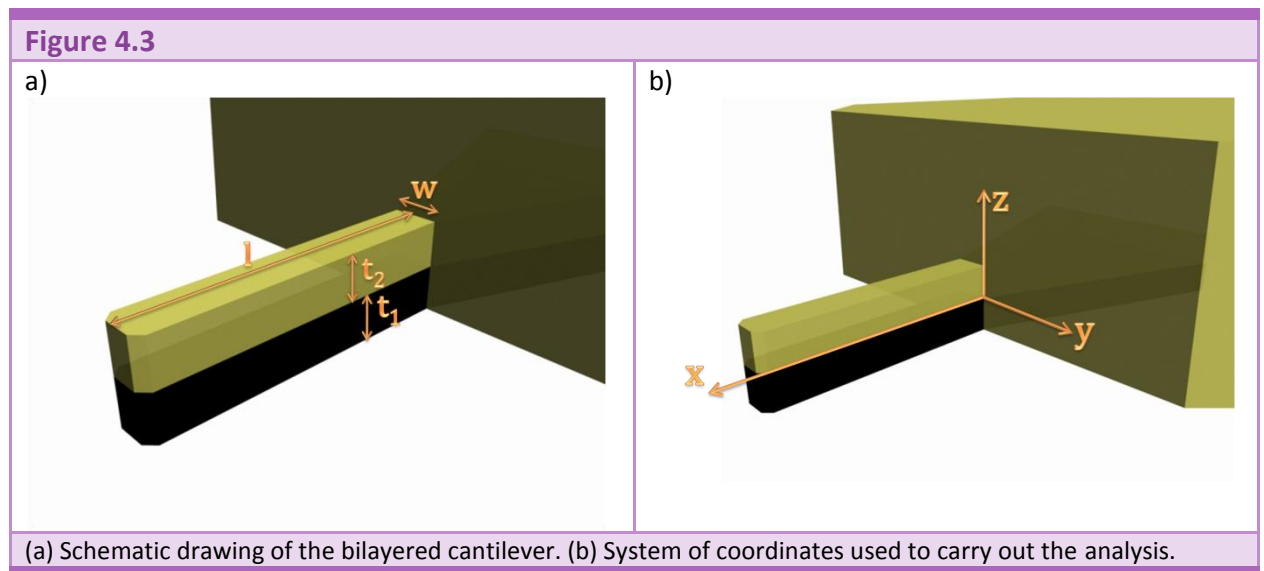
4.2 THEORETICAL STUDY

In this section, theoretical calculations, which are used to describe the mechanics of an optothermal cantilever, are presented. This analysis allows the analysis of the experimental results obtained as well as the optimization of the design and geometry.

As it has been commented, it is commonly used the bimetal effect to obtain thermal actuation in a cantilever. In order to do that, materials with different thermal expansion coefficients are necessary to form part of the structure of the lever. Therefore, the theoretical analysis will be focused in the properties and behavior of bi-layered cantilevers (simplest structure) and of tri-layered cantilevers.

4.2.1 Basic mechanics for a multi-layered structure

Although cantilevers are one of the simplest geometries one can ever think of, they have demonstrated an enormous versatility as mechanical sensors for different applications [19-27]. In order to characterize this mechanical structure, generally two parameters are studied and calculated, namely the elastic constant (k) and the resonance frequency (f), the first two parameters that will be calculated.



Let us consider a cantilever with a rectangular cross section that is kept constant all over the length of the structure and that it is formed by three layers of different materials (see Figure 4.3.a). Let us be t_1 , t_2 (in our case polymers) and t_m (in our case metal) the thicknesses of each of the materials, w the width and l the length of the structure, as it is shown in the Figure 4.3.a.

The origin of the system of coordinates is placed in the clamping edge of the lever, and in the separation between the two materials 1 and 2 (see Figure 4.3.b).

A general analysis of multi-layered cantilevers can be found elsewhere [14, 28-30]. Here, the steps to simply determine the characteristics and the deflection of such structures are presented.

Elementary beam theory states that any deformation of a cantilever beam can be considered as composed of two different effects: pure bending and pure extension. In the latter case, the whole beam is subjected to a constant elongation all over the cross section. In the first case, the deformation is linearly dependent with the distance to the so-called *structural neutral axis*, z_0 . This axis, therefore, is defined as the region that does not present any elongation for pure bending. So, in a general case, it can be written (4.3):

$$\epsilon(z) = \epsilon_0 + \chi(z - z_0) \quad (4.3)$$

Where z_0 is the position of the *structural neutral axis* with respect to the given reference system, the first summand stays from the pure elongation and the second term represents the pure bending. Note that the value of z_0 will depend on where the origin of coordinates has been placed and also the fact that, in a general case, the *structural neutral axis* will present a deformation (here it is possible to distinguish between *structural* and *real neutral axis*, being the latter an axis with zero final deformation).

To calculate the position of the structural neutral axis, a pure bending is considered and the equilibrium condition is applied (the total force must be zero at equilibrium), so it is possible to write (4.4) and (4.5), where $E(z)$ stands for the Young's modulus of the material that is located at a distance z of the origin of coordinates.

$$\int_{-t_1}^{t_2+t_m} \int_{-w(z)/2}^{w(z)/2} \sigma(z) dy dz = \int_{-t_1}^{t_2+t_m} \int_{-w(z)/2}^{w(z)/2} E(z)\epsilon(z) dy dz = 0 \quad (4.4)$$

$$\int_{-t_1}^{t_2+t_m} \int_{-w(z)/2}^{w(z)/2} E(z)\chi(z - z_0) dy dz = 0 \quad (4.5)$$

which, neglecting the trivial solution for $\chi = 0$, gives an expression for z_0 in the form of the equation (4.6):

$$z_0 = \frac{\int_{-t_1}^{t_2+t_m} \int_{\frac{-w(z)}{2}}^{\frac{w(z)}{2}} E(z) z dy dz}{\int_{-t_1}^{t_2+t_m} \int_{\frac{-w(z)}{2}}^{\frac{w(z)}{2}} E(z) dy dz} = \frac{1}{2} \cdot \frac{t_2^2 E_2 - t_1^2 E_1 + t_m (2t_2 + t_m) E_m}{t_1 E_1 + t_2 E_2 + t_m E_m} \quad (4.6)$$

where it has been taken into account the fact that the cross section is rectangular and the fact that the distribution of materials is the same shown in Figure 4.3.a. If the position of the axis is negative ($z_0 < 0$) it means that the neutral axis is below the origin; whereas if it is positive ($z_0 > 0$) it means that the neutral axis is above. Note that in this case (see Figure 4.3.a), the origin has been taken in the interface region between the two polymeric materials.

Once the neutral axis position has been calculated, the next step is to define the new *stiffness moment of inertia*. This parameter (EI) is defined by the equation (4.7):

$$EI = \int_{-t_1}^{t_2+t_m} \int_{-w(z)/2}^{w(z)/2} (z - z_0)^2 E(z) dy dz \quad (4.7)$$

which, in our case, yields (4.8):

$$EI = \frac{w}{12} \cdot \frac{t_2^4 E_2^2 + t_1^4 E_1^2 + t_m^4 E_m^2 + 2t_1 t_2 (2t_1^2 + 3t_1 t_2 + 2t_2^2) E_1 E_2 + 2t_m t_1 (2t_1^2 + 6t_1 t_2 + 6t_2^2 + 6t_m t_2 + 3t_1 t_m + 2t_m^2) E_1 E_m + 2t_m t_2 (2t_2^2 + 3t_m t_2 + 2t_m^2) E_2 E_m}{t_1 E_1 + t_2 E_2 + t_m E_m} \quad (4.8)$$

This expression (4.8) is present in all the calculations for the deformation of the cantilever, given the fact that the vertical deflection is calculated after integrating twice (4.9):

$$W''(x) = -\frac{M(x)}{EI} \quad (4.9)$$

where $M(x)$, or flexural moment, will be given by (4.10):

$$M(x) = \int_{-t_1}^{t_2+t_m} \int_{-w(z)/2}^{w(z)/2} (z - z_0) E(z) \epsilon(z) dy dz \quad (4.10)$$

Therefore, the expression (4.8) allows us to calculate the elastic constant of the cantilever itself, which will be given by (4.11):

$$k = \frac{3EI}{l^3} \quad (4.11)$$

In addition, this expression allows calculating the resonant frequencies of the transversal vibration modes of the lever:

$$f_n = \frac{c_n}{2\pi} \cdot \sqrt{\frac{12EI}{(\rho_1 t_1 + \rho_2 t_2 + \rho_m t_m) l^4}} \quad (4.12)$$

where c_n is different for each mode:

$$c_1 = 1.015; c_2 = 6.36; c_n = \frac{(2n + 1)^2 \pi^2}{8\sqrt{3}} \text{ for } n > 2 \quad (4.13)$$

4.2.1.1 Thin metal layer

The expression (4.8) can be simplified if the metal layer is very thin, i.e. $t_m \ll t_1, t_2$. In such a case, terms with powers of t_m higher than 1, can be neglected with respect to the rest:

$$EI = \frac{w}{12} \cdot \frac{t_2^4 E_2^2 + t_1^4 E_1^2 + 2t_1 t_2 (2t_1^2 + 3t_1 t_2 + 2t_2^2) E_1 E_2 + 2t_m t_1 (2t_1^2 + 6t_1 t_2 + 6t_2^2) E_1 E_m + 4t_m t_2^3 E_2 E_m}{t_1 E_1 + t_2 E_2 + t_m E_m} \quad (4.14)$$

The linear terms in t_m could also be neglected but, given the fact that the Young's modulus of the metal can be much larger than that of the polymers (around 40 times), it is better to keep them in the expression.

4.2.1.2 Bi-layered structure

In the case that the metal layer is not present in the cantilever, the simplification is even more important, yielding finally:

$$EI = \frac{w}{12} \cdot \frac{t_2^4 E_2^2 + t_1^4 E_1^2 + 2t_1 t_2 (2t_1^2 + 3t_1 t_2 + 2t_2^2) E_1 E_2}{t_1 E_1 + t_2 E_2} \quad (4.15)$$

And also:

$$f_n = \frac{c_n}{2\pi} \cdot \sqrt{\frac{12EI}{(\rho_1 t_1 + \rho_2 t_2) l^4}} \quad (4.16)$$

4.2.2 Deflection due to thermal expansion

As it has been commented before, every material has a coefficient of thermal expansion (CTE), which means that there is a change in size when the temperature is also changing (4.1). Therefore, if a cantilever is formed by several materials (generally each of them with a different CTE, a part of the beam will expand, whereas others will contract, causing an overall bending of the lever [13, 14].

In order to calculate the bending, it will be necessary to compute the flexural moment, given by (4.10), taking into account that the strains are thermal, i.e. they are given by (4.1), and then it is possible to write (4.17)

$$M(x) = \frac{w \cdot \Delta T(x)}{2} \cdot \frac{E_1 E_2 (\alpha_2 - \alpha_1) t_1 t_2 (t_1 + t_2) + E_m E_2 (\alpha_m - \alpha_2) t_m t_2 (t_m + t_2) + E_1 E_m (\alpha_m - \alpha_1) t_1 t_m (t_1 + 2t_2 + t_m)}{t_1 E_1 + t_2 E_2 + t_m E_m} \quad (4.17)$$

Note that in this case, the temperature has been considered independent of (y, z) . This approximation will be justified later. In the most general case, the increment in temperature $\Delta T(x)$ will depend on the position of the cantilever. As this is the only non-constant part of (4.17), it is convenient to rewrite it in the following manner:

$$M(x) = QM \cdot \Delta T(x) \quad (4.18)$$

Where QM is the so-called quasi-momentum and it depends just on the geometry of the cantilever and on the properties of the materials, being useful in order to have some design

rules for the lever. Then, the curvature of the cantilever is known by combining (4.8), (4.9) and (4.17):

$$W''(x) = -\frac{QM}{EI} \cdot \Delta T(x) \quad (4.19)$$

And hence, once the temperature distribution is known, the deflection can be calculated, by integrating twice the expression (4.19) and applying the boundary conditions for a clamped-free beam, that are:

$$W(x=0) = 0; W'(x=0) = 0 \quad (4.20)$$

4.2.2.1 Constant temperature

Let us consider in the first place that the structure is submerged in a thermal bath at a temperature ΔT above room temperature. In this situation, provided the thermodynamic equilibrium has been reached, the whole cantilever is at constant temperature, the same than the one in the thermal bath, and the integral of (4.19) is:

$$W(x) = -\frac{QM}{2EI} \cdot \Delta T \cdot x^2 \quad (4.21)$$

4.2.2.2 Rectangular distribution of the temperature

As a second example for temperature distribution, let us consider that the increment is zero for most of the cantilever excepting a zone centered in x_0 and of length λ , where the increment is constant (see Figure 4.4.a). In other words:

$$\Delta T(x) = \Delta T_0 \cdot \left(H\left(x - x_0 + \frac{\lambda}{2}\right) - H\left(x - x_0 - \frac{\lambda}{2}\right) \right) = \begin{cases} 0 & 0 < x < x_0 - \frac{\lambda}{2} \\ \Delta T_0 & x_0 - \frac{\lambda}{2} < x < x_0 + \frac{\lambda}{2} \\ 0 & x_0 + \frac{\lambda}{2} < x < L \end{cases} \quad (4.22)$$

where $H(x)$ is the *Heaviside function*. In this case, the deflection of the cantilever is given by:

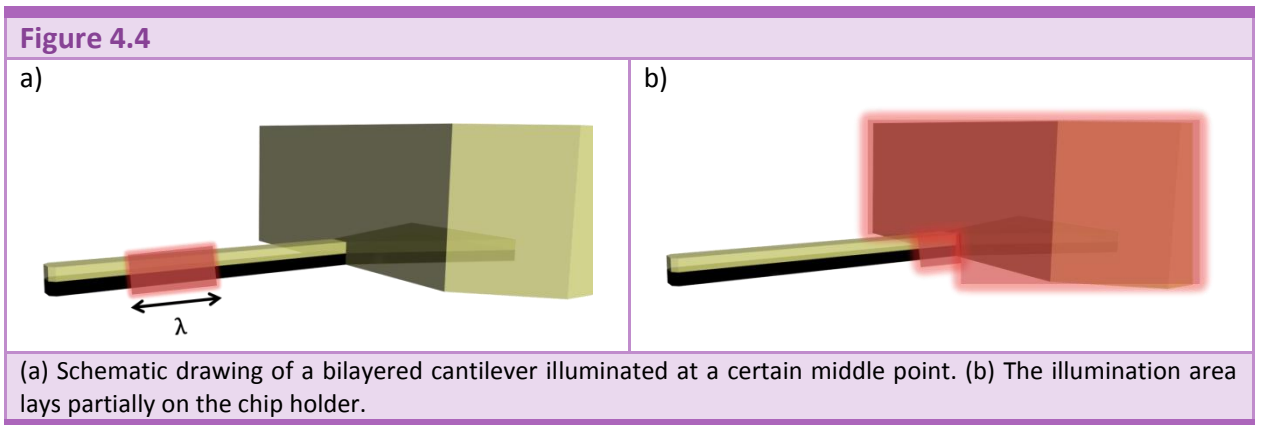
$$W(x) = \begin{cases} 0 & 0 < x < x_0 - \frac{\lambda}{2} \\ -\frac{QM}{2EI} \cdot \Delta T_0 \cdot \left(x - x_0 + \frac{\lambda}{2}\right)^2 & x_0 - \frac{\lambda}{2} < x < x_0 + \frac{\lambda}{2} \\ -\frac{QM}{EI} \cdot \Delta T_0 \cdot \lambda \cdot (x - x_0) & x_0 + \frac{\lambda}{2} < x < L \end{cases} \quad (4.23)$$

It is clear from (4.23) that the final deformation of the cantilever will depend on the length of the hot region (λ) and on the position (x_0). One could imagine what would happen if the hot region would come closer to the clamping edge (reducing x_0): eventually, part of the hot region would lie on the holder of the chip (when $x_0 < \frac{\lambda}{2}$), hence the temperature distribution would be:

$$\Delta T(x) = \Delta T_0 \cdot \left(1 - H\left(x - x_0 - \frac{\lambda}{2}\right)\right) = \begin{cases} \Delta T_0 & 0 < x < x_0 + \frac{\lambda}{2} \\ 0 & x_0 + \frac{\lambda}{2} < x < L \end{cases} \quad (4.24)$$

where $x_0 + \frac{\lambda}{2}$ is the length of the region of the lever which is at a higher temperature, and therefore the deflection:

$$W(x) = \begin{cases} -\frac{QM}{2EI} \cdot \Delta T_0 \cdot x^2 & 0 < x < x_0 + \frac{\lambda}{2} \\ -\frac{QM}{EI} \cdot \Delta T_0 \cdot \left(x_0 + \frac{\lambda}{2}\right) \cdot \left(x - \frac{x_0}{2} + \frac{\lambda}{4}\right) & x_0 + \frac{\lambda}{2} < x < L \end{cases} \quad (4.25)$$



Finally, on the other extreme, it could happen that $x_0 > L - \frac{\lambda}{2}$, which would mean:

$$\Delta T(x) = \Delta T_0 \cdot H\left(x - x_0 - \frac{\lambda}{2}\right) = \begin{cases} 0 & 0 < x < x_0 - \frac{\lambda}{2} \\ \Delta T_0 & x_0 - \frac{\lambda}{2} < x < L \end{cases} \quad (4.26)$$

$$W(x) = \begin{cases} 0 & 0 < x < x_0 - \frac{\lambda}{2} \\ -\frac{QM}{EI} \cdot \Delta T_0 \cdot \left(x - x_0 + \frac{\lambda}{2}\right)^2 & x_0 - \frac{\lambda}{2} < x < L \end{cases} \quad (4.27)$$

4.2.2.3 Rectangular distribution of the incident power

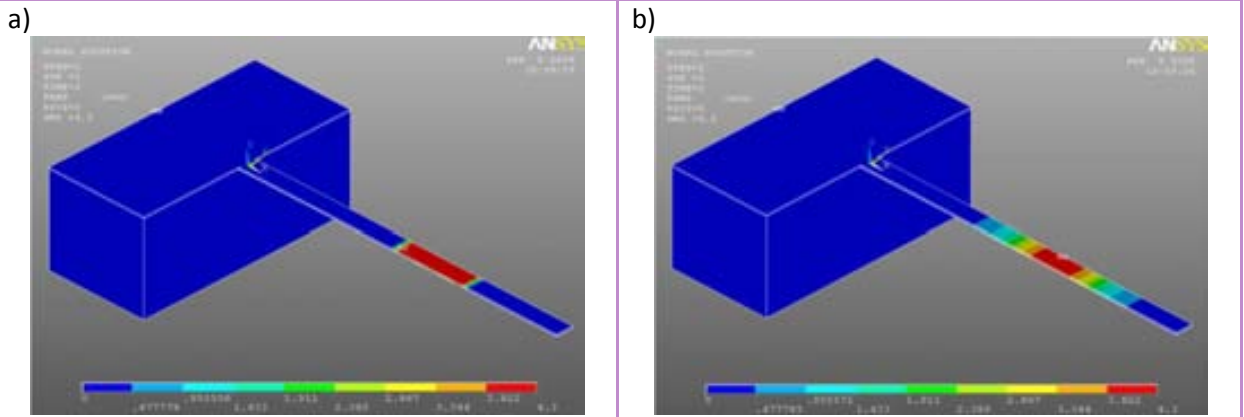
Let us consider finally the case in which the region that previously was supposed to have the increment in temperature, is now receiving an influx of energy from the exterior. In other words, the incident power density at a given point of the cantilever would be given by:

$$p_{in}(x) = \frac{P_{Abs}}{\lambda} \cdot \left(H\left(x - x_0 + \frac{\lambda}{2}\right) - H\left(x - x_0 - \frac{\lambda}{2}\right) \right) \quad (4.28)$$

The difference between this case and the previous one lies in the fact that, in the previous one, a rectangular distribution of temperatures was considered, what implies directly that the thermal conduction was neglected. That is a first approximation to the solution of the problem but, if a more accurate solution is required, it is necessary to take into account the heat conduction and hence the distribution of temperatures will be obtained. In Figure 4.5, the difference in the final distribution of temperatures between the two cases can be seen. Those are results of a FEM analysis performed with Ansys© in order to illustrate the difference.

As it has been commented, in this case the heat conduction must be taken into account. To do that, considering that the temperature will be constant all over each cross section (it will be justified later), it is possible to split the whole volume of the cantilever into slides of differential length and area equal to the cross-sectional area of the cantilever. For each one of those differential volumes, it is possible to write the heat conservation equation (incoming heat must be equal to outgoing heat plus heat losses plus heat invested in increasing temperature).

Figure 4.5



Distribution of the increment in temperature when (a) there is a rectangular distribution of temperatures or when there is a rectangular distribution in the incident power.

Let's consider the simplest case of a homogeneous cantilever (only one material). Then the heat transfer equation should be given by (4.29):

$$\rho c_p w \frac{\partial T}{\partial t} = \kappa t w \frac{\partial^2 T}{\partial x^2} - 2h(w + t)(T(x) - T_{room}) + p_{in}(x) \quad (4.29)$$

The term in the left hand side of the expression is the heat consumed in increasing the temperature, ρ is the mass density and c_p the specific heat of the material. The first term in the right hand side is the heat that is transferred by thermal conduction, where κ is the thermal conductivity of the material and when the term is positive it means that the differential of volume has more incoming than outgoing heat by conduction. The last term in the right part of the expression stays for the incident power in each differential of volume, which in this case will be given by (4.28). Finally, the mid-term of the right side is a term of losses. The cantilever is in contact with the air, so there will be some thermal conduction towards the air as well as some convection. To insert them correctly in the model would mean to include a multidimensional analysis. Instead, it has been considered that the losses depend on the temperature difference between the lever and the ambient temperature, multiplied by the contact area and by a loss parameter to be determined, h . As it can be seen in (4.29), the ambient temperature just means an offset of the variable, $T(x)$. Therefore, it is possible to solve the problem for $T_{room} = 0$ and then the results for $T(x)$ will have to be understood as an actual $\Delta T(x)$.

If a tri-layer cantilever is considered, the expression gets more complicated, but still remains the same [31-34]:

$$(\rho_1 c_{p,1} t_1 + \rho_2 c_{p,2} t_2 + \rho_m c_{p,m} t_m) w \frac{\partial T}{\partial t} = (\kappa_1 t_1 + \kappa_2 t_2 + \kappa_m t_m) w \frac{\partial^2 T}{\partial x^2} - 2h(w + t)T + p_{in}(x) \quad (4.30)$$

where t is the total thickness of the cantilever, and h is a parameter of losses, to be fitted experimentally. Once the stationary state has been reached, the time disappears from (4.30) and the differential equation stays:

$$\frac{\partial^2 T(x)}{\partial x^2} = \beta \cdot T(x) - \gamma(x) \quad (4.31)$$

With:

$$\beta = \frac{2h(w + t_1 + t_2 + t_m)}{(\kappa_1 t_1 + \kappa_2 t_2 + \kappa_m t_m)w}; \quad \gamma(x) = \frac{p_{in}(x)}{(\kappa_1 t_1 + \kappa_2 t_2 + \kappa_m t_m)w} \quad (4.32)$$

The solution for (4.31) must be found in three different regions, defined by $p_{in}(x)$. As that function is just different from zero around x_0 , and even there it is constant, it is possible to solve the homogeneous equation and add a particular solution for the inhomogeneous. Therefore, to find a particular solution for the equation (4.31) the first trial would be a constant function, ΔT_0 :

$$\Delta T_0 = -\frac{P_{Abs}}{2h\lambda(w + t_1 + t_2 + t_m)} \quad (4.33)$$

The general solution will be given by:

$$T(x) = \begin{cases} a_1 e^{\sqrt{\beta}x} + b_1 e^{-\sqrt{\beta}x} & 0 < x < x_0 - \frac{\lambda}{2} \\ \Delta T_0 + a_2 e^{\sqrt{\beta}x} + b_2 e^{-\sqrt{\beta}x} & x_0 - \frac{\lambda}{2} < x < x_0 + \frac{\lambda}{2} \\ a_3 e^{\sqrt{\beta}x} + b_3 e^{-\sqrt{\beta}x} & x_0 + \frac{\lambda}{2} < x < L \end{cases} \quad (4.34)$$

And then it is necessary to apply the boundary conditions, which would be continuity and derivability of the function in the boundaries between regions; the holder is considered as a thermal reservoir (no increase in temperature) and, at the free edge, the heat conducted to the outside must be equal to the heat lost:

$$T'(x=L) = -\frac{h(t_1 + t_2 + t_m)}{(\kappa_1 t_1 + \kappa_2 t_2 + \kappa_m t_m)} T(x=L) = -\delta \cdot T(x=L); \quad T(x=0) = 0 \quad (4.35)$$

where,

$$a_1 = a_2 + \frac{1}{2} \Delta T_0 e^{-\sqrt{\beta} \left(x_0 - \frac{\lambda}{2}\right)} \quad (4.36)$$

$$b_1 = -a_2 + \frac{1}{2} \Delta T_0 e^{-\sqrt{\beta} \left(x_0 - \frac{\lambda}{2}\right)} \quad (4.37)$$

$$b_2 = -a_2 - \Delta T_0 \cosh\left(\sqrt{\beta} \left(x_0 - \frac{\lambda}{2}\right)\right) \quad (4.38)$$

$$a_3 = a_2 + \frac{1}{2} \Delta T_0 e^{-\sqrt{\beta} \left(x_0 + \frac{\lambda}{2}\right)} \quad (4.39)$$

$$b_3 = -a_2 + \frac{1}{2} \Delta T_0 e^{\sqrt{\beta} \left(x_0 - \frac{\lambda}{2}\right)} \left(-1 + e^{\sqrt{\beta} \lambda} - e^{-2\sqrt{\beta} \left(x_0 - \frac{\lambda}{2}\right)}\right) \quad (4.40)$$

$$a_2 = \frac{-e^{-\sqrt{\beta} \left(x_0 + \frac{\lambda}{2}\right)} \Delta T_0 \left((\sqrt{\beta} - \delta) \left(e^{2x_0 \sqrt{\beta}} + e^{\sqrt{\beta} \lambda} - e^{2\sqrt{\beta} \left(x_0 + \frac{\lambda}{2}\right)}\right) + (\sqrt{\beta} + \delta) e^{2\sqrt{\beta} L}\right)}{2 \left(\sqrt{\beta} - \delta + e^{2L\sqrt{\beta}} (\sqrt{\beta} + \delta)\right)} \quad (4.41)$$

Taking into account (4.34) and (4.32), it is understandable that the parameter:

$$\beta^{\frac{1}{2}} = \sqrt{\frac{(\kappa_1 t_1 + \kappa_2 t_2 + \kappa_m t_m) w}{2h(w + t_1 + t_2 + t_m)}}$$

is governing the exponential decay of the temperature distribution in the stationary state. If typical values are applied (see below: Table 4.2 and experimental results), it is obtained that $\beta^{\frac{1}{2}}$ is in the order of, at least, a hundred microns, which is much larger than the typical thickness of the cantilevers, hence demonstrating the approximation of considering the system as one-dimensional, i.e. constant temperature in each cross section.

Integrating (4.34), it is possible to estimate the deflection of the lever:

$$W(x) = -\frac{QM}{EI\beta} \cdot \begin{cases} a_1 e^{\sqrt{\beta}x} + b_1 e^{-\sqrt{\beta}x} & 0 < x < x_0 - \frac{\lambda}{2} \\ \Delta T_0 \left(\frac{\beta}{2} \left(x - x_0 + \frac{\lambda}{2} \right)^2 + 1 \right) + a_2 e^{\sqrt{\beta}x} + b_2 e^{-\sqrt{\beta}x} & x_0 - \frac{\lambda}{2} < x < x_0 + \frac{\lambda}{2} \\ \Delta T_0 \beta \lambda (x - x_0) + a_3 e^{\sqrt{\beta}x} + b_3 e^{-\sqrt{\beta}x} & x_0 + \frac{\lambda}{2} < x < L \end{cases} \quad (4.42)$$

In the same way that, in the previous section, the cases in which the heated area was not completely in the cantilever have been considered, here it is also possible to do that:

$$T(x) = \begin{cases} \Delta T_0 + a'_1 e^{\sqrt{\beta}x} + b'_1 e^{-\sqrt{\beta}x} & 0 < x < x_0 + \frac{\lambda}{2} \\ a'_2 e^{\sqrt{\beta}x} + b'_2 e^{-\sqrt{\beta}x} & x_0 + \frac{\lambda}{2} < x < L \end{cases} \quad (4.43)$$

with:

$$a'_1 = -b'_2 + \frac{1}{2} \Delta T_0 \left(e^{\sqrt{\beta} \left(x_0 + \frac{\lambda}{2} \right)} - 2 \right) \quad (4.44)$$

$$a'_2 = -b'_2 + \Delta T_0 \left(\cosh \left(\sqrt{\beta} \left(x_0 + \frac{\lambda}{2} \right) \right) - 1 \right) \quad (4.45)$$

$$b'_1 = b'_2 - \frac{1}{2} \Delta T_0 e^{\sqrt{\beta} \left(x_0 + \frac{\lambda}{2} \right)} \quad (4.46)$$

$$b'_2 = \frac{\Delta T_0 (\sqrt{\beta} + \delta) e^{\sqrt{\beta} \left(2L - x_0 - \frac{\lambda}{2} \right)} \left(e^{\sqrt{\beta} \left(x_0 + \frac{\lambda}{2} \right)} - 1 \right)^2}{2 \left(\sqrt{\beta} - \delta + e^{2L\sqrt{\beta}} (\sqrt{\beta} + \delta) \right)} \quad (4.47)$$

which yields:

$$W(x) = -\frac{QM}{EI\beta} \cdot \begin{cases} \Delta T_0 \left(\frac{\beta}{2} x^2 + 1 \right) + a'_1 e^{\sqrt{\beta}x} + b'_1 e^{-\sqrt{\beta}x} & 0 < x < x_0 + \frac{\lambda}{2} \\ \frac{\beta \Delta T_0}{2} \left(x_0 + \frac{\lambda}{2} \right) \left(2x - x_0 - \frac{\lambda}{2} \right) + a'_2 e^{\sqrt{\beta}x} + b'_2 e^{-\sqrt{\beta}x} & x_0 + \frac{\lambda}{2} < x < L \end{cases} \quad (4.48)$$

Or, in the case that the laser is at the free edge of the cantilever:

$$T(x) = \begin{cases} a_1'' e^{\sqrt{\beta}x} + b_1'' e^{-\sqrt{\beta}x} & 0 < x < x_0 - \frac{\lambda}{2} \\ \Delta T_0 + a_2'' e^{\sqrt{\beta}x} + b_2'' e^{-\sqrt{\beta}x} & x_0 - \frac{\lambda}{2} < x < L \end{cases} \quad (4.49)$$

where:

$$a_1'' = -b_2'' - \frac{1}{2} \Delta T_0 e^{\sqrt{\beta}(x_0 - \frac{\lambda}{2})} \quad (4.50)$$

$$a_2'' = -b_2'' - \Delta T_0 \cosh\left(\sqrt{\beta}\left(x_0 - \frac{\lambda}{2}\right)\right) \quad (4.51)$$

$$b_1'' = b_2'' + \frac{1}{2} \Delta T_0 e^{\sqrt{\beta}(x_0 - \frac{\lambda}{2})} \quad (4.52)$$

$$b_2'' = -\frac{\Delta T_0 e^{\sqrt{\beta}(L - x_0 + \frac{\lambda}{2})} \left(-2e^{\sqrt{\beta}(x_0 - \frac{\lambda}{2})} \delta + (\sqrt{\beta} + \delta) (e^{\sqrt{\beta}L} + e^{\sqrt{\beta}(L + 2x_0 - \lambda)}) \right)}{2(\sqrt{\beta} - \delta + e^{2L\sqrt{\beta}}(\sqrt{\beta} + \delta))} \quad (4.53)$$

which yields:

$$W(x) = -\frac{QM}{EI\beta} \cdot \begin{cases} a_1'' e^{\sqrt{\beta}x} + b_1'' e^{-\sqrt{\beta}x} & 0 < x < x_0 - \frac{\lambda}{2} \\ \Delta T_0 \left(\frac{\beta}{2} \left(x - x_0 + \frac{\lambda}{2} \right)^2 + 1 \right) + a_2'' e^{\sqrt{\beta}x} + b_2'' e^{-\sqrt{\beta}x} & x_0 - \frac{\lambda}{2} < x < L \end{cases} \quad (4.54)$$

4.2.3 Optothermal actuation

As it has been already commented previously, the final objective is to fabricate a polymeric optothermal actuator. The actuation technique will be based in the illumination of the cantilever by a laser focused at a distance x_0 from the clamping edge, and being the spot of the focused region a circle with a diameter λ .

This incident laser will penetrate into the polymeric materials of the cantilever, which will absorb part of the energy of the laser (depending on the absorbance coefficient for the laser wavelength). Therefore, just a part of the incident power will remain absorbed in the cantilever, causing the temperature to increase.

As it can easily be seen, in a first approximation, a system in which the lever is locally illuminated by a laser is analog to a system like the one previously explained, that is to say, a system where there is an incident power with a rectangular distribution.

In addition, as a simple model, it should be possible to consider a cantilever in which the temperature has a rectangular distribution, which simplifies enormously the analytic formulae for the deflection.

4.2.4 Design rules

If a device with a large actuation capability in strain is desired, the deflection of the cantilever must be maximized for a given input. In this case, it is possible to consider as input either an incident power or a temperature.

In any case, recalling all the expressions for the deflection of the cantilevers calculated previously ((4.21), (4.23), (4.25), (4.27), (4.42), (4.48) and (4.54)), it can be seen that, in order to maximize the deflection-input ratio, the quantities $\frac{QM}{EI}$ in the case of fixed temperature and $\frac{QM}{EI\beta}$ in the case of fixed incident power must be optimized.

The main problem at this point is the fact that the named quantities depend on so many parameters that can vary that a general optimization is hard to perform. In addition, usually there are some technological factors that already are limiting the value of some of them.

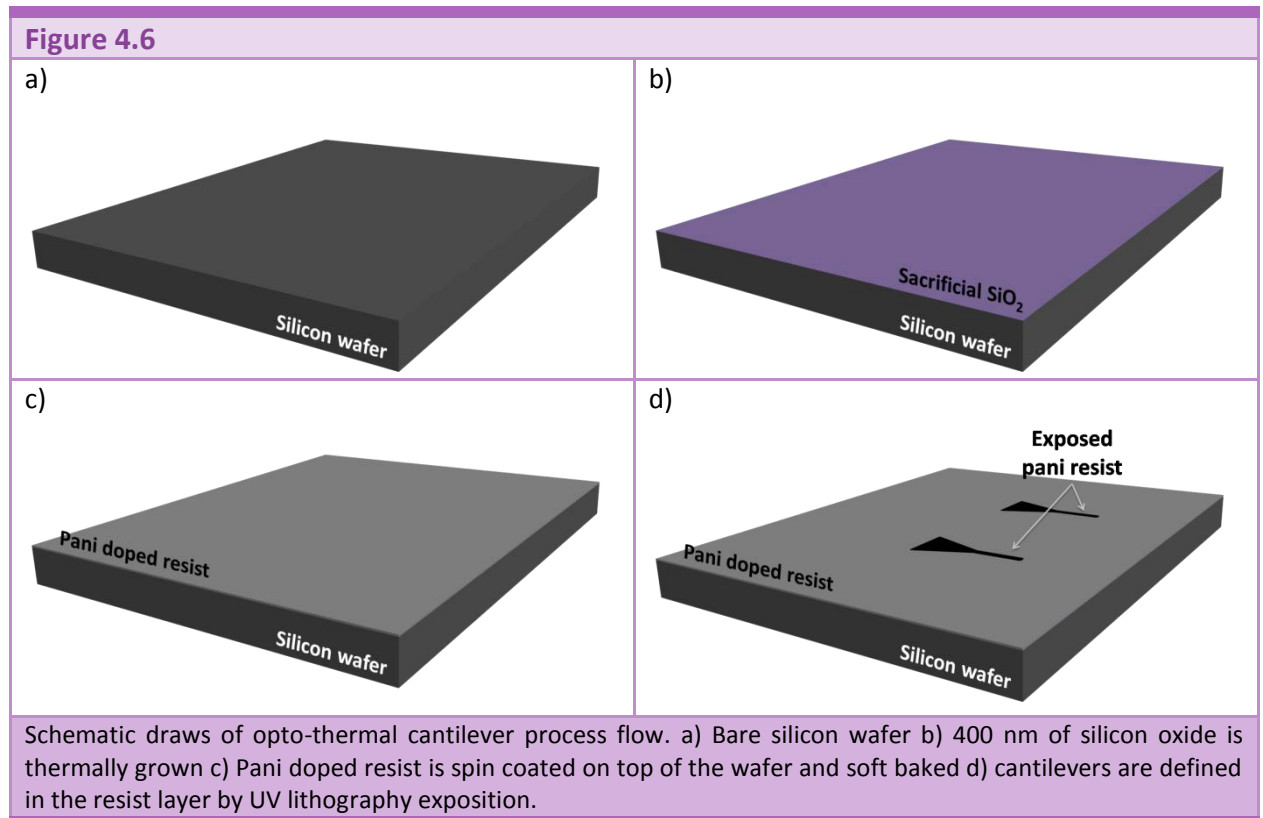
However, some general remarks can be given. For example: the Young's modulus of the structures will not affect notoriously, given the fact that is present with the same power in both the numerator and denominator of $\frac{QM}{EI}$. This, that can result contradictory at a first sight, is easily understandable if the origins of the deflection are considered, i.e. the elongation of the materials. On the other hand, the thickness of the structure must be minimized and the length maximized in order to optimize the deflection.

4.3 FABRICATION

As it has been commented, the design rules are very loose. Therefore, it was decided to build the first generation of devices, and hence obtain a proof of principle, using the set of masks already described in Chapter 2, designed for the fabrication of AFM probes.

4.3.1 Process flow

The fabrication of these optothermal actuators was performed using two layers of polymers: one layer is epoxy based resist and the other layer is the same resist but doped with polyaniline. As have been introduced, two different PANI concentration materials have been used, the first one was referenced by micro resist technology company as mr-L 6002 PANI-20-XP and the second is mr-L 5010 PANI-XP. After the whole fabrication process, in some cases a thin metallic layer was deposited on top of the cantilever in order to improve the reflection (useful when an optical detection technique based on means of laser reflection), which is the reason why a metallic layer has been included in all the calculations that were presented in the previous section.



The fabrication steps for the optothermal cantilevers are very similar to the bilayer cantilevers described in Chapter 3. The main difference between these two processes relies in the fact that optothermal cantilevers do not require a tip, therefore no mould is needed which simplifies and reduces the costs of fabrication.

The beginning of the fabrication process is depicted in Figure 4.6: to define the optothermal devices, the doped resist is deposited on a silicon wafer with a 400 nm SiO₂ layer as a substrate and exposed by UV lithography. As two different polyaniline concentrations have been used to fabricate the devices, two exposition parameters had been optimized, and these values are compiled in Table 4.1. As the doped resist is darker than the non doped one, it is better to deposit it in the first place in order to ease the alignment when the second layer has to be exposed.

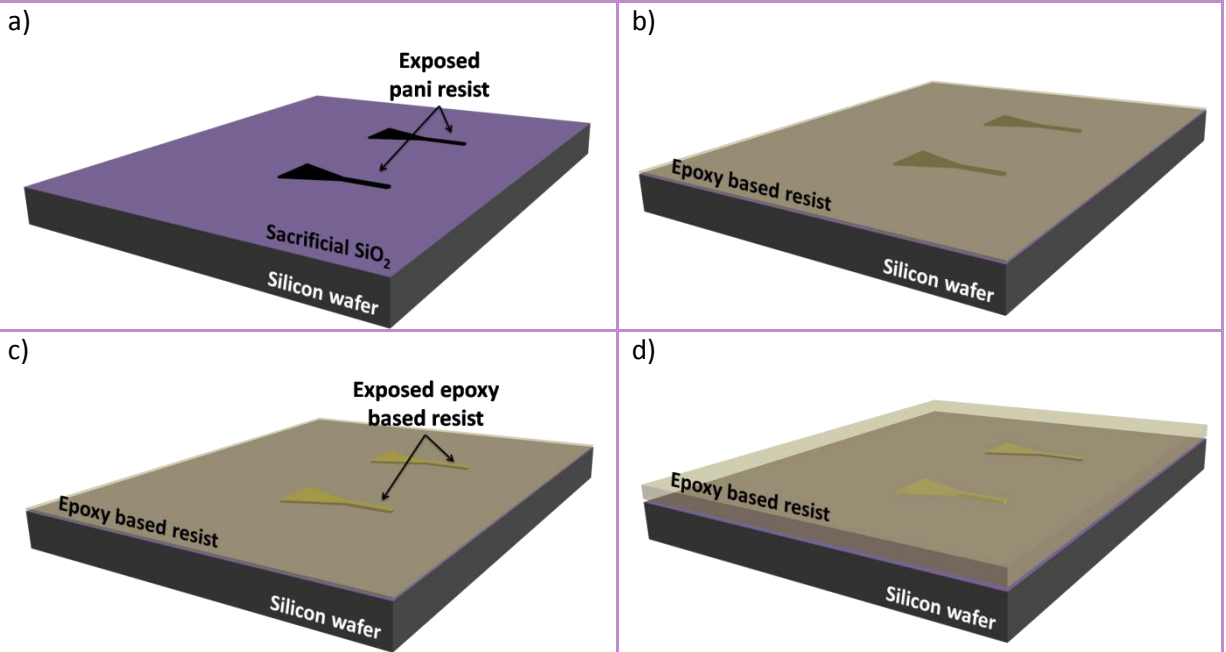
Material	Thickness layer	Spin conditions	Dose
mr-L 6002 PANI-20-XP	2 μm	2000 rpm 400 rpm/s 45 s	2940 mJ/cm ²
mr-L 5010 PANI-XP	7 μm	3000 rpm 400 rpm/s 45 s	455 mJ/cm ²
	4 μm	6000 rpm 400 rpm/s 45 s	365 mJ/cm ²
mr-L 5002 XP	1 μm	2000 rpm 400 rpm/s 45 s	39.2 mJ/cm ²
mr-L 5005 XP	3 μm	3000 rpm 400 rpm/s 45 s	39.2 mJ/cm ²

Table 4.1: Deposition and exposition parameters of the doped and standard epoxy based resist. Resists modified with polyaniline require more exposition time due to the fact their absorbance coefficients at a wavelength of 365 nm are smaller than that of the standard epoxy based resist. Two different standard epoxy based resist have been used in order to deposit layers of similar thickness to that of the doped resist.

After the PEB of the doped resist, the wafer was developed in PGMEA and the surface treated with oxygen plasma during 1 min to adequate the resist to the second layer. The oxygen plasma conditions are the same conditions already described in Chapter 3.

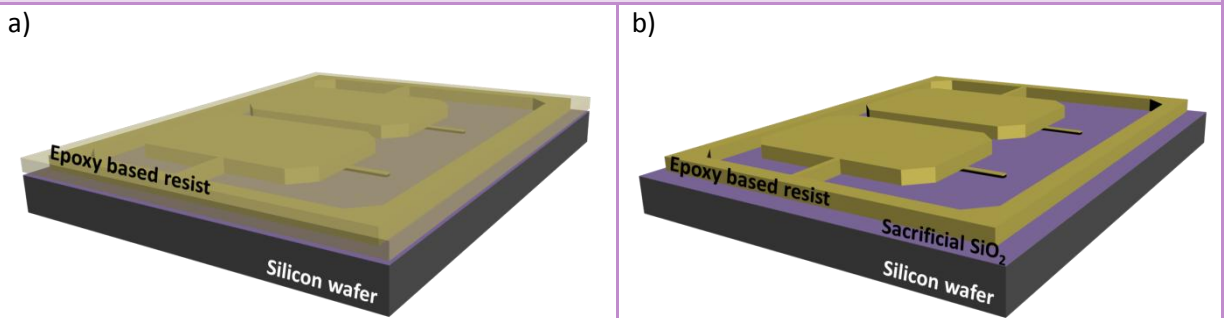
The second deposited layer is the epoxy based resist. The thickness of the epoxy based resist is selected according to the type of PANI resist deposited. As it has been already commented, to obtain optothermal actuation in cantilevers, it is not necessary to have a particular distribution of thicknesses, but the thinner the lever, the higher the final deformation (Figure 4.7).

Figure 4.7



a) PANI doped resist is exposed and developed in PGMEA to ease the alignment of the second layer. b) epoxy based resist is deposited and soft baked after the oxygen plasma treatment. c) The mask of the cantilever is aligned with the patterned cantilevers in the black resist and with the alignment marks. d) after the PEB and without development, the third epoxy based layer is deposited to define the holder of the structure.

Figure 4.8



(a) The 150 μm is soft baked, exposed and PEB. b) Finally the wafer is fully developed in PGMEA and released by etching the sacrificial oxide layer in a buffered HF solution.

A third deposition is performed to define the holder of the cantilever to be easily handled by tweezers. This third deposition consists of a 150 μm thick layer of mr-L 5025. This third layer requires a dose of 910 mJ/cm^2 in order to be fully exposed due to its thickness. When the last layer is exposed and baked, the full wafer is developed. To prevent the levers of presenting an initial deflection, a hard bake process is performed during 2 hours at 120 $^\circ\text{C}$ in an inert atmosphere; the same post-processing step that has been proved to be working properly in

Chapter 2 and 3. Finally, all the chips consisting in cantilevers with holders are released by wet etching of the silicon oxide.

4.3.2 Preliminary characterization of the composite

The elastic properties of the materials were studied by indentation. This study was performed at the *Institut de Ciència de Materials de Barcelona (ICMAB-CSIC)* in the same way as it has been described in Chapter 3. The results are shown in Table 4.2 and were used in order to analyze the experimental results that will be presented afterwards.

Material	Young's modulus	CTE	κ
mr-L 5005	4,6 GPa	$50 \cdot 10^{-6} \text{ K}^{-1}$	0.2 W/(K·m)
mr-L 6002 PANI-20-XP	13 GPa	$\alpha_{\text{PANI-6002}}$	$\kappa_{\text{PANI-6002}}$
mr-L 5010 PANI-XP	6.6 GPa	$\alpha_{\text{PANI-5010}}$	$\kappa_{\text{PANI-5010}}$
Al	70 GPa	$20 \cdot 10^{-6} \text{ K}^{-1}$	235 W/(K·m)

Table 4.2: Material properties of the standard epoxy based resist, the modified resist with polyaniline and of aluminum. For the metal and the standard epoxy based resist, the properties were obtained from materials databases [35]. For doped materials, however, the Young's modulus was determined by nanoindentation. The other two parameters were to be obtained from the experimental results.

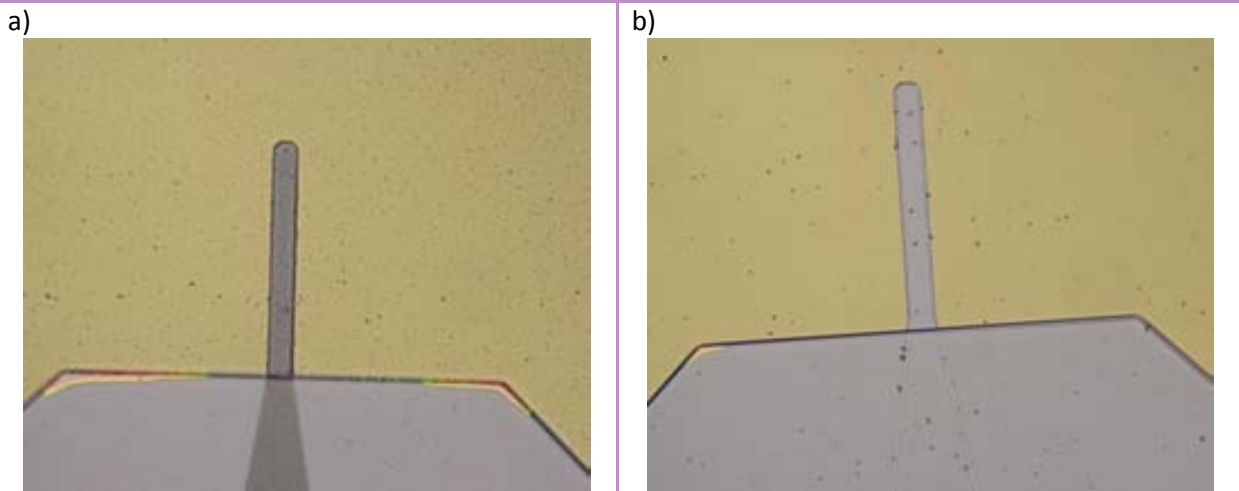
4.3.3 Fabrication results

The main difference between the fabrication of these cantilevers and the previously reported in chapter 2 and 3 is the fact that, in this case, no tip is present on the levers. Therefore, the releasing technique presents a much higher yield. However, the other two mask levels were the same already used for the fabrication of probes, therefore the length of the opto-thermal actuators ranged between 100-1050 μm .

In Figure 4.9, two typical examples of cantilevers just before releasing from the wafer are shown. Figure 4.9.a is showing a cantilever fabricated using the mr-L 6002 PANI-20-X, whereas the structure in Figure 4.9.b was made out of the mr-L 5010 PANI-XP.

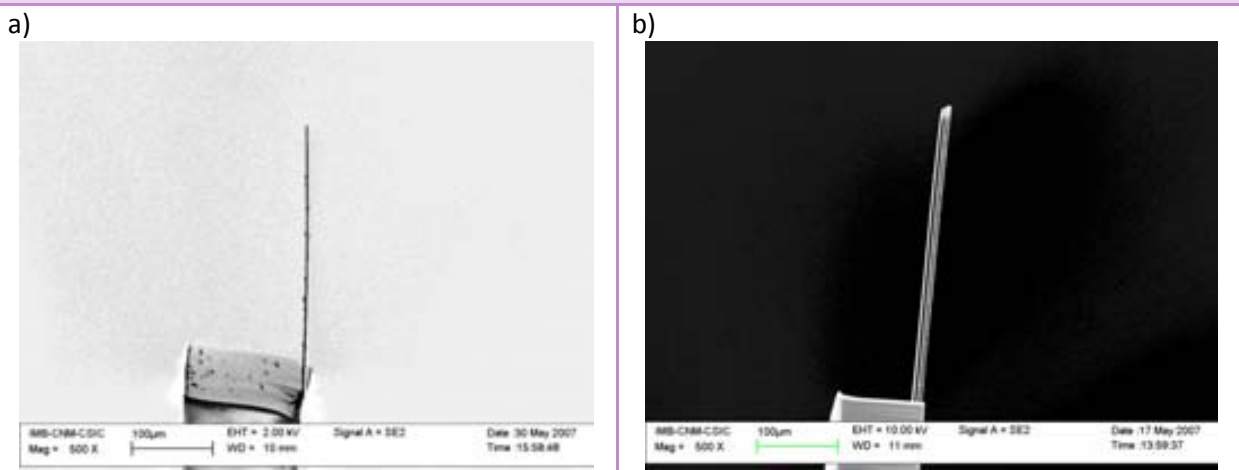
In Figure 4.10, two SEM micrographs show two structures after release. They correspond to the same type of chips that are shown in Figure 4.9. A difference in thickness can be observed, which comes from the fact that the supplied doped resists had different viscosity in the highly and the lowly doped configuration.

Figure 4.9



Optical pictures of (a) an optothermal cantilever fabricated with the highest concentration of PANI-EB in the epoxy based resist (mr-L 6002 PANI-20-X) and (b) with the lowest concentration (mr-L 5010 PANI-XP). The difference in color can be appreciated directly, being the one in (b) almost transparent, as it could be deduced from the absorption spectrum in Figure 4.2. Outside of the levers, on the substrate, dark spots can be seen. Those are PANI (EB) residues that have not been removed with the developer used for the epoxy based resist.

Figure 4.10



SEM micrographs pictures of (a) an optothermal cantilever fabricated with the highest concentration of PANI-EB in the epoxy based resist (mr-L 6002 PANI-20-X) and (b) with the lowest concentration (mr-L 5010 PANI-XP). The difference in thickness is due to the fact that the supplied material had different viscosities.

Finally, in Table 4.3 and Table 4.4 the thicknesses of each of the fabricated cantilevers are shown. Total thickness was tried to get as small as possible and, in addition, it was intended to have both layers of a similar thickness. This was the case in all the fabricated devices except for “*type 2b*” levers, where the processing conditions were not properly adjusted.

Cantilever	mr-L 6002 PANI-20-XP	mr-L 5005	Al
Type 1	1.5 μm	1 μm	-
Type 1-m	1.5 μm	1 μm	20 nm

Table 4.3: Thicknesses of the optothermal cantilevers fabricated out of the highly doped epoxy based resist, mr-L 6002 PANI-20-XP.

Cantilever	mr-L 5010 PANI-XP	mr-L 5005	Al
Type 2a	4 μm	3 μm	-
Type 2a-m	4 μm	3 μm	20 nm
Type 2b	7 μm	0.5 μm	-
Type 2b-m	7 μm	0.5 μm	20 nm

Table 4.4: Different thicknesses of the 4 types of cantilevers fabricated using the low doped epoxy based resist, mr-L 5010 PANI-XP.

4.4 CHARACTERIZATION

In this section, the characterization of the fabricated devices for their use as actuators is presented. This characterization has basically two goals: first, the determination of the material characteristics that appear in the equations of deformation (and in Table 4.2); and, second, the demonstration of the fact that the devices are actually working as opto-thermal actuators, i.e. they are activated by laser illumination.

4.4.1 Constant temperature

As a first experiment, the simplest way of thermal excitation was chosen, that is to say, the cantilevers were placed in a thermal bath at a given temperature. Therefore, as it has been explained before, the complete cantilever had a constant temperature that, at the same time, was equal to the temperature of the thermal bath (air).

In this case, it is expected to find a deflection of the lever given by (4.21) that, in the case of a bi-layered structure, can be written here as:

$$W(x) = -3\Delta T \frac{E_1 E_2 t_1 t_2 (t_1 + t_2)}{t_2^4 E_2^2 + t_1^4 E_1^2 + 2t_1 t_2 (2t_1^2 + 3t_1 t_2 + 2t_2^2) E_1 E_2} (\alpha_2 - \alpha_1) x^2 \quad (4.55)$$

or, in the case of having a thin metal layer on top:

$$W(x) = -3\Delta T \frac{E_1 E_2 (\alpha_2 - \alpha_1) t_1 t_2 (t_1 + t_2) + E_m E_2 (\alpha_m - \alpha_2) t_m t_2^2 + E_1 E_m (\alpha_m - \alpha_1) t_1 t_m (t_1 + 2t_2)}{t_2^4 E_2^2 + t_1^4 E_1^2 + 2t_1 t_2 (2t_1^2 + 3t_1 t_2 + 2t_2^2) E_1 E_2 + 2t_m t_1 (2t_1^2 + 6t_1 t_2 + 6t_2^2) E_1 E_m + 4t_m t_2^3 E_2 E_m} x^2 \quad (4.56)$$

Therefore, provided the deflection is measured, we can obtain a value for the CTE of the doped resist, which is the only unknown parameter in both equations.

The measurements for this experiment were performed at the *Instituto de Microelectrónica de Madrid* (IMM) under collaboration with Dr. M. Calleja and Dr. J. Tamayo. The setup is based in laser reflection by the cantilever which is then collected by a 4-quadrant photodiode to detect instantaneously the deflection, in a similar way to the detection technique used in most of the commercial AFMs. The differential characteristic of the setup is the fact that the laser can be moved in order to scan all the cantilever, meaning that the complete profile, $W(x)$, can be

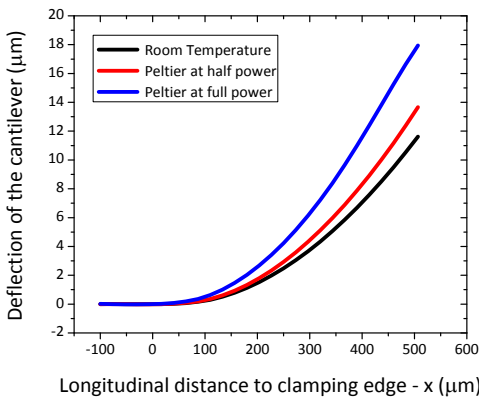
obtained and not just the deflection of the free edge. As it is explained in [36], the actual signal that is acquired is the derivative of the deflection, $W'(x)$, which has to be integrated in order to have the real profile of the cantilever.

The heating element is a thermoelectric cooler/heater (a Peltier plate) which is placed below the lever. The maximum temperature that can be achieved is 50 °C in the plate itself. The transfer of temperature from there into the lever is done via conduction through the holder and convection through the air. In principle, the temperature of the cantilever will be considered as the same of the heater. The main problem is that the measurements were performed in a non-controlled environment, where variations of the room temperature (RT) can be up to 5 °C. If RT is 22.5 ± 2.5 °C, then the maximum increment in temperature will be 27.5 ± 2.5 °C, which means almost a 10% of uncertainty. If the increment in temperature is smaller, the uncertainty is much larger.

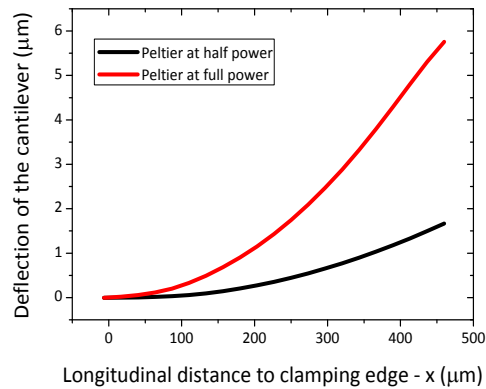
Several optothermal cantilevers were measured using this technique, of all types shown in Table 4.4. The deflection profile of the levers at full, half and zero power of the heating element was acquired, as can be seen in the example in Figure 4.11.a. Subsequently, the deflection at zero power was subtracted from the others (Figure 4.11.b), obtaining the actual differential deflection that will behave as (4.55) and (4.56) are predicting. It can be noted here that this subtraction can be done because the system does not present non-linearities, hence the principle of superposition can be applied.

Figure 4.11

a)



b)



(a) Deflection measurements for an optothermal device type 2a-m (fabricated using mr-L 5010 PANI-XP, lowly doped resist) taken at room temperature, when the peltier was working at half power (around 35°C) and when the peltier was working at full power (around 50°C). (b) Differential deflection due to the heating.

Once the differential deflections have been obtained, they were fitted to a polynomial function of second degree and values for the CTE were obtained, considering as (4.56) and its particular case (4.55). This way, it is possible to obtain a value for the coefficient of thermal expansion of the doped resist that will be given by (4.57). As deflection data acquired from cantilevers made out of both types of doped resist were acquired, and fitted to the same value, (4.57) is the linear coefficient of thermal expansion for both doped epoxy based resists.

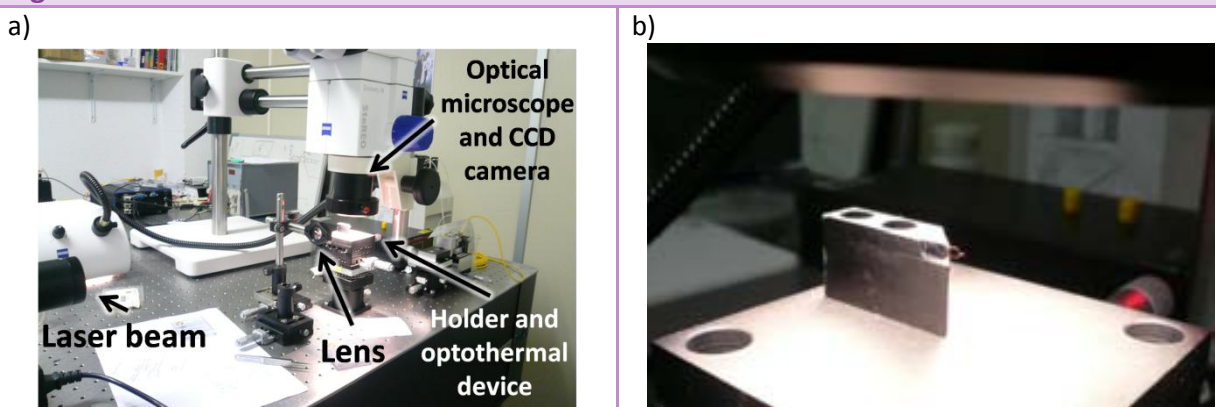
$$\alpha_{PANI} = \alpha_{PANI-6002} = \alpha_{PANI-5010} = (75 \pm 5) \cdot 10^{-6} K^{-1} \quad (4.57)$$

4.4.2 Optothermal actuation – Experimental setup 1

Once the coefficient of thermal expansion was calculated, a real optothermal actuation experiment was carried out in order to prove the actual behaviour/responsiveness of the fabricated devices to light stimulus.

The experimental setup consisted in a He-Ne laser (640 nm, P = 10 mW) that was locally illuminating a cantilever placed in a galvanized solid holder (see Figure 4.12). The lever was placed perpendicular to the laser, and the laser was focused by means of a convergent lens in the cantilever plane. A digital CCD camera coupled to a microscope was placed over the lever in order to measure the deflection.

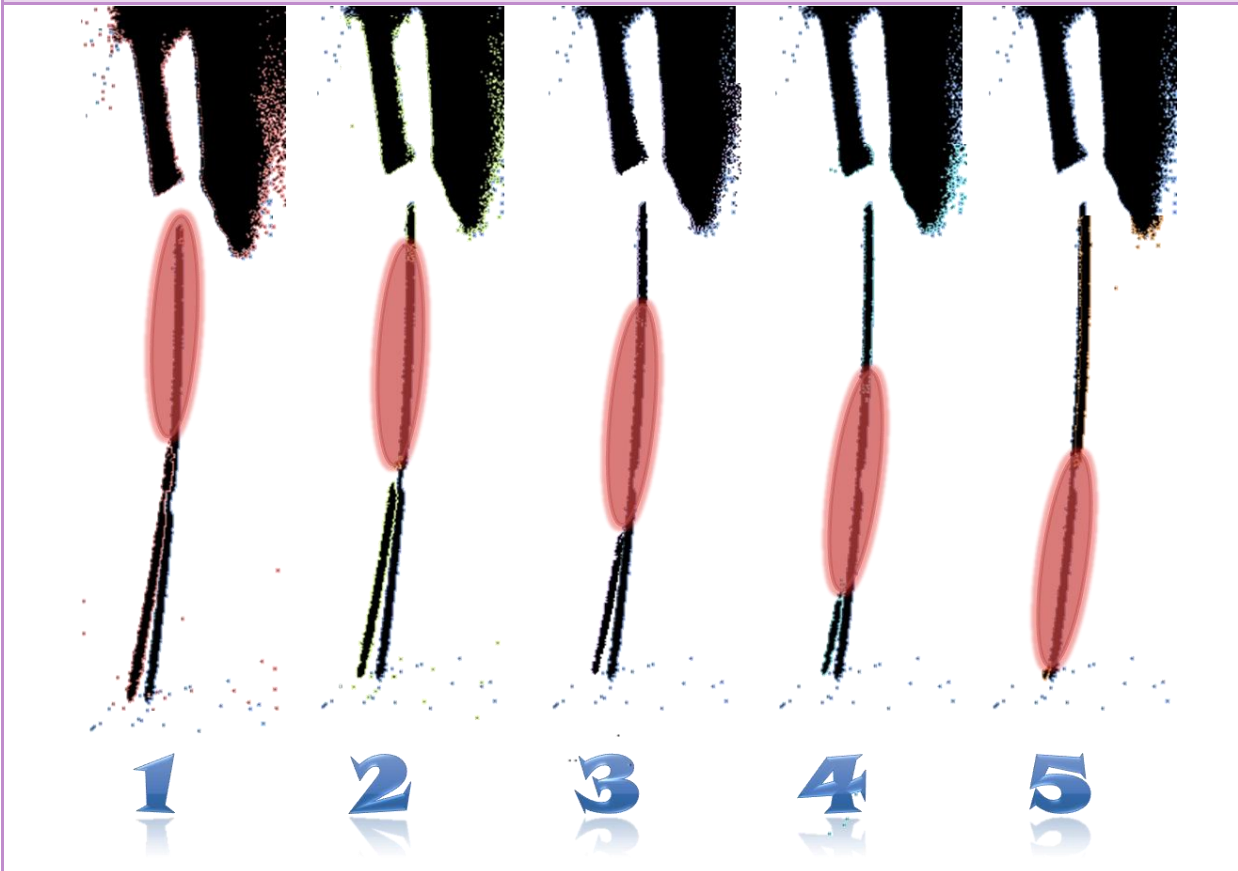
Figure 4.12



Experimental setup – 1. Pictures showing (a) the laser, the holder and the camera used in the measurements and (b) a zoom in on the holder.

The acquired data were pictures of the whole cantilever, as it can be seen in Figure 4.13. Subsequently, the pictures were processed and the deflection of the free end was acquired.

Figure 4.13

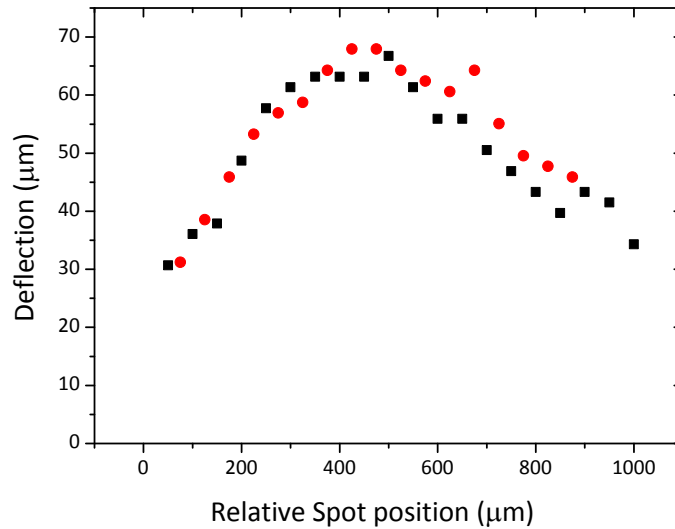


Overlapping of pictures showing the progressive deflection of the cantilever as a function of the displacement of the actuating laser. All the pictures were taken from cantilevers fabricated using mr-L 6002 PANI-20-X resist.

Using this experimental setup, the deflection of the lever was studied as a function of the position of the laser (Figure 4.13). Using some micrometric screws, the lever could be moved perpendicular to the laser and the camera, just changing in the longitudinal direction the place where the light was applied.

In Figure 4.14, measurements for two different cantilevers of the deflection at the free end as a function of the longitudinal position of the laser spot is shown. It has to be noted that the X axis is just a relative position of the beam. Given the fact that the spot of the laser has a finite size (λ in the model), it is not possible to exactly determine the centre of the spot. The only thing that is known is the displacement (performed by a micrometric screw) in the perpendicular direction, meaning that the distance between two different measurements is known, but not the exact position of the beam. Therefore, X axis is just a relative position of the spot.

Figure 4.14



Deflection of the free end of two different type 1 cantilevers (fabricated using mr-L 6002 PANI-20-X) of $L = 1000 \mu\text{m}$ as a function of the relative position of the laser spot.

In order to analyze the data from Figure 4.14, it was firstly considered to approximate the whole system using a model with a rectangular distribution of the temperature, i.e. considering that the zone where the laser was hitting the lever was a different temperature (higher) than the rest of the lever. That approximation proved to be not accurate enough, implying the need for a finer modelling. Hence, the already described model with a rectangular distribution of the incident power was taken.

The formulae considered were (4.42), (4.48) and (4.54), building the expression for the deflection of the free edge of the lever, $W(x = L)$, taking the position of the laser x_0 as the variable:

$$W(x) = -\frac{QM}{EI\beta} \cdot \begin{cases} \Delta T_0 \left(\frac{\beta}{2} L^2 + 1 \right) + a'_1 e^{\sqrt{\beta}L} + b'_1 e^{-\sqrt{\beta}L} & 0 < x_0 - \delta < \frac{\lambda}{2} \\ \Delta T_0 \left(\frac{\beta}{2} \left(L - x_0 + \frac{\lambda}{2} \right)^2 + 1 \right) + a_2 e^{\sqrt{\beta}L} + b_2 e^{-\sqrt{\beta}L} & \frac{\lambda}{2} < x_0 - \delta < L - \frac{\lambda}{2} \\ \Delta T_0 \left(\frac{\beta}{2} \left(L - x_0 + \frac{\lambda}{2} \right)^2 + 1 \right) + a''_2 e^{\sqrt{\beta}L} + b''_2 e^{-\sqrt{\beta}L} & L - \frac{\lambda}{2} < x_0 - \delta < L \end{cases} \quad (4.58)$$

where the constants $a'_1, b'_1, a_2, b_2, a''_2, b''_2$ have already been calculated. Hence, the objective was to fit the acquired data with (4.58), but using the geometries of the lever (type 1 and $L =$

1000 μm) and the known material properties. The free parameters to fit were: the length of the laser spot (λ), the thermal conductivity of the doped resist (β_1), the absorbed power (P_{Abs}), the parameter of losses (h) and the exact position where the clamping edge is actually located (δ) (X axis in Figure 4.14 is relative, as it has been commented).

In the first place, the parameter of losses was determined by comparing the model for the stationary distribution of temperatures with Finite Element Modelling (FEM) simulations of the system. Given the fact that the parameter was included in the model just to emulate the energy losses, it was considered that the obtained value would describe well the behaviour of the system.

$$h = \text{parameter of losses} = 110 \frac{\text{W}}{\text{m}^2 \cdot \text{K}} \quad (4.59)$$

The rest of the parameters were left to be freely chosen by the fitting algorithm but always taking into account the physical meaning of each parameter. The best fitting values were found to be, approximately (Figure 4.15.a):

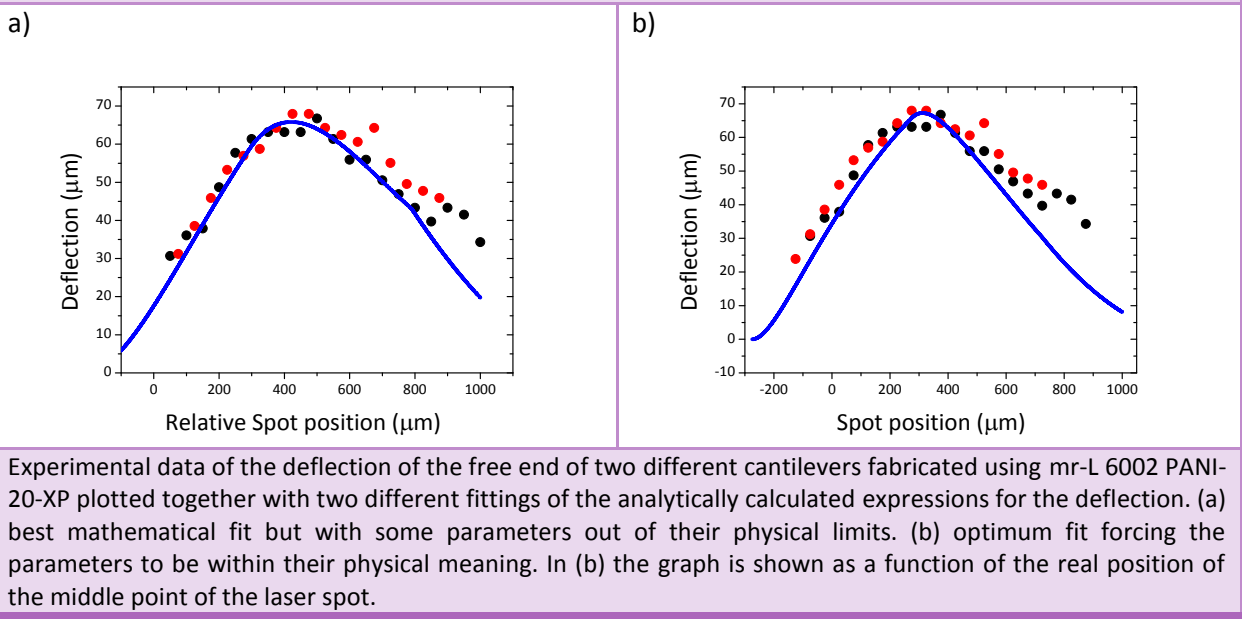
$$\kappa_{PANI-6002} = 3 \frac{\text{W}}{\text{m} \cdot \text{K}}; P_{abs} = 0.15 \text{ mW}; \lambda = 500 \mu\text{m}; \delta = -40 \mu\text{m} \quad (4.60)$$

But, although the fitting was optimum, it was not possible that the thermal conductivity of a polymer doped with polyaniline was as high as $3 \frac{\text{W}}{\text{m} \cdot \text{K}}$. Forcing the conductivity to be $< 1 \frac{\text{W}}{\text{m} \cdot \text{K}}$, in accordance with the literature [16, 17], the optimum fitting was found for the values (Figure 4.15.b):

$$\kappa_{PANI-6002} = 0.3 \frac{\text{W}}{\text{m} \cdot \text{K}}; P_{abs} = 0.105 \text{ mW}; \lambda = 550 \mu\text{m}; \delta = -125 \mu\text{m} \quad (4.61)$$

Using this experiment, the thermal conductivity for the highly doped resist (mr-L 6002 PANI-20-XP) was found ($\kappa_{PANI-6002}$). When it was applied to measure the deflection of the cantilevers fabricated using mr-L 5010 PANI-XP, some movement was also detected, but it was so small that it was not possible to quantify it using the CCD camera. Therefore, a different method was used in order to characterize the lowly doped resist.

Figure 4.15



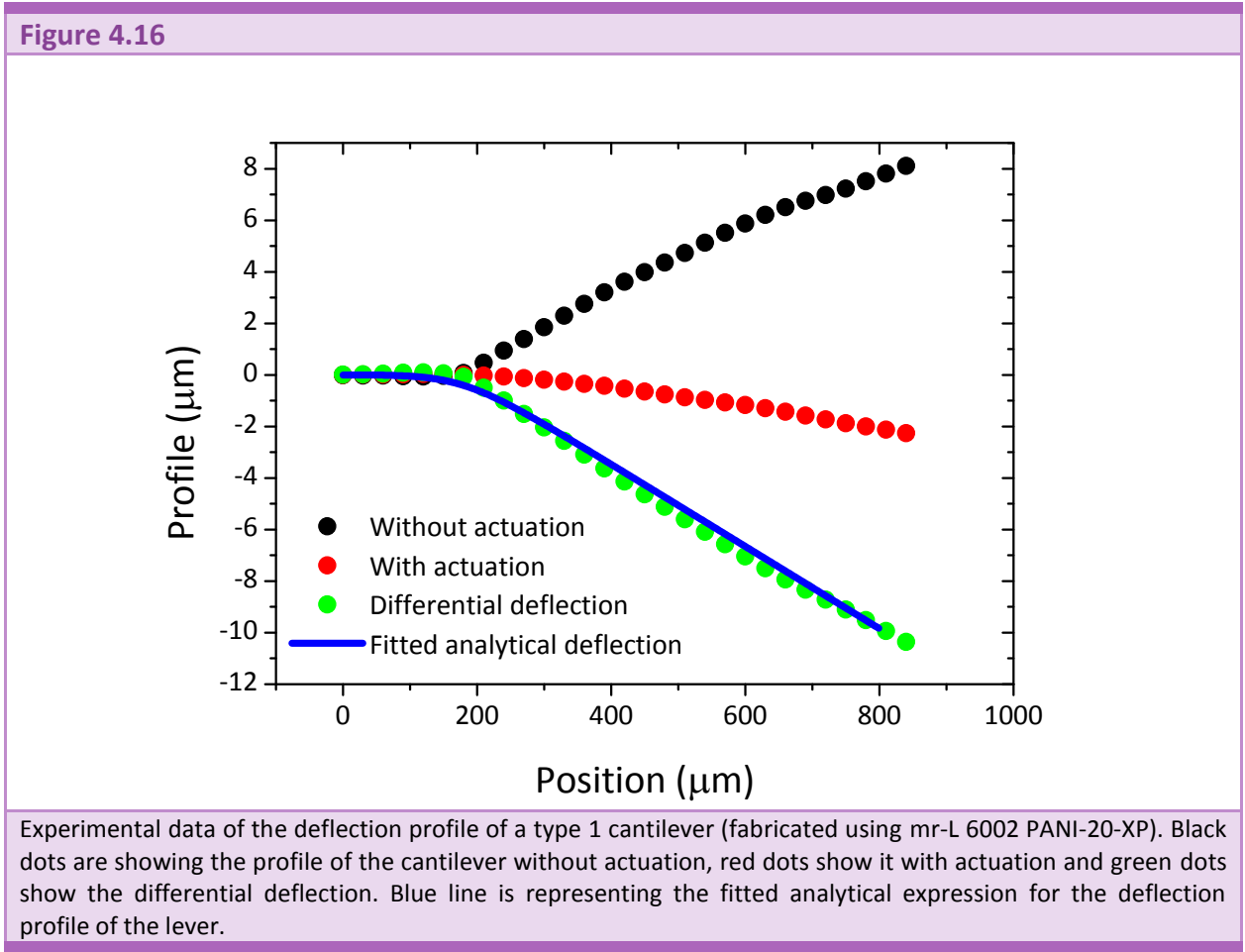
4.4.3 Optothermal actuation – Experimental setup 2

The second experiment to characterize the optothermal actuation of the polymeric cantilevers was carried out using a similar setup than that described for the thermal actuation [36], i.e. using a laser to acquire the deflection of the lever all along its longitudinal axis. The main difference consisted in the use of a second laser in order to heat the cantilever [34], in a similar way described in the previous section. These experiments were performed in the *Instituto de Microelectrónica de Madrid* (IMM) under collaboration with Dr. M. Calleja and Dr. J. Tamayo.

In this case, the formulae that have to be taken into account are (4.42), (4.48) and (4.54). Depending on the position of the laser actuator, the appropriate expression should be chosen. Of course, such a choice must be done once the data have been analyzed because a priori it is difficult to distinguish in which of the three cases the system is.

The experimental procedure was as following: a first measurement of the profile of the lever was measured without the actuating laser, just with the measuring laser; subsequently, a second measurement of the profile was acquired, this time with the actuating laser “on”, hitting the lever at an unknown position. As it has been commented before, the differential equations governing the system do not contain any non-linearity, so the superposition principle can be applied; therefore the differential deflection between the two described measurements is due to the differential input, i.e. the actuating laser, and hence (4.42), (4.48) and (4.54) can be

applied. A typical example of this kind of measurements can be seen in Figure 4.16, which shows the profile of the cantilever without actuation (black dots), with actuation (red dots) and the differential deflection (green dots), together with the fitted analytical expression for the deflection.

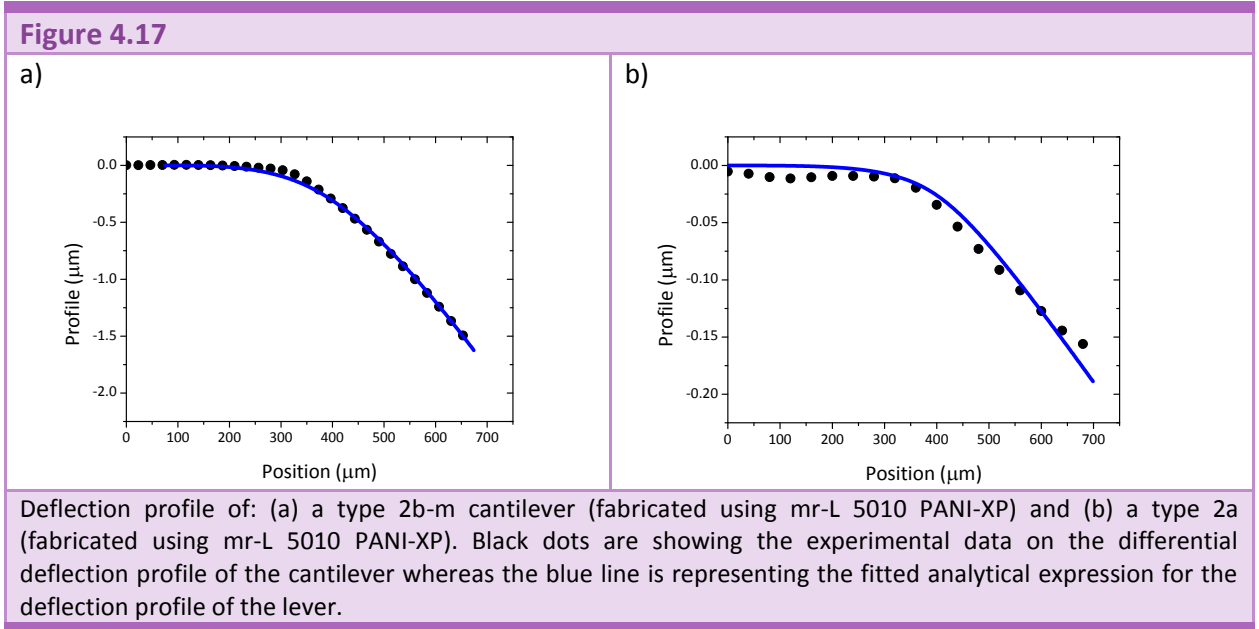


All the acquired data fit properly to the analytical expressions. In Figure 4.17, two different measurements are presented: (a) comes from a type3-m cantilever and (b) from a type2. As both types of cantilevers are fabricated using the lowly doped epoxy based resist (mr-L 5010 PANI-XP), it is found that the thermal conductivity for this new resist is:

$$\kappa_{PANI-5010} = 0.3 \frac{W}{m \cdot K} \tag{4.62}$$

Therefore:

$$\kappa_{PANI} = \kappa_{PANI-6002} = \kappa_{PANI-5010} = 0.3 \frac{W}{m \cdot K} \quad (4.63)$$



4.4.4 Discussion of results

Once all the material properties have been estimated, the first conclusion that can be extracted is the fact that, even though both doped resists are different in some properties as the Young's modulus or the absorption spectrum, for the thermal conductivity and the thermal expansion coefficient, both of them have the same (very similar) values, meaning that the thermal properties are not influenced by the amount of doping, at least by the amount of doping that has been used to prepare these two resists.

The second result that can be extracted is that it is possible to calculate the expression $\frac{QM}{EI}$ for all the six types of cantilevers that have been fabricated and that can be found in Table 4.3 and Table 4.4. This expression, as it can be recalled from (4.19), relates the curvature of the lever with the distribution of temperature, meaning that the larger it is, the larger the effect of the temperature.

The values for these parameters are included in Table 4.5 and it can be seen that the cantilevers with a metal layer present an increased optothermal actuation. This is because the metal layer

was deposited on the side of the non-doped resist. Had it been deposited on the other side, the results would have been opposite.

Type 1	Type 1-m	Type 2	Type 2-m	Type 3	Type 3-m
11.8	16.3	5.07	5.78	0.947	1.984

Table 4.5: Values for $\frac{QM}{EI}$ for all the six types of fabricated levers. The units are $(m^{-1}K^{-1})$ in all the cases. The magnitude of these expressions is directly related with the deflection that is obtained when a given temperature is applied to the lever.

Finally, it must be commented the most important effect that the difference in the type of resist brings to the behavior of the optothermal actuation. If two different levers, non-metallized, are compared, for example the fitting of Figure 4.17.b and Figure 4.16, each of them fabricated with one type of resist, it is possible to see that the absorbed power presents a difference of one order of magnitude. This difference is due to the fact that the lowly doped resist has an absorption spectrum almost flat around the wavelength of the used laser. On the other hand, the highly doped resist, presents a maximum around that wavelength, which implies much higher power absorption.

4.5 CONCLUSIONS

In this chapter, the fabrication of a polymeric optothermal actuator has been presented. It has been shown how the absorbance spectrum of a given epoxy based resist can be modified by mixing it with an additional polymer, in this case polyaniline emeraldine base (PANI-EB), in order to make the new polymeric composite more sensitive to laser light in the visible or infrared.

Two different resists, with two different concentrations of PANI-EB, were used in order to fabricate bilayered cantilevers, composed by a layer of standard resist and a second layer of the doped one.

Cantilevers with thicknesses between 2.5 μm and 7.5 μm were fabricated and some of them coated with aluminum for an improved reflection.

Theoretical calculations were performed in order to understand the actuation mechanism when a thermal load is uniformly applied to the structure, when is applied only in a partial region and when a constant power is applied locally.

Experimental measurements were performed in order to test if the concept of actuation was working and in order to characterize some material properties. Two kind of measurements were performed; one with the polymeric structure at a constant temperature and measuring the deflection (only thermal actuation), and the other applying locally a constant incident power by means of a laser focused in the actuator, and measuring the deflection (optothermal actuation).

The experimental results showed that the actuation principle is working for both resists, but in a much larger extent for the highly doped version. In addition, using the theoretical calculations to analyze the experimental results it was possible to determine the coefficient of thermal expansion and the thermal conductivity of the doped resists. This measurements show that devices fabricated with the described technology will be valid as actuators, with a very low fabrication cost and a high displacement.

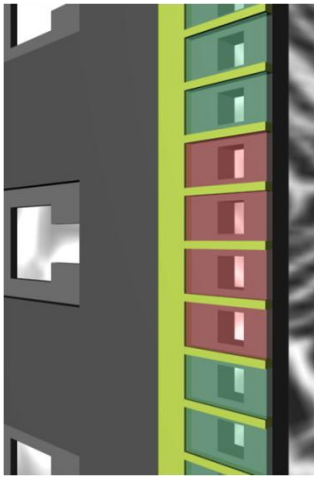
4.6 REFERENCES

1. K.E. Petersen
"Silicon as a Mechanical Material".
Proceedings of the IEEE, 1982, **70**(5), 420-457.
2. M. Gad-el-Hak
"MEMS applications : the MEMS handbook".
Ed. *CRC Press/Taylor & Francis*, 2006, ISBN: 0849391393.
3. J. Fraden and F. Knovel
"Handbook of modern sensors physics, designs, and applications".
Ed. *Springer*, 2004, ISBN: 9781601193476, 1601193475.
4. G.K. Lau, J.F.L. Goosen, F. van Keulen, T.C. Duc, and P.M. Sarro
"Powerful polymeric thermal microactuator with embedded silicon microstructure".
Applied Physics Letters, 2007, **90**(21), 214103.
5. C. Vancura, J. Lichtenberg, A. Hierlemann, and F. Josse
"Characterization of magnetically actuated resonant cantilevers in viscous fluids".
Applied Physics Letters, 2005, **87**(16), 162510.
6. Asylum
"Asylum research web page".
<http://www.asylumresearch.com>, 2007.
7. K.L. Ekinici and M.L. Roukes
"Nanoelectromechanical systems".
Review of Scientific Instruments, 2005, **76**(6), 061101.
8. I. Bargatin, I. Kozinsky, and M.L. Roukes
"Efficient electrothermal actuation of multiple modes of high-frequency nanoelectromechanical resonators".
Applied Physics Letters, 2007, **90**(9), 093116.
9. A. Llobera, G. Villanueva, V.J. Cadarso, S. Buttgenbach, and J.A. Plaza
"Polymeric MOEMS variable optical attenuator".
Ieee Photonics Technology Letters, 2006, **18**(21-24), 2425-2427.
10. J.M. Zanardi Ocampo, P.O. Vaccaro, K. Kubota, T. Fleischmann, T.-S. Wang, T. Aida, T. Ohnishi, A. Sugimura, R. Izumoto, M. Hosoda, and S. Nashima
"Characterization of GaAs-based micro-origami mirrors by optical actuation".
Microelectronic Engineering, 2004, **73-74**, 429-434.
11. B.E. Jones and J.S. McKenzie
"A review of optical actuators and the impact of micromachining".
Sensors and Actuators A: Physical, 1993, **37-38**, 202-207.
12. S.V. Ahir and E.M. Terentjev
"Photomechanical actuation in polymer-nanotube composites".
Nature Materials, 2005, **4**(6), 491-495.

13. G.G. Stoney
"The tension of metallic films deposited by electrolysis".
Proceedings of the Royal Society of London Series A-Containing Papers of a Mathematical and Physical Character, 1909, **82**(553), 172-175.
14. S. Timoshenko
"Analysis of bi-metal thermostats".
Journal of the Optical Society of America and Review of Scientific Instruments, 1925, **11**(3), 233-255.
15. M.F. Ashby
"On the Engineering Properties of Materials".
Acta Metallurgica, 1989, **37**(5), 1273-1293.
16. J.C. Chiang and A.G. Macdiarmid
"Polyaniline - Protonic Acid Doping of the Emeraldine Form to the Metallic Regime".
Synthetic Metals, 1986, **13**(1-3), 193-205.
17. Y. Cao, P. Smith, and A.J. Heeger
"Counterion Induced Processibility of Conducting Polyaniline and of Conducting Polyblends of Polyaniline in Bulk Polymers".
Synthetic Metals, 1992, **48**(1), 91-97.
18. Microresist
"Micro Resist Technology GmbH Webpage".
<http://www.microresist.de>, 2007.
19. N.V. Lavrik, M.J. Sepaniak, and P.G. Datskos
"Cantilever transducers as a platform for chemical and biological sensors".
Review of Scientific Instruments, 2004, **75**(7), 2229-2253.
20. H.P. Lang, M.K. Baller, R. Berger, C. Gerber, J.K. Gimzewski, F.M. Battiston, P. Fornaro, J.P. Ramseyer, E. Meyer, and H.J. Guntherodt
"An artificial nose based on a micromechanical cantilever array".
Analytica Chimica Acta, 1999, **393**(1-3), 59-65.
21. J. Fritz, M.K. Baller, H.P. Lang, H. Rothuizen, P. Vettiger, E. Meyer, H.J. Guntherodt, C. Gerber, and J.K. Gimzewski
"Translating biomolecular recognition into nanomechanics".
Science, 2000, **288**(5464), 316-318.
22. Y. Arntz, J.D. Seelig, H.P. Lang, J. Zhang, P. Hunziker, J.P. Ramseyer, E. Meyer, M. Hegner, and C. Gerber
"Label-free protein assay based on a nanomechanical cantilever array".
Nanotechnology, 2003, **14**(1), 86-90.
23. J. Zhang, H.P. Lang, F. Huber, A. Bietsch, W. Grange, U. Certa, R. McKendry, H.J. Guntgerodt, M. Hegner, and C. Gerber
"Rapid and label-free nanomechanical detection of biomarker transcripts in human RNA".
Nature Nanotechnology, 2006, **1**(3), 214-220.
24. A. Boisen, J. Thaysen, H. Jensenius, and O. Hansen
"Environmental sensors based on micromachined cantilevers with integrated read-out".
Ultramicroscopy, 2000, **82**(1-4), 11-16.

25. P.A. Rasmussen, J. Thaysen, O. Hansen, S.C. Eriksen, and A. Boisen
"Optimised cantilever biosensor with piezoresistive read-out".
Ultramicroscopy, 2003, **97**(1-4), 371-376.
26. M. Li, H.X. Tang, and M.L. Roukes
"Ultra-sensitive NEMS-based cantilevers for sensing, scanned probe and very high-frequency applications".
Nature Nanotechnology, 2007, **2**(2), 114-120.
27. A. Gupta, D. Akin, and R. Bashir
"Single virus particle mass detection using microresonators with nanoscale thickness".
Applied Physics Letters, 2004, **84**(11), 1976-1978.
28. J.S. Pulskamp, A. Wickenden, R. Polcawich, B. Piekarski, M. Dubey, and G. Smith
"Mitigation of residual film stress deformation in multilayer microelectromechanical systems cantilever devices".
Journal of Vacuum Science & Technology B, 2003, **21**(6), 2482-2486.
29. S. Timoshenko and J.N. Goodier
"Theory of elasticity".
 Ed. *McGraw-Hill*, 1970, ISBN: ENG QA931.T5853 1970.
30. K. Washizu
"Variational methods in elasticity and plasticity".
 Ed. *Pergamon Press*, 1975, ISBN: 0080176534.
31. S.D. Senturia
"Microsystem design".
 Ed. *Kluwer Academic Publishers*, 2001, ISBN: 0792372468.
32. J.L. Corbeil, N.V. Lavrik, S. Rajic, and P.G. Datskos
"Self-leveling" uncooled microcantilever thermal detector".
Applied Physics Letters, 2002, **81**(7), 1306-1308.
33. N.V. Lavrik and P.G. Datskos
"Femtogram mass detection using photothermally actuated nanomechanical resonators".
Applied Physics Letters, 2003, **82**(16), 2697-2699.
34. D. Ramos, J. Tamayo, J. Mertens, and M. Calleja
"Photothermal excitation of microcantilevers in liquids".
Journal of Applied Physics, 2006, **99**(12), 124904.
35. M. Winter
"WebElements™ periodic table".
<http://www.webelements.org>, 2007.
36. M. Alvarez and J. Tamayo
"Optical sequential readout of microcantilever arrays for biological detection".
Sensors and Actuators B-Chemical, 2005, **106**(2), 687-690.

Chapter 5. POLYMERIC HYDROPHOBIC BARRIERS



In Chapter 5 two novel methods for the preparation of arbitrary micro-scale patterns of polymers on surfaces with pre-defined topography are depicted. While photosensitive polymers are commonly used together with optical lithography, the methods presented in this section can be used for non-photostructurable polymers and where spin-coating cannot be performed. As a demonstrator of the viability of the fabrication processes, they have been applied for the definition of hydrophobic barriers in a microfluidics network, which is dedicated to selectively dispense liquid to a spotting device consisting of 12 silicon microneedles. The barriers are needed in the microfluidics network to assure no intermixing of liquids, which would cause cross-contamination in the dispensing system.

5.1 INTRODUCTION

Microfluidics allows manipulating and transporting liquid at the micrometer scale by the suitable patterning of surfaces and by combining hydrophilic and hydrophobic areas [1, 2]. It was initiated at the beginning of the decade of the 1990's as a fundamental point for the generation of Lab-on-a-Chip or micro Total Analysis Systems (μ -TAS) systems [3-5]. This kind of systems implies the achievement of higher sensitivity and resolution using very small amounts of sample, which is one of the main reasons for the development of microfluidics technology [2].

Microfluidics systems can be established either on silicon or on polymer-based technology. The first one, silicon-based technology, is more robust, reliable and, given that it is based on the microelectronics fabrication, it is highly developed [6, 7]. Both Silicon and glass are used as materials to build the systems, being the latter one more used because of its insulating properties. On the other hand, polymer-based technology is faster, cheaper, more flexible and simple [8, 9]. The two preferred materials are SU-8 and poly (dimethylsiloxane) or PDMS (an optically transparent, soft elastomer). Both, silicon and polymer based technologies, have been and are used for different applications. Originally, all the fabrication techniques and knowledge from the microelectronics field were applied to build silicon and glass systems. Later, plastics became more and more important until the current state of the art, in which PDMS is widely used. In fact, it is the key material for exploratory research and research engineering at the early stages of development mainly due to the ease with which new concepts can be tested.

In this chapter, the fabrication of a microfluidics network by the combination of both kinds of technologies is presented. Using previous know-how, the main structure in the chip was aimed by standard silicon fabrication technology. After that, two different methods for polymer structures definition were used. These methods, soft-lithography and ink-jet lithography, allow the fabrication of structures on top of substrates with pre-defined topography.

As it was introduced in Chapter 1, soft lithography is a low-cost strategy for carrying out micro- and nano-fabrication. It is possible to find several techniques that are known as soft-lithographic, i.e. microcontact printing (μ CP), replica molding (REM), micromolding in capillaries (MIMIC), microtransfer molding (μ TM) [10, 11]. The common characteristic to all of the previously mentioned techniques is the use of an elastomeric block with patterned relief structures on its surface. PDMS or silicone rubbers have been the most used materials. The fabrication of such stamp is done by pouring a prepolymer of the elastomer over a master having relief structure on its surface. The prepolymer is then cured and subsequently peeled off.

Once the mould has been made, it can be used, for example, to create patterned self assembled monolayers SAMs on a substrate (μ CP). These SAMs [12] can be then be used as a mask to pattern transfer the substrate [13, 14], to provide a selective binding to some proteins or other biological species [15] or to generate gradients of hydrophobicity [16].

On the other hand, the stamp can be used to replicate its relief structures in a polymeric material by pouring the polymer onto it to generate a replica (REM, technique similar to the initial preparation of the mould); or transfer the reliefs onto a substrate after removing the excess of polymer (μ TM); or replicating the reliefs on a substrate by means of capillary action (MIMIC). All these techniques are then based on the use of the stamp as a mould, transferring the shape into a polymer or prepolymer that becomes solid and stiff after curing, exposing to UV-light, etc.

Soft-lithography techniques are low cost and allow the fabrication of micro- and sub-micrometer patterns without using photolithography (or other even more expensive) equipments. That's the point where its main advantage yields, the fact that every laboratory can have access to micro- and nano- fabrication without needing big investment, but for the initial master fabrication.

The second method for the definition of the polymer structures, also introduced in Chapter 1, is ink-jet printing lithography. Ink-jet printing is a technique that allows drop-on-demand dispensing of microscale droplets by means of an actuated nozzle [17, 18].

During the last decades the development and evolution of ink-jet printing systems has been enormous, motivated mainly by the market of printers for computers. The present state-of-the-art of ink-jet printers for domestic users includes printers that can deposit droplets of ink on top of a sheet of paper with a size below 100 μ m in radius [19]. In research, ink-jet systems have been used to selectively functionalize cantilevers [20, 21], to fabricate transistors [22, 23], to locally deposit nanoparticles [24], to fabricate structures with materials that are difficult to machine by other methods [25], etc.

A standard ink-jet system [26] consists of a glass capillary with a narrow end (nozzle) in the tens of microns range in diameter, integrated with an actuator. These two parts together form any commercial printing head. In addition, it is necessary to have a moving xy-system to allow locally selective deposition of material onto the substrate. This can be attained by moving the nozzle or the substrate by means of a xy-moving stage. The basic principle of ink-jet starts with the generation of a pressure wave inside the glass capillary (that is full of the fluid material to be printed) by means of the actuator. This pressure wave implies that, in the orifice of the nozzle,

the fluid surface will be deformed. If the energy of the wave is enough, the fluid close to the surface will have enough kinetic energy to generate a droplet and detach from the nozzle.

Therefore, the generation of the pressure wave is the key point in ink-jet technology. Depending on the actuation method that is used to do it, three different technologies can be distinguished: thermal, piezoelectric or combined ink-jet. In thermal ink-jet, small resistors are located all around the nozzle and rise temporarily and locally the temperature. This gradient of temperature is translated rapidly into a movement in the inner fluid. Piezoelectric ink-jet is based on the application of a mechanical pressure to a part of the nozzle. Again, this gradient converts into a movement of the fluid. The most complete ink-jet systems are formed by both types of actuations, what increases the possibilities to obtain a better control of the droplets generation. Thermal actuation is much cheaper so it is used in the majority of the commercial ink-jet devices, even though it presents some issues, as the fact that the ink is exposed to temperatures in the range of 200°C, what is really high for polymers and resists, implying the necessity of optimization of the solvents and add-ins to the materials to be ink-jetted. For research, piezoelectric actuation is preferred because then it is possible to avoid such high temperatures for the polymers. In addition, it is possible to better control the size of the droplets. However, it is always necessary an optimization of the solvent(s) of the materials to be printed, in order to improve the volatility, solubility, wettability, viscosity and surface tension.

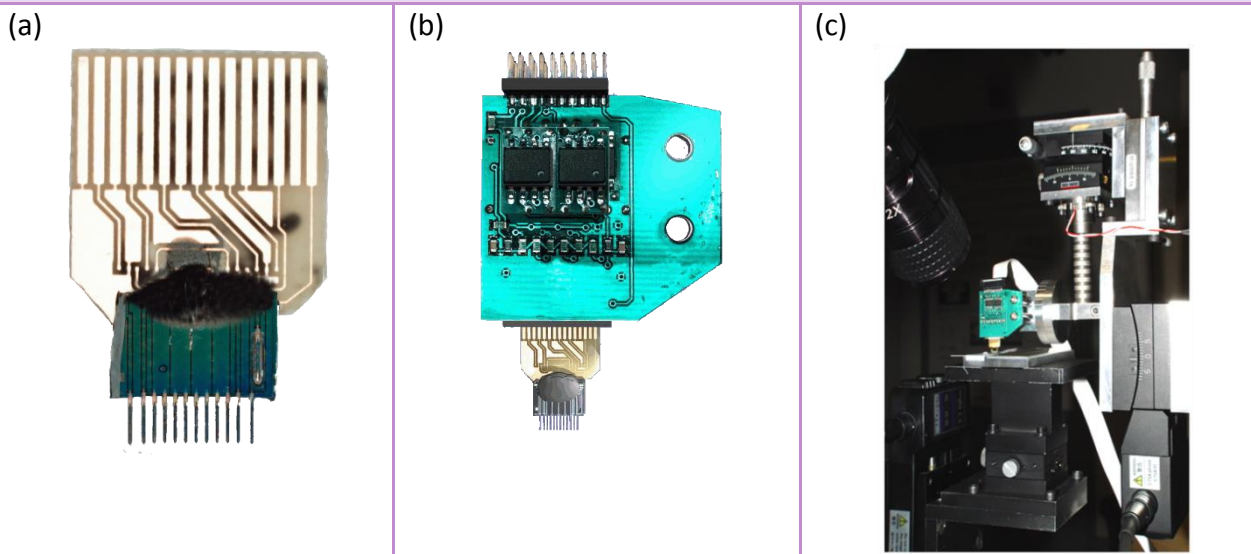
5.2 BIOPLUME SYSTEM

The microfluidics network whose fabrication is presented in this chapter is dedicated to selectively supply liquid to a novel nanospotting device called Bioplume [27, 28]. The work is part of the NaPa project.

Bioplume is a depositing tool which consists of an array of silicon microcantilevers integrating a fluidic channel fixed to a xyz motion control system. It is developed by the Nano-addressing/Nano-biotechnology group of LAAS - CNRS. The main advantages of this system are that it allows the deposition of drops with suitable control of the positioning and homogeneity. In addition, Bioplume can deposit in parallel, multiple depositions at the same time with a single load (the cantilevers also load simultaneously), it allows different substrate materials and the deposition of drops of different size [29].

Bioplume system consists of a chip with the cantilever array (called also Bioplume chip, Figure 5.1.a), an electronic circuitry (Figure 5.1.b) and a mechanical stage (Figure 5.1.c).

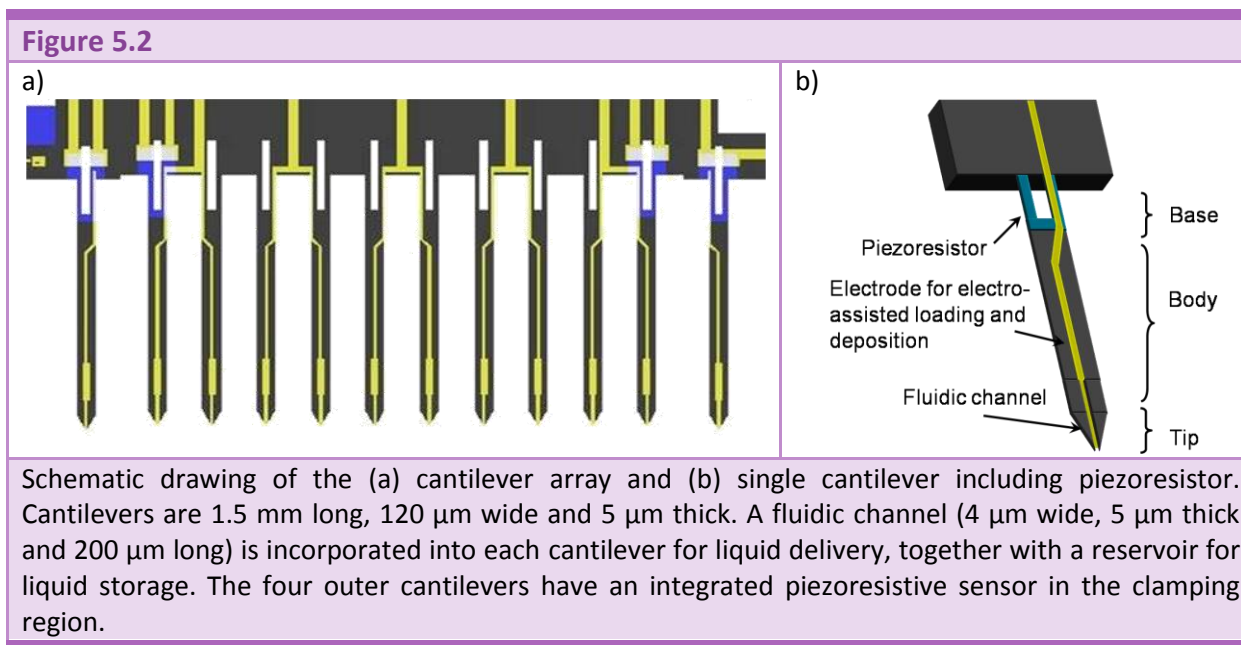
Figure 5.1



(a) Picture of a Bioplume chip, showing the array of silicon cantilevers including the two piezoresistive ones for deflection measurement and alignment control and the electrodes for electrowetting; (b) Picture of a Bioplume chip with an annex electronic circuitry to measure the piezoresistor variation; (c) Picture of the mechanical stage that allows an accurate displacement and tilting of the Bioplume chip.

The Bioplume chip has 12 microcantilevers distributed in an array and a separated reference cantilever (Figure 5.2.a). Of all 12 cantilevers in the array, just the central 10 are employed to load and dispense the liquid, incorporating a channel and a small reservoir for liquid deposition and liquid storage. The channel and reservoir are filled by capillary action.

On the other hand, the first and the last cantilevers of the array are longer than the rest and they include a piezoresistance close to the clamping zone. These two levers are in charge of the control of the trim of the array, meaning that they are used as an alignment sensor, to correct any tilting mismatch between the array and the substrate. These two “*aligner levers*” are 30 μm longer than the rest “*dispensing levers*” which, taking into account that the minimum detectable deflection is around 100 nm, ensures that the substrate is contacted earlier by the outer beams and hence the alignment is done without the dispensing levers touching the substrate.



In addition to the two “alignment” cantilevers, there are two dispensing cantilevers that also hold a piezoresistance in the clamping region. These other two levers are used to measure both the force that the cantilever array is performing to the surface and the time that they are contacting.

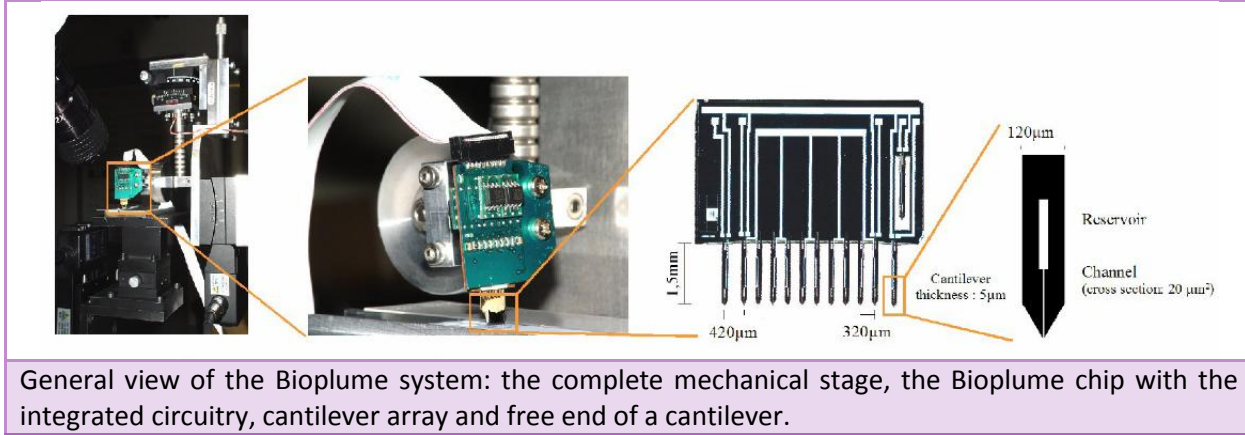
All sensing levers are an important improvement for the reliability in operation of Bioplume, given that they ensure homogeneity of the dispensed droplets, low damage of the substrate and accurate control of drop size. First, without tilt correction printed matrices would not be homogeneous because some levers would be touching in a different way than others (longer time, stronger contact, etc.). Second, a high contact force can damage the substrate if this is

delicate (soft materials, biological samples, etc.). Finally, controlling the contact time between the dispensing tips and the substrate, it is possible to control the size of the droplets, which will depend on that time and the capillary force between the substrate and the dispensed liquid.

The fabricated chips are bonded to PCB supports (Figure 5.1.b) allowing the connections to dedicated electronics readout. This electronic circuitry, based on a modified Wheatstone bridge, allows the measurement of the cantilever deflection through the piezoresistance variations. The signal output from the electronics is recorded while the cantilevers are vertically brought down toward the surface and included in a closed loop for the controllers of the movement.

The cantilever array (Bioplume chip) is fixed on a four-degree-of-freedom moving stage. It can be moved in the X, Y directions (horizontal in-plane movement) by means of step motors. In addition, vertical (Z) displacement and tilt (θ) of the array can be done both by a piezoactuator and a step motor for fine and coarse positioning respectively. Each one of the actuators (motors and piezos) is controlled by a PC thanks to specifically written LabWindows/CVI software.

Figure 5.3



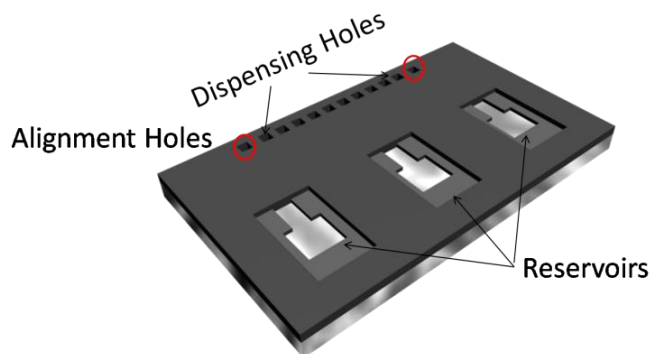
5.3 FABRICATION OF MICROFLUIDIC CHIP

Bioplume system has been presented as a very complete device, and the only part missing up to now is the microfluidics network used to selectively address fluids to each of the levers.

The fluidic network (Figure 5.4) contains 12 holes, one for each cantilever in the array. 10 of them are dedicated to supply liquid to the dispensing cantilevers, whereas the two lateral holes are for the alignment cantilevers and therefore they are not connected to any fluidic channel.

Each dispensing hole is rectangular shaped, with 200 μm long and 100 μm wide. The depth is defined by the thickness of the wafer, in this case 525 μm . The gap separation between two adjacent holes is 120 μm . Three reservoirs which allow easily pipetting supply the liquid to the dispensing holes. The channels, which are patterned in the backside of the wafer and are sealed by glass, drive selectively the liquids from the reservoirs to the dispensing holes.

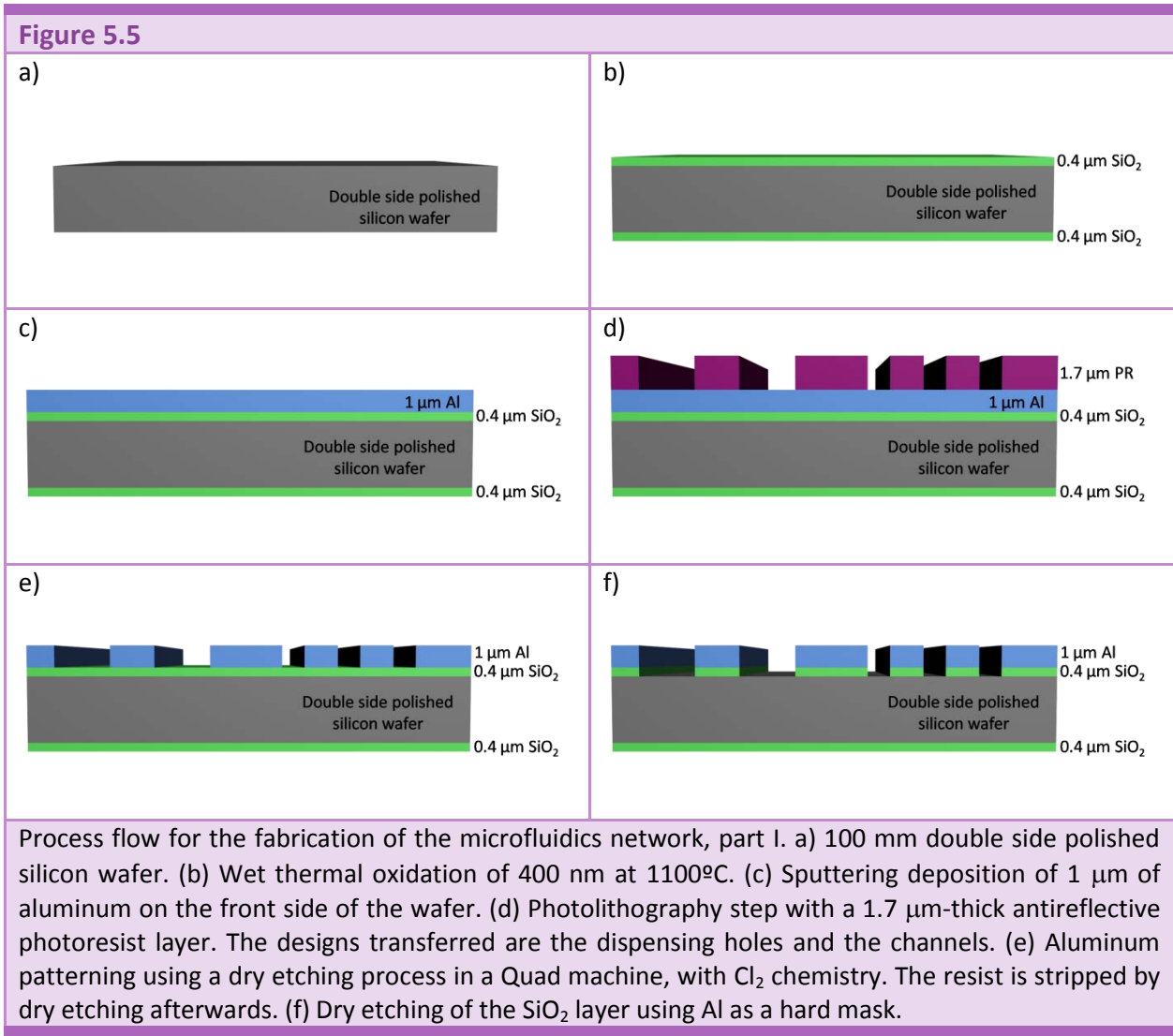
Figure 5.4



Schematic drawing of the microfluidics network used to selectively address the fluids to the cantilevers.

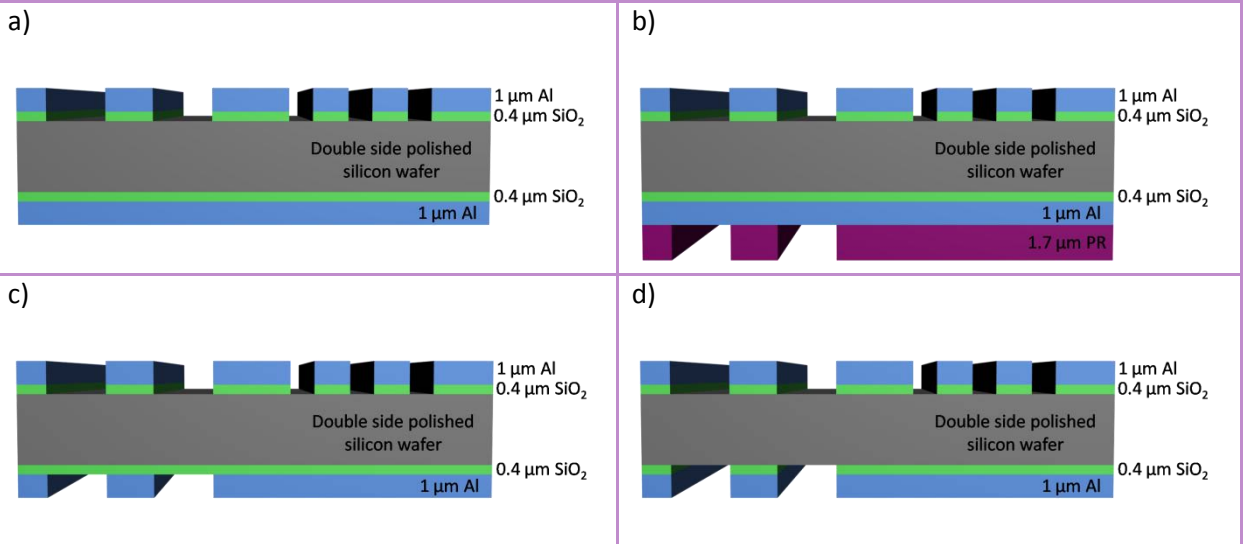
For the fabrication of the microfluidic network standard silicon technology has been used. Starting with a 100 mm in diameter double side polished silicon wafer (Figure 5.5.a), 400 nm of thermal SiO_2 is grown in both sides of the wafer by a wet oxidation at 1100°C (Figure 5.5.b). Then, a 1 μm thick Al layer is deposited by sputtering on the front side of the wafer (Figure 5.5.c). This layer is used as a mask for subsequent etches. A 1.7 μm thick layer of antireflective positive photoresist is then spin coated on top of the Al layer and exposed using standard UV-lithography. The resist is antireflective in order to avoid loss of dimensions due to the Al layer below. In this lithography step (Figure 5.5.d) the channels and dispensing holes are defined. The Al layer is then dry etched using chlorine chemistry and the resist removed afterwards (Figure

5.5.e). Subsequently, SiO₂ is patterned using again a dry etching process and the Al is used as a hard mask (Figure 5.5.f).



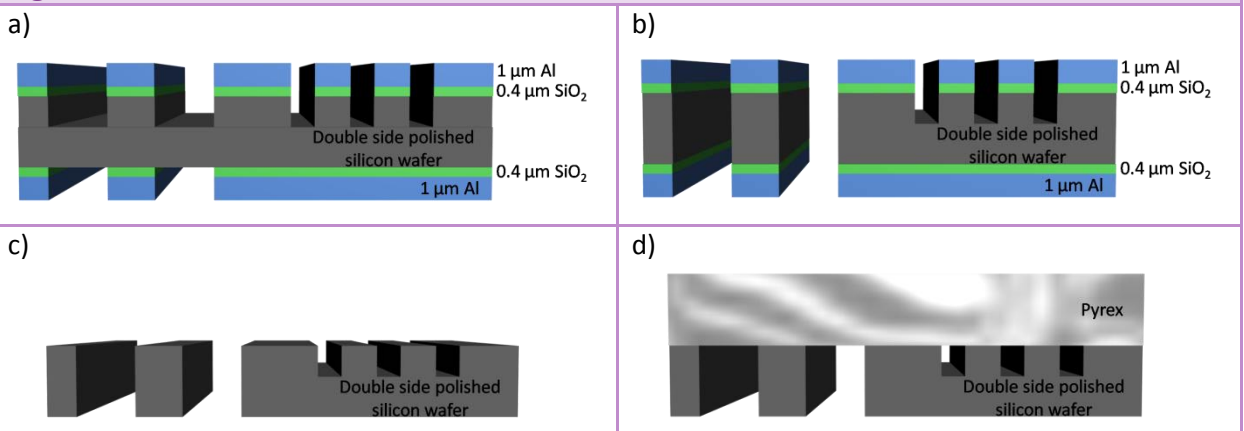
In the subsequent steps, the backside of the wafer is processed in a similar way than that of the front side. First, a 1 μm thick Al layer is deposited by sputtering on the backside of the wafer (Figure 5.6.a). A photolithography step is performed with an antireflective resist. In this case the designs transferred are the dispensing holes and the reservoirs (Figure 5.6.b). The Al layer is then dry etched using chlorine chemistry, the resist removed afterwards (Figure 5.6.c) and then the SiO₂ using again Al as a hard mask (Figure 5.6.d).

Figure 5.6



Process flow for the fabrication of the microfluidics network, part II. (a) Sputtering deposition of 1 μm of aluminum on the backside of the wafer. (b) Photolithography step with a 1.7 μm-thick antireflective photoresist layer. The designs transferred are the dispensing holes and the channels. (c) Aluminum patterning using a dry etching process with Cl₂ chemistry. The resist is stripped by dry etching afterwards. (f) Dry etching of the SiO₂ layer using Al as a hard mask.

Figure 5.7



Process flow for the fabrication of the amicrofluidics network, part III. (a) Partial Deep Reactive Ion Etching (DRIE) of the silicon wafer from the front side using Al as a hard mask and SF₆ and C₄F₈ (Bosch process) as the etching process. (b) Idem from the backside. The wafer is fully etched just in some areas: dispensing holes and some part of the reservoirs. (c) Aluminum and oxide stripping by HF etching. (d) Anodic bonding of a Pyrex wafer to the front side of the wafer in order to seal the microfluidic channels, the dispensing holes and the reservoirs.

Once the aluminum layers are ready in both sides of the wafer, a Deep Reactive Ion Etching (DRIE) is performed from the front side to partially machine the wafer. The silicon is etched using the Bosch process [30, 31]. In this step (Figure 5.7.a) the channels are defined, together with a part of the dispensing holes. Subsequently, the same process is performed from the backside, defining this time the reservoirs and completing the dispensing holes (Figure 5.7.b). The full wafer is only etched in the dispensing holes and in the intersection between the reservoirs and the channels. Finally, the aluminum and the oxide layers are removed by wet etching in HF (Figure 5.7.c), and the wafer is anodic bonded to a pyrex wafer (1000 V, 400°C). Pyrex seals the dispensing holes, the channels and the reservoirs (Figure 5.7.d).

In Figure 5.8 two optical images of the microfluidics network after the fabrication process is finished are shown. The reservoirs with the dispensing holes can be seen in one side of the chip (Figure 5.8.a) whereas some inks can be seen in the microfluidic channels showing that the network is properly working (Figure 5.8.b). The size of the chip is 20 mm wide and 12 mm long. The total amount of liquid that can be loaded in the chip is 13 μl . As the paths are different for the liquid to get from the reservoir to the dispensing holes, the volume of each liquid is slightly different, but approximately from 3-5 μl per channel.

Figure 5.8

a)



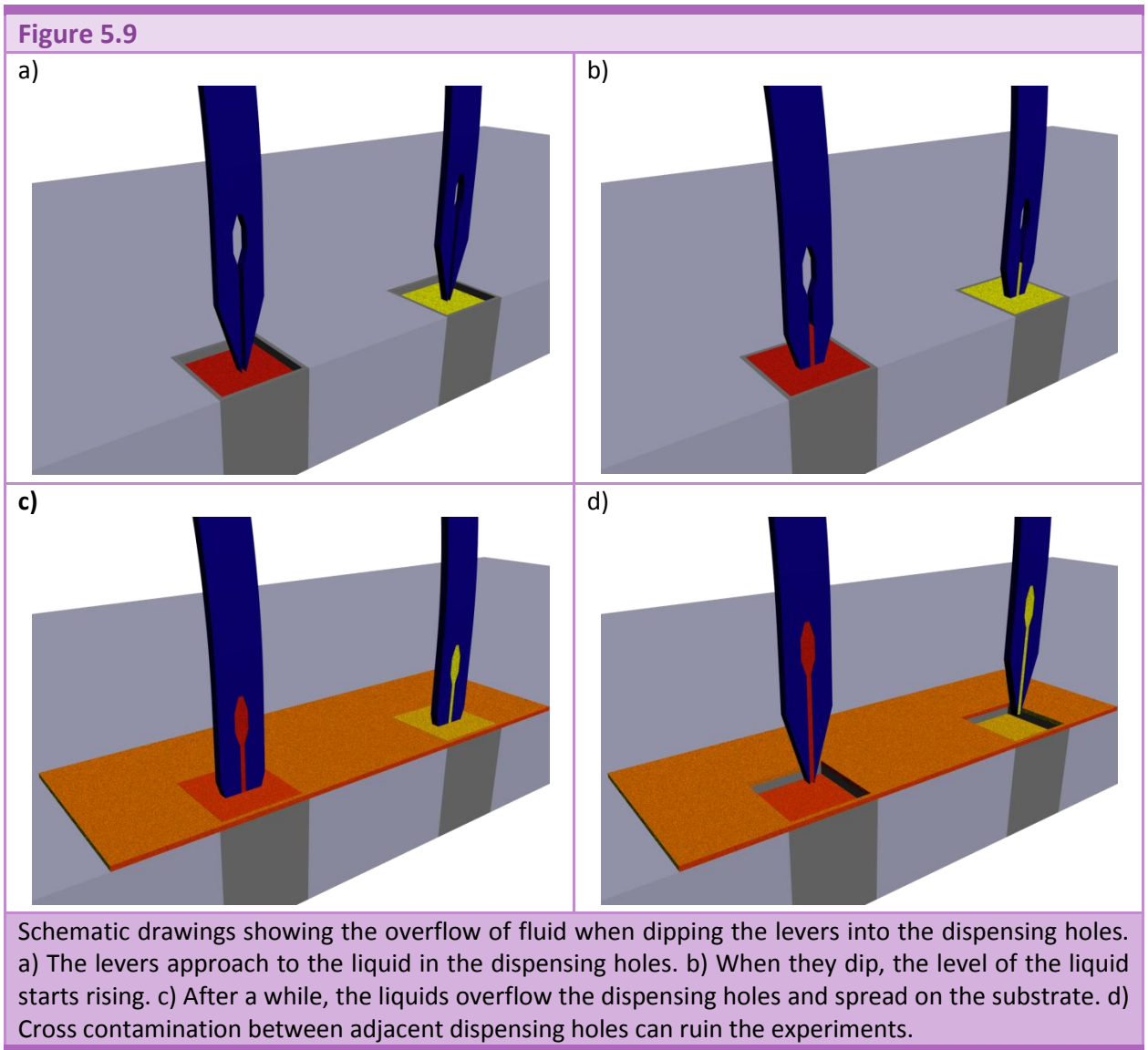
b)



Pictures of a microfluidic network after the fabrication process using silicon technology. (a) Reservoirs and dispensing holes are shown. This side is opened to allow pipette the liquids. (b) Microfluidic channels holding liquid are shown. This side is cover with pyrex.

5.4 HYDROPHOBIC BARRIERS

Although the chip can be considered fully fabricated after the anodic bonding process, a small issue arises, and this is the overflow that will happen while the cantilevers dip into the dispensing holes. The liquid spreads over the silicon wafer causing a cross contamination of the liquid between adjacent holes (Figure 5.9).



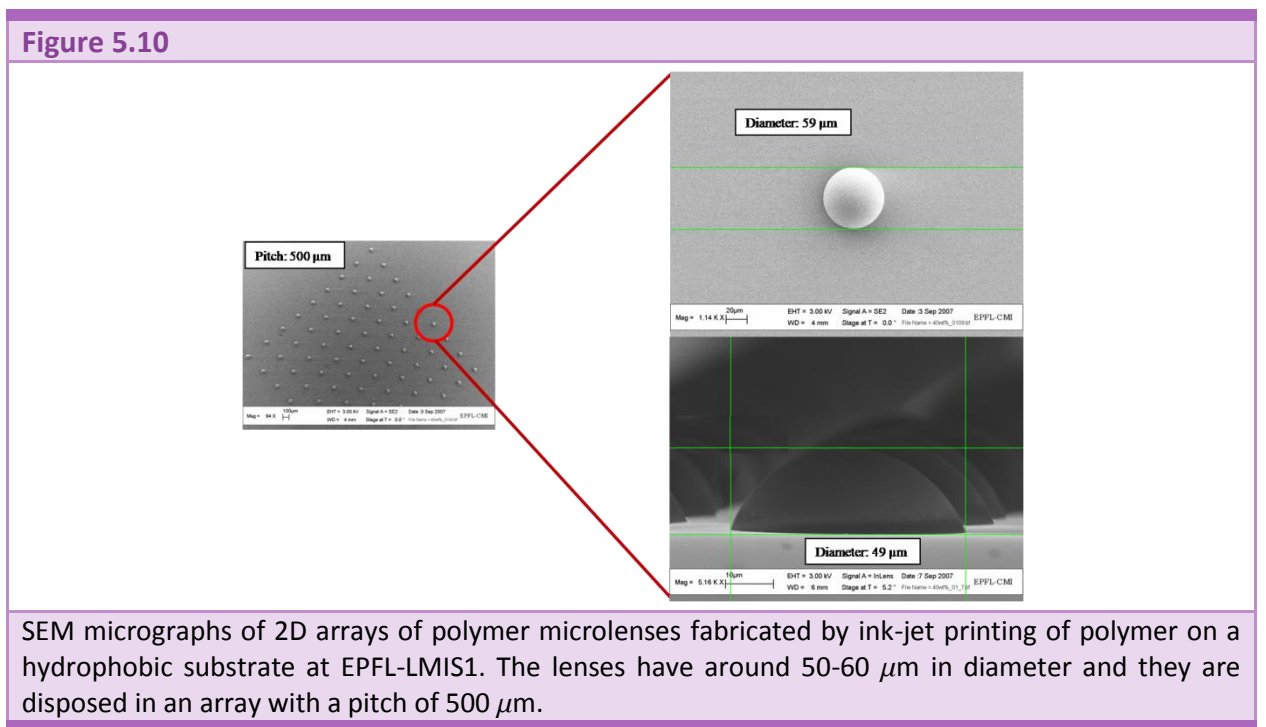
The solution to avoid cross contamination between holes, has been the fabrication of polymeric hydrophobic barriers placed in between holes. These hydrophobic barriers have to be high enough to avoid the liquids intermix.

As the fabrication of the microfluidic network involves a final high temperature step (anodic bonding), definition of the polymer barriers is not possible during the fabrication process. It is also not possible to define them after the fabrication process by photolithography because the resist deposition by spinning would clog the channels avoiding the liquid flow. In consequence, as it has already been commented in the introduction, we have explored two novel methods for polymer structuring: ink-jet printing and soft lithography.

5.4.1 Ink-jet printing

The first method is based on ink-jet printing [17] and its processing was performed in the Ecole Polytechnique Fédérale de Lausanne (EPFL) in the laboratory of Prof. Juergen Brugger (LMIS1).

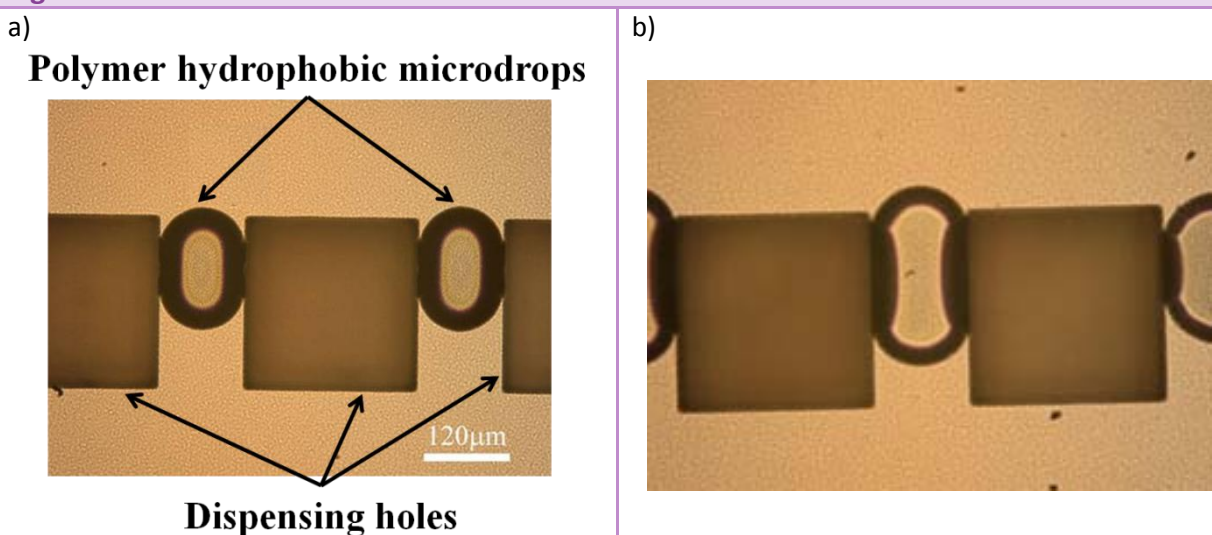
The ink-jet setup used for the experiments consists of a piezo-actuated inkjet printer head (nozzle) coupled to a motorized stage sample holder. The nozzles used are commercially available (Microdrop technologies, Germany) and, in this case, with apertures of approximately 50 μm in diameter. The motorized stage is controlled by dedicated software and allows the motion in x, y and θ directions. Consequently, two dimensional arbitrary polymer drop patterns can be generated, i.e. arrays of lenses for micro-optical devices (Figure 5.10).



Inkjet printing is unique because of its flexibility to define arbitrary patterns on different surfaces and its cleanliness. As it is a non-contact method, it is clear that surfaces with pre-

defined structure can be easily patterned by ink-jet, which makes it an ideal tool to fabricate the hydrophobic barriers between dispensing holes of the microfluidics chip. The main challenge, however, is to align the deposition with the pre-existing patterns on the surface. This is solved in this case by a positioning system with a camera coupled to the motorized stage, and allows the alignment with an accuracy of less than 20 microns.

Figure 5.11

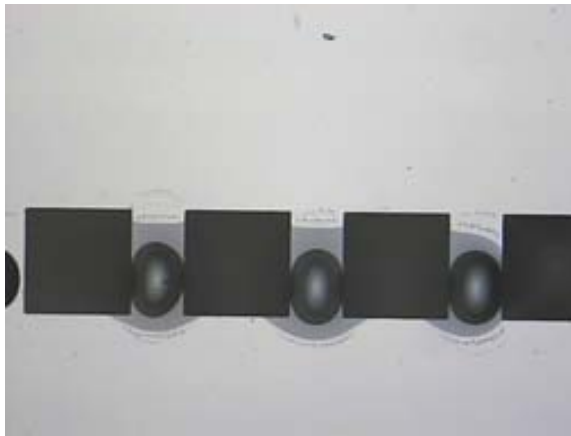


Pictures of the top view of two different chips after the deposition of hydrophobic barriers of SU-8 between dispensing holes.

Different parameters can be changed in order to get a stable drop generation, e.g. voltage of the piezo-actuator, pulse length, frequency of the actuation, nozzle temperature, etc. All those parameters must be tuned each time the nozzle is used, because the inkjet characteristics depend drastically of environmental conditions, and those are not stable enough in the laboratory where the experiments were run.

After finding the optimal parameters and hence stabilize the droplet generation, ink-jet printing was used to dispense five 50 µm sized polymer drops in between two adjacent dispensing holes, resulting in a 120 µm wide barrier (see Figure 5.11). After deposition, the drops were exposed to standard UV lithography (400 mJ/cm²) and baked at 100°C for 15 min (PEB). Two typical examples of the polymeric barriers after exposure and bake are shown in Figure 5.11.

Figure 5.12



Optical image showing that the ink-jetted microdroplets don't stop the liquid intermixing between the dispensing holes.

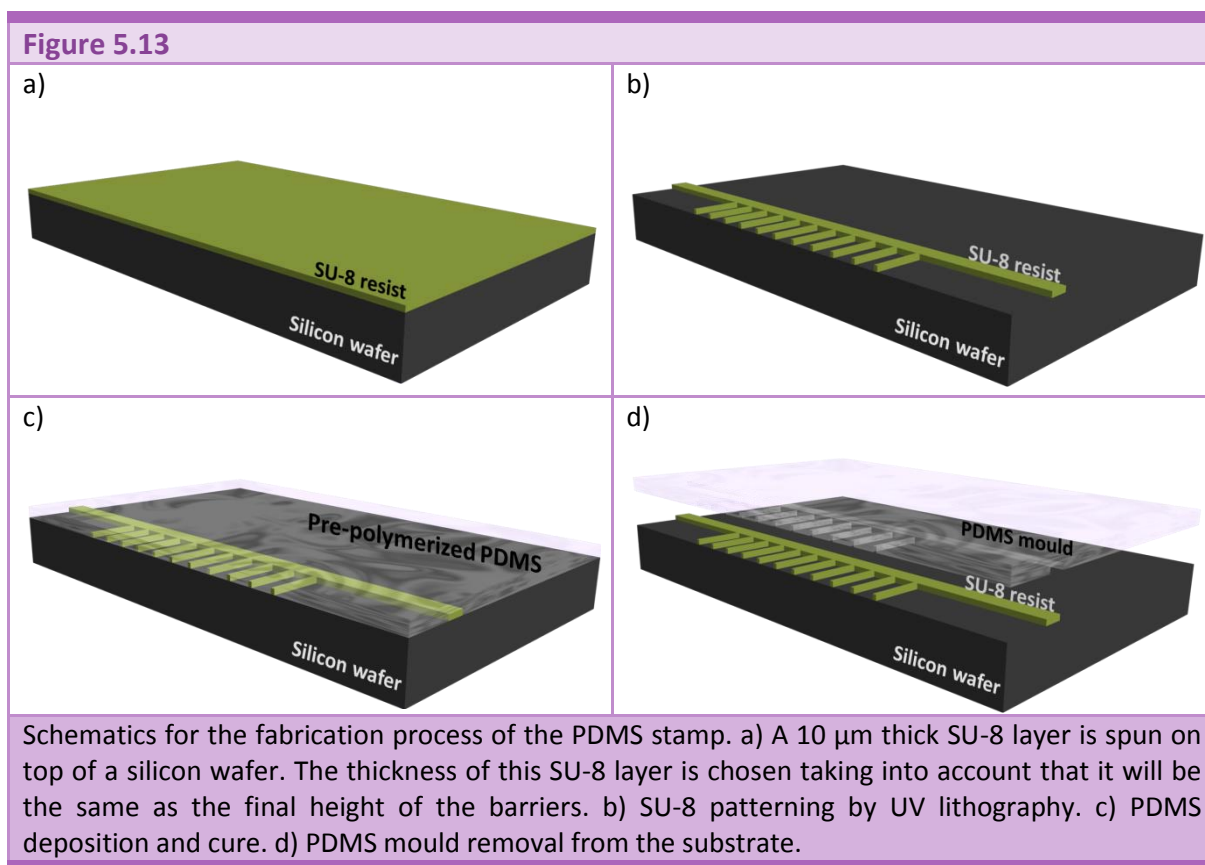
Tests of the microfluidic chip with the ink-jetted microdroplets have been performed. The experiment consists in filling the reservoirs by pipetting with a very low viscous liquid to ease the overflowing in the dispensing holes. In this case isopropanol was used. Figure 5.12 is an optical image of the results obtained. It is clear that the droplets are not enough large to prevent the cross-contamination when the liquid from the dispensing holes are overflowing. As the isopropanol is very volatile, the liquid is disappearing leaving some trace. Probably placing more droplets in the space between dispensing holes this contamination could be avoided.

Although the possibility to fabricate the hydrophobic barriers by means of ink-jet printing of SU-8 (or other related high viscous polymers) has been shown, this option was soon discarded as the optimum fabrication tool. The main problem consists in the fact that the microfluidics chip is fabricated has a hydrophilic surface (necessary to allow a good flow through the channels). This hydrophilic surface yields a low contact angle of the droplets, what implies that they are hard to confine in a small area and, at the same time, it is difficult to build high barriers out of droplets. For this reason a second option, i.e. soft lithography, was used.

5.4.2 Soft-lithography

The soft-lithography approach to build the hydrophobic barriers is based on Micromolding in Capillaries (MIMIC) [10, 11]. Channels in the PDMS stamp will be filled with a polymer resist by capillary action, which in turn will form the barriers.

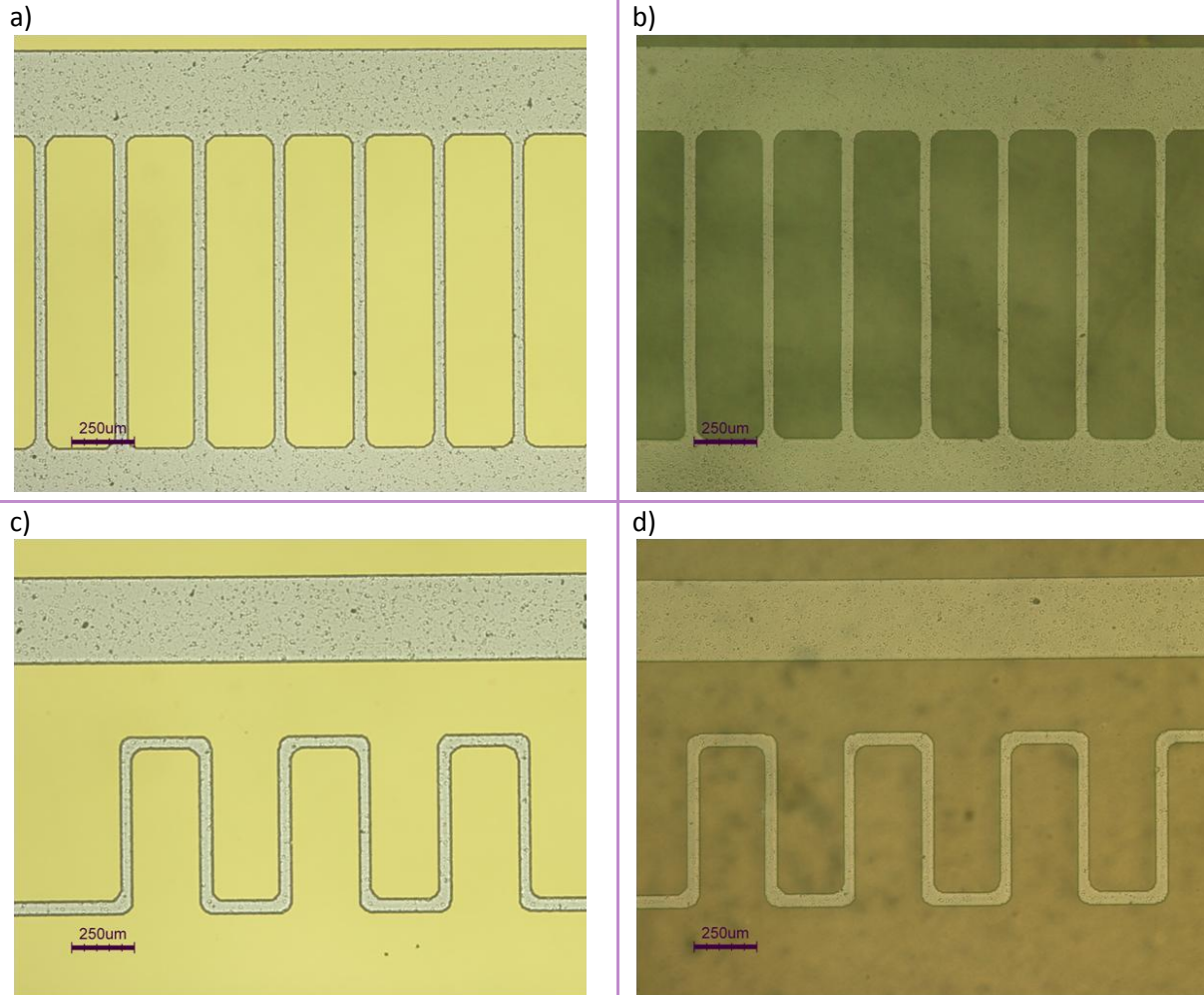
The PDMS stamp is fabricated from a SU-8 master. After spin coating this resist on a bare silicon wafer (Figure 5.13.a) and selectively expose it to UV-light, it is developed in PGMEA, obtaining the master for PDMS stamps (Figure 5.13.b). The thickness of the SU-8 is selected so as to be equal to the final height of the polymer barriers. Once the master is ready, pre-polymerized PDMS in a 1:10 ratio is poured on the master in order to replicate the complementary pattern (Figure 5.13.c). Then, PDMS is thermally cured at 95°C for 5 hours. Finally, the mould is released from the substrate by physical removal (Figure 5.13.d).



Several different channel designs were fabricated and tested. This was motivated because it was not known a priori which kind of design would be working better both for the hydrophobic

barriers fabrication or their reliability. In Figure 5.14, two different designs for the barriers are shown.

Figure 5.14

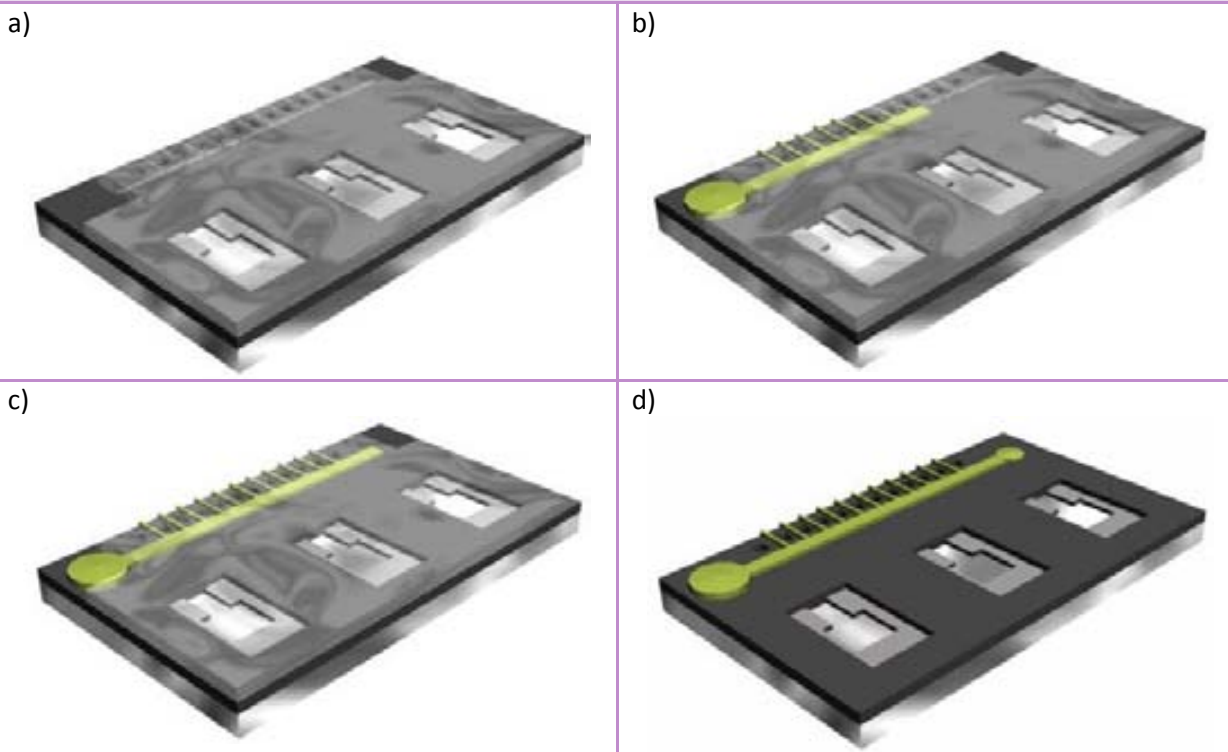


Optical images of the fabricated masters and moulds. (a) and (c) show a 10 μm thick SU-8 layer patterned on top of a silicon wafer, while (b) and (d) show their respective PDMS moulds. Design in (c) did not work properly for the barriers fabrication.

Once the PDMS mould is fabricated, it is necessary to align it to the pre-patterned front-side of the microfluidic chip (Figure 5.15.a). This alignment was done using a KarlSuss MA6. After the alignment, a drop of polymer is placed at the beginning (inlet) of the main channel and, by capillary action, all the channels are filled (Figure 5.15.b and c). The polymer used for the fabrication of these devices is a low viscous epoxy-based negative tone resist developed for electron beam lithography [32]. After the complete filling of the PDMS mould channels, the polymer was exposed by UV-light ($190 \text{ mJ}/\text{cm}^2$, i-line) and a post exposure bake (95°C) was

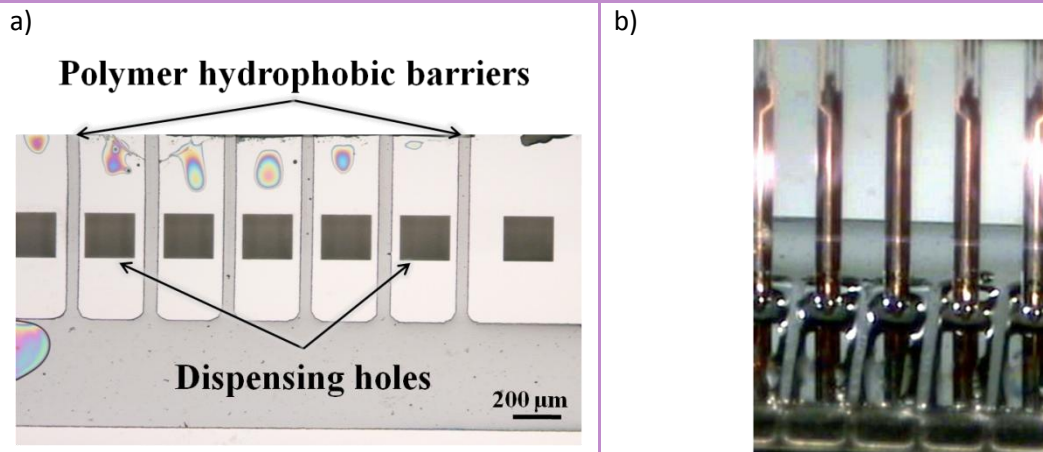
performed subsequently. Once the resist was hard, the mould was removed from the substrate, leaving on the microfluidics chip the hydrophobic barriers (Figure 5.15.d).

Figure 5.15



Schematics for the fabrication process of the hydrophobic barriers using MIMIC. a) The PDMS stamp is aligned to the microfluidic chip, already finished. b) A drop of low-viscous epoxy resist is deposited close to the inlet of the channel of the PDMS mould. c) Capillary forces drive the resist into the channel until it goes out through the outlet of the mould. Resist is exposed to UV-light in order to harden the polymer. d) PDMS mould removal from the substrate leaves the hydrophobic barriers on the chip.

The features that define the channels in the PDMS were 10 μm deep and 60 μm wide. In Figure 5.16.a, it can be seen that the barriers made with the hydrophobic polymer are successfully defined, showing that it is a very clean process that avoids clogging of the dispensing holes with hydrophobic polymer and makes very homogeneous barriers. The height of the barriers is of 10 μm (measured by a profilometer), which means that the depth of the channels in the PDMS mould is kept after the MIMIC process. In Figure 5.16.b, an actual operation example is shown, where the dispensing cantilevers dip into the dispensing holes and no intermixing is seen.

Figure 5.16

Pictures of a) top view of a microfluidics chip with the hydrophobic layers defined by the MIMIC process and b) actual operation with the dispensing cantilevers dipping into the dispensing hole with no appreciable intermixing of the fluid.

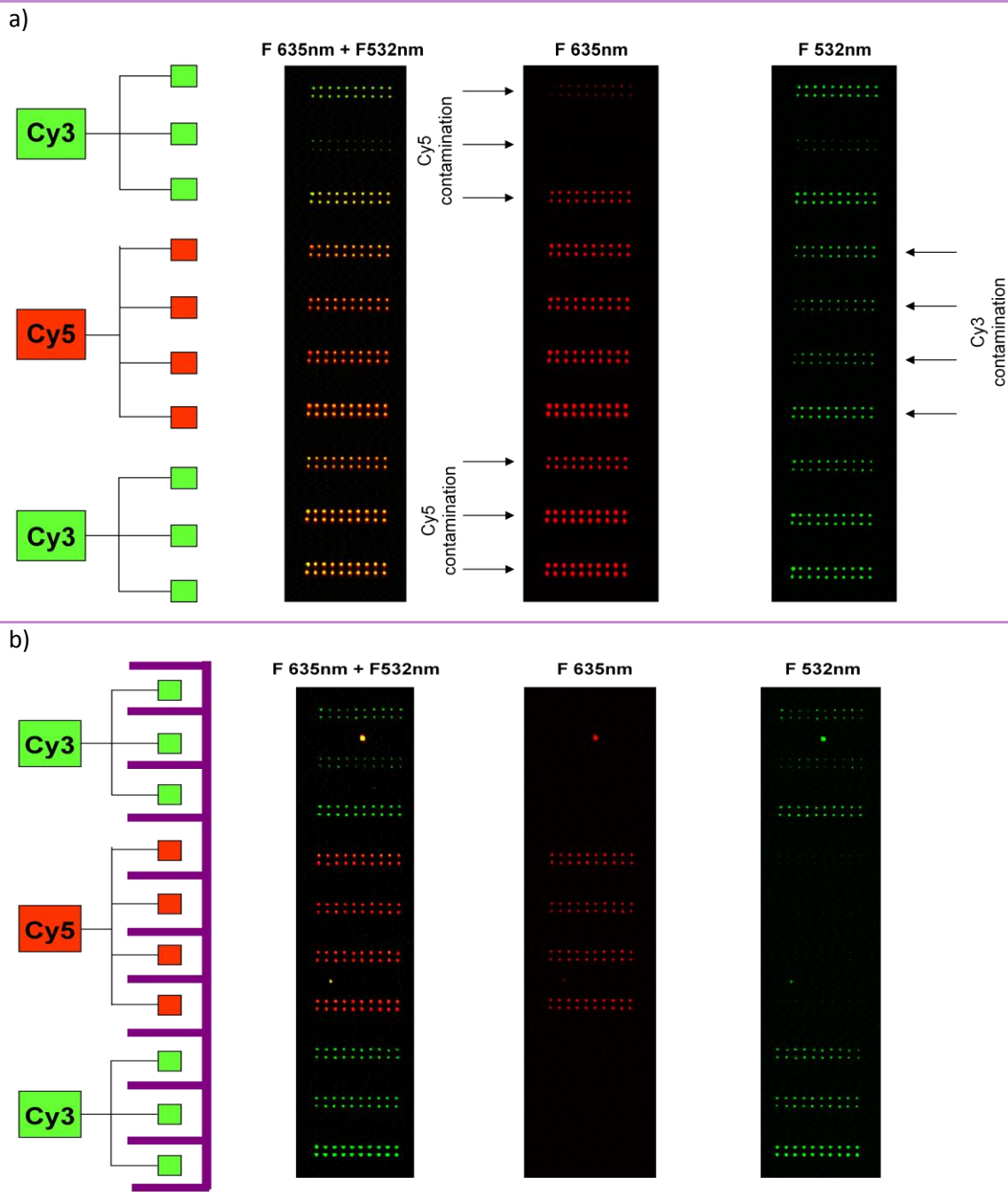
5.5 VALIDATION TEST

In order to test the correct performance of the hydrophobic barriers fabricated by soft lithography, a validation test was made. The reservoirs of two different chips (with and without hydrophobic barriers) were filled with 2 DNA solution labelled with Cy3 and Cy5 fluophores. Cy3 has green fluorescence ($\lambda = 532$ nm) and Cy5 has red fluroescence ($\lambda = 635$ nm). Then, the cantilevers were dipped in the reservoirs and matrices of spots printed. The results are shown in Figure 5.17.

Figure 5.17.a shows the results for a microfluidic chip without the hydrophobic barriers. Two of the reservoirs (at the edge) are filled with the Cy3 labelled DNA and the middle reservoir is filled with Cy5 labelled DNA. Cross contamination is evidenced when either the green or the red light is filtered and brilliant dots are distributed uniformly. In such a case, if there was no contamination, just some lines of dots should be visible.

On the other hand, Figure 5.17.b shows the same experiment but performed using a microfluidics chip with hydrophobic barriers. In this case, we observe a perfect correlation between reservoir loading and colour of the matrices, demonstrating that the hydrophobic barriers assures no cross contamination due to the volume of liquid displaced when the cantilevers are dipped in the dispensing holes.

Figure 5.17



Pictures showing the validation test performed on the microfluidics chips. The reservoirs are filled with 2 DNA solutions labeled with Cy3 and Cy5 fluorophores. Cy3 has green fluorescence and Cy5 red fluorescence. The cantilevers are dipped inside the dispensing holes, causing the liquid overflow and matrices of spots are printed. a) Corresponds to a microfluidic chip without the hydrophobic barriers. It can be seen that with a green filter there are Cy5 cross contamination and with a red filter also is proof that there is Cy3 cross contamination. b) Corresponds to the same test on a microfluidic chip with hydrophobic barriers. The filtered images show no cross contamination between dispensing holes.

5.6 CONCLUSIONS

A microfluidics network has been fabricated in order to allow the selective load of an array of cantilevers for dispensing of liquid at the nanoscale. To avoid cross-contamination between the different dispensing holes, the need of hydrophobic barriers separating the holes has been shown.

Two novel methods have been described for the fabrication of the polymer hydrophobic barriers: ink-jet printing and soft lithography. Ink-jet printing allows high flexibility and a selective deposition of the polymer. Using soft-lithography, a better control of the barrier dimensions can be achieved. In addition, this technique is scalable, that is to say, barriers of several heights can be achieved and high aspect ratio structures can be generated, which can be crucial for the optimum performance of the final device.

Finally, validation tests have been presented showing that the fabricated barriers avoid the cross-contamination and allows a completely selective deposition.

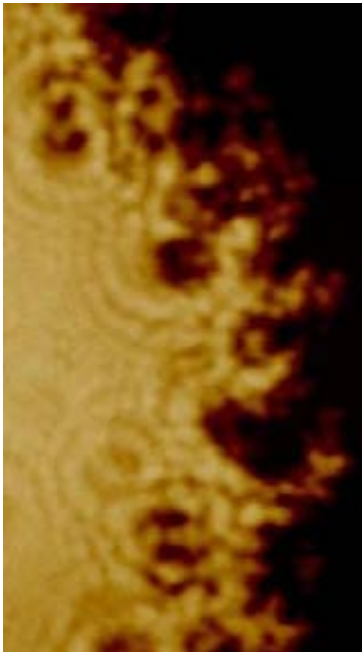
5.7 REFERENCES

1. B.H. Weigl and P. Yager
"Microfluidics - Microfluidic diffusion-based separation and detection".
Science, 1999, **283**(5400), 346-347.
2. G.M. Whitesides
"The origins and the future of microfluidics".
Nature, 2006, **442**(7101), 368-373.
3. D.R. Reyes, D. Iossifidis, P.A. Auroux, and A. Manz
"Micro total analysis systems. 1. Introduction, theory, and technology".
Analytical Chemistry, 2002, **74**(12), 2623-2636.
4. P.A. Auroux, D. Iossifidis, D.R. Reyes, and A. Manz
"Micro total analysis systems. 2. Analytical standard operations and applications".
Analytical Chemistry, 2002, **74**(12), 2637-2652.
5. A. Manz, N. Graber, and H.M. Widmer
"Miniaturized total chemical-analysis systems - a novel concept for chemical sensing".
Sensors and Actuators B-Chemical, 1990, **1**(1-6), 244-248.
6. A. Manz, J.C. Fettingler, E. Verpoorte, H. Ludi, H.M. Widmer, and D.J. Harrison
"Micromachining of Monocrystalline Silicon and Glass for Chemical-Analysis Systems - a Look into Next Century Technology or Just a Fashionable Craze".
TRAC-Trends in Analytical Chemistry, 1991, **10**(5), 144-149.
7. D.J. Harrison, K. Fluri, K. Seiler, Z.H. Fan, C.S. Effenhauser, and A. Manz
"Micromachining a Miniaturized Capillary Electrophoresis-Based Chemical-Analysis System on a Chip".
Science, 1993, **261**(5123), 895-897.
8. D.C. Duffy, J.C. McDonald, O.J.A. Schueller, and G.M. Whitesides
"Rapid prototyping of microfluidic systems in poly(dimethylsiloxane)".
Analytical Chemistry, 1998, **70**(23), 4974-4984.
9. H. Becker and L.E. Locascio
"Polymer Microfluidic Devices".
Talanta, 2002, **56**(2), 267-287.
10. Y.N. Xia and G.M. Whitesides
"Soft lithography".
Annual Review of Materials Science, 1998, **28**, 153-184.
11. X.M. Zhao, Y.N. Xia, and G.M. Whitesides
"Soft lithographic methods for nano-fabrication".
Journal of Materials Chemistry, 1997, **7**(7), 1069-1074.
12. G.M. Whitesides, A. Kumar, H.A. Biebuyck, N.L. Abbott, and P.A. Dimilla
"Self-Assembled Monolayers and Their Uses".
Abstracts of Papers of the American Chemical Society, 1994, **207**, 373-PHYS.

13. A. Kumar and G.M. Whitesides
"Features of Gold Having Micrometer to Centimeter Dimensions Can Be Formed through a Combination of Stamping with an Elastomeric Stamp and an Alkanethiol Ink Followed by Chemical Etching".
Applied Physics Letters, 1993, **63**(14), 2002-2004.
14. G.P. Lopez, H.A. Biebuyck, R. Harter, A. Kumar, and G.M. Whitesides
"Fabrication and Imaging of 2-Dimensional Patterns of Proteins Adsorbed on Self-Assembled Monolayers by Scanning Electron-Microscopy".
Journal of the American Chemical Society, 1993, **115**(23), 10774-10781.
15. G.P. Lopez, P.A. Dimilla, A. Kumar, R. Harter, and G.M. Whitesides
"Use of Self-Assembled Monolayers of Alkanethiolates on Gold for the Study and Manipulation of Interactions of Proteins and Cells with Solid-Surfaces".
Journal of Cellular Biochemistry, 1994, 250-250.
16. J. Drelich, J.D. Miller, A. Kumar, and G.M. Whitesides
"Wetting Characteristics of Liquid-Drops at Heterogeneous Surfaces".
Colloids and Surfaces A-Physicochemical and Engineering Aspects, 1994, **93**, 1-13.
17. Kamphoef.Fj
"Ink Jet Printing".
IEEE Transactions on Electron Devices, 1972, **19**(4), 584.
18. T.W. Shield, D.B. Bogy, and F.E. Talke
"Drop Formation by Dod Ink-Jet Nozzles - a Comparison of Experiment and Numerical-Simulation".
IBM Journal of Research and Development, 1987, **31**(1), 96-110.
19. EPSON
"EPSON webpage".
<http://www.epson.com>, 2007.
20. H.P. Lang, M.K. Baller, R. Berger, C. Gerber, J.K. Gimzewski, F.M. Battiston, P. Fornaro, J.P. Ramseyer, E. Meyer, and H.J. Guntherodt
"An artificial nose based on a micromechanical cantilever array".
Analytica Chimica Acta, 1999, **393**(1-3), 59-65.
21. D. Ramos, J. Tamayo, J. Mertens, M. Calleja, and A. Zaballos
"Origin of the response of nanomechanical resonators to bacteria adsorption".
Journal of Applied Physics, 2006, **100**(10), -.
22. P. Beecher, P. Servati, A. Rozhin, A. Colli, V. Scardaci, S. Pisana, T. Hasan, A.J. Flewitt, J. Robertson, G.W. Hsieh, F.M. Li, A. Nathan, A.C. Ferrari, and W.I. Milne
"Ink-jet printing of carbon nanotube thin film transistors".
Journal of Applied Physics, 2007, **102**(4), -.
23. R. Dagani
"Polymer transistors: Do it by printing - Ink-jet technique may hasten advent of low-cost organic electronics for certain uses".
Chemical & Engineering News, 2001, **79**(1), 26-27.
24. H. Ago, K. Murata, M. Yumura, J. Yotani, and S. Uemura
"Ink-jet printing of nanoparticle catalyst for site-selective carbon nanotube growth".
Applied Physics Letters, 2003, **82**(5), 811-813.

25. M. Mott, J.H. Song, and J.R.G. Evans
"Microengineering of ceramics by direct ink-Jet printing".
Journal of the American Ceramic Society, 1999, **82**(7), 1653-1658.
26. T. Okamoto, T. Suzuki, and N. Yamamoto
"Microarray fabrication with covalent attachment of DNA using Bubble Jet technology".
Nature Biotechnology, 2000, **18**(4), 438-441.
27. T. Leichle, D. Saya, J.B. Pourciel, F. Mathieu, L. Nicu, and C. Bergaud
"Liquid loading of silicon-based cantilevers using electrowetting actuation for microspotting applications".
Sensors and Actuators A-Physical, 2006, **132**(2), 590-596.
28. P. Belaubre, M. Guirardel, G. Garcia, J.B. Pourciel, V. Leberre, A. Dagkessamanskaia, E. Trevisiol, J.M. Francois, and C. Bergaud
"Fabrication of biological microarrays using microcantilevers".
Applied Physics Letters, 2003, **82**(18), 3122-3124.
29. T. Leichle, M.M. Silvan, P. Belaubre, A. Valsesia, G. Ceccone, F. Rossi, D. Saya, J.B. Pourciel, L. Nicu, and C. Bergaud
"Nanostructuring surfaces with conjugated silica colloids deposited using silicon-based microcantilevers".
Nanotechnology, 2005, **16**(4), 525-531.
30. F. Laermer and A. Urban
"Challenges, developments and applications of silicon deep reactive ion etching".
Microelectronic Engineering, 2003, **67-8**, 349-355.
31. G. Villanueva, J.A. Plaza, A. Sanchez, K. Zinoviev, F. Perez-Murano, and J. Bausells
"DRIE based novel technique for AFM probes fabrication".
Microelectronic Engineering, 2007, **84**(5-8), 1132-1135.
32. C. Martin, G. Rius, A. Llobera, A. Voigt, G. Gruetzner, and F. Perez-Murano
"Electron beam lithography at 10 keV using an epoxy based high resolution negative resist".
Microelectronic Engineering, 2007, **84**(5-8), 1096-1099.

Chapter 6. AFM BASED FABRICATION



Scanning Probe Lithography (SPL) has shown itself to be a unique tool for materials structuring and patterning with nanometer precision. Due to its nanoscale positioning and imaging capability, AFM nanolithography is uniquely able to create site-specific and localized functional structures. Moreover, the morphological and physical properties of patterns formed can be immediately characterized with AFM [1]. The main disadvantage that can be attributed to AFM nanolithography is its intrinsic low throughput, but it can be reduced either if it is used in combination with another lithographic technique or if integrated arrays of tips, which can write in parallel, are incorporated.

In this Chapter, the performance of AFM lithography on polymers, like PMMA and epoxy based resist thin layers, is studied. A new lithographic method is described which it is based on the direct local removal of thin, non-exposed, polymer layers. Those polymers can be patterned using other lithographic techniques like EBL, NIL or UV lithography, which can be used in combination with AFM lithography in order to pattern the largest areas, where resolution is not an issue.

6.1 INTRODUCTION

Since the origin of the Atomic force microscopy (AFM) in 1986 a large amount of papers are published every year showing new techniques and capabilities, demonstrating its versatile application that can be used in many research fields. One of these applications is the AFM nanolithography. AFM nanolithography has shown itself to be a unique tool for materials structuring and patterning with nanometer precision. This technique can be applied to a wide range of materials and in different media (liquid, air or vacuum). Due to its nanoscale positioning and imaging capability, AFM nanolithography is uniquely able to create site-specific and localized functional structures. Moreover, the morphological and physical properties of patterns formed can be immediately characterized with AFM. This combined fabrication and characterization function in AFM nanolithography allow convenient in situ and in-line pattern creation and characterization.

The limitations are the intrinsic low throughput (which prevents its industrial application) and the short lifetime of the tip. Nevertheless, notable improvements in reliability and throughput of the technique have been achieved through the use of dynamic mode oxidation [1-3] and parallel tip arrays [4, 5].

Numerous AFM-based lithographic techniques have been developed. Generally, these techniques can be classified into two groups in terms of their operational principles: force-assisted AFM nanolithography and bias-assisted AFM nanolithography. In force-assisted AFM nanolithography, a large force is applied to the tip for pattern fabrication, and the tip-surface interaction is mainly mechanical. For bias-assisted AFM nanolithography, the AFM tip is biased to create a localized electric field in the regime of 10^8 V/m to 10^{10} V/m, and the tip acts as a nanoscale electrode for current injection or collection.

6.1.1 Force-assisted AFM nanolithography

As it has been introduced, in force-assisted AFM nanolithography, a large force is applied to the tip for pattern fabrication, and the tip-surface interaction is mainly mechanical. During force-assisted nanolithography, forces larger than those used for AFM imaging are loaded onto the tip. Typical methods in this category include mechanical indentation [6] and plowing [6], thermomechanical writing [7], nanomanipulation [8], and dip-pen nanolithography (DPN) [9]. The initially featureless surface is then patterned by mechanically scratching [10], pulling, or pushing the surface atoms and molecules with the probe. In DPN, instead of manipulating the

existing molecules on the surfaces, the tip is used as a nanoscale pen to directly deposit collections of ink materials onto the substrate to define a functional structure.

6.1.1.1 Mechanical indentation

Indentation is the simplest way for single structure formation in which the tip is immobilized at a specific surface site, and a large force is then applied to the tip to indent the surface. As the tip approaches the sample surface, structures are created by elastic and plastic deformations of the substrate.

Nanoindentation is performed in three simple steps (Figure 6.1), the AFM tip must be first lowered into contact with the sample (Figure 6.1.a), then indented into the surface (Figure 6.1.b), and finally lifted off the sample surface (Figure 6.1.c).

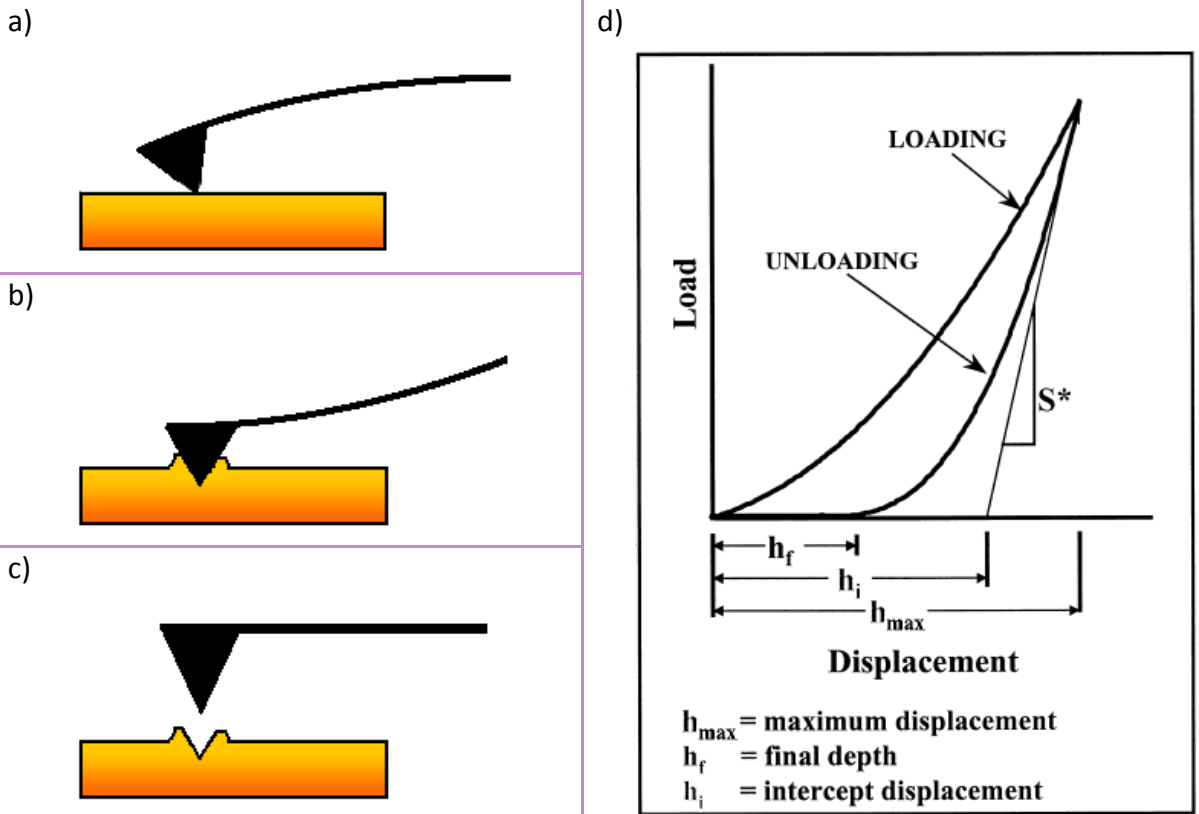
The most crucial parameter in indentation is the force applied between probe and substrate. This, together with tip shape and hardness and thickness of the substrate to be patterned, determines the size and depth of the holes produced in it. The stronger the tip is pressed into the substrate, the deeper the tip goes and, therefore, the diameter of the hole is larger. In addition, more resist has to be displaced and consequently more material is displaced out of the hole and left around it as a bulge.

The feasibility of indentation as a nanofabrication technique will depend on the difference between the hardness of tip and substrate material and on the force that is necessary to exert to actually deform the substrate. For the first point, using diamond or diamond covered AFM tips would reduce tip weariness but would mean an increase in the cost and resolution. Therefore, the most suitable materials to perform nanoindentation on are the softest ones.

In addition, as the force that can be applied by an AFM (in a controlled way) is limited by the elastic constant of the cantilever together with the range of the piezoelectric, that implies that the most compliant materials are the most suited for this application. In Figure 6.1.d the most important parameters used in indentation analysis are represented.

Polymers are much softer than silicon. In addition, Young's moduli are lower than most of the so-called solid state materials (metals, ceramics, etc.) which implies that the forces needed to indent a polymer will be much smaller. These two points demonstrate that polymers are, in principle, convenient materials to perform fabrication based on nanoindentation.

Figure 6.1



Mechanical indentation mechanism. a) AFM tip is first lowered into contact with the sample, b) then the tip indents into the surface and finally c) the tip is lifted off the sample surface. d) Load-distance curve in which several important parameters used in the indentation analysis are illustrated. S^* is the total system stiffness, h_{max} is the maximum loading point, as far as the tip gets inside the surface, h_f is the final unloading depth and h_i is related with the contact depth and it is defines as the intercept displacement [11].

6.1.1.2 Thermomechanical writing

In thermomechanical writing, a resistively heated AFM probe writes a data bit by scanning over a polymer surface. The combined heat and mechanical force of the tip causes the polymer to soften and flow, thus facilitating the writing of data bits in a storage medium. This technique was pioneered by IBM, and systematic descriptions on its working principles and applications can be found in their numerous publications [12-15].

In this method, an electrical current is passed through the cantilever and a large force is loaded on the hot tip to indent the polymer medium. The tip is heated to a relatively high temperature (~ 400 °C), the tip has been pressed into the polymer to increase the volume of softened

polymer and hence the bit a size. A hard Si substrate prevents the tip from penetrating farther than the film thickness, and it enables more rapid transport of heat away from the heated region due to the higher thermal conductivity of Si. By coating a 40 nm thick PMMA layer on Si, bit sizes ranging from 10 nm to 50 nm can be obtained [14].

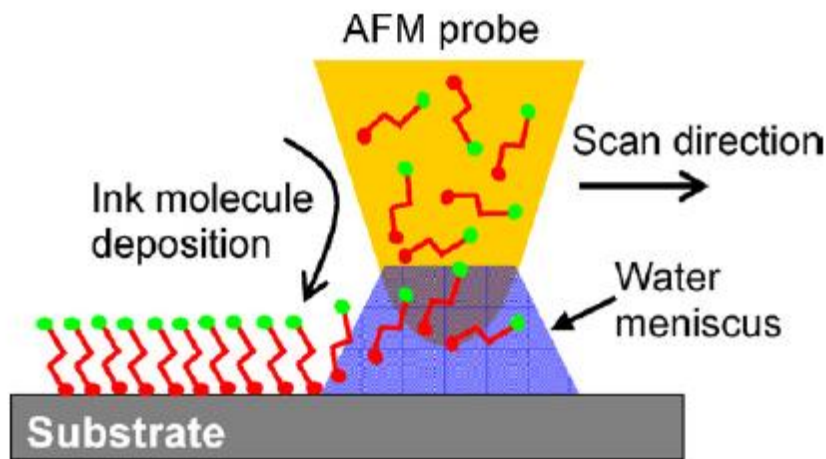
Finally, it is also remarkable that thermomechanical writing is a reversible nanofabrication technique in which data bits can be written, erased, and re-written. Data erasing is simply achieved by thermal reflow of the storage field as a whole.

6.1.1.3 Manipulation

In AFM nanoscopic manipulation, the tip is used to mechanically cut, push, and transport materials to form desired patterns on a substrate. The materials manipulated by AFM range from single atoms, nanoparticles, nanocrystals and nanotubes to biological molecules such as DNA [16, 17]. The manipulations can be operated in contact, tapping and non-contact modes with the feedback loop on or off.

One of the most popular technique belonging to this group is the Dip-pen nanolithography (DPN) [9]. DPN is an AFM-based direct-write lithographic technique in which the AFM probe is used as a pen to directly deliver materials (inks) to a nanoscopic region on a target substrate. In most cases, the transport of ink molecules from the tip to the substrate is mediated by a water meniscus which is formed through capillary condensation. Depending on the selection of ink molecules, DPN is capable of creating structures made of various materials such as metal, inorganic compounds, organic molecules, and biological species.

Figure 6.2



Schematic showing the transport of ink from the AFM tip to the substrate through the water meniscus [9].

6.1.2 Bias-assisted AFM nanolithography

In biased-assisted AFM nanolithography, a bias is applied to the AFM probe to create a localized electric field in the nanometer-sized tip–sample gap. Since the gap is usually less than a few nanometers, a moderate tip bias of several volts would generate a field of 10^8 V/m to 10^{10} V/m. Such an extremely high field can initiate various physical and chemical processes which facilitate pattern formation through field emission, charge injection, Joule heating, electrostatic attraction, explosive discharge, and electrochemical reactions. Techniques such as anodic oxidation, electrochemical deposition and electrochemical modification nanolithography belong to this group.

6.1.2.1 Anodic oxidation

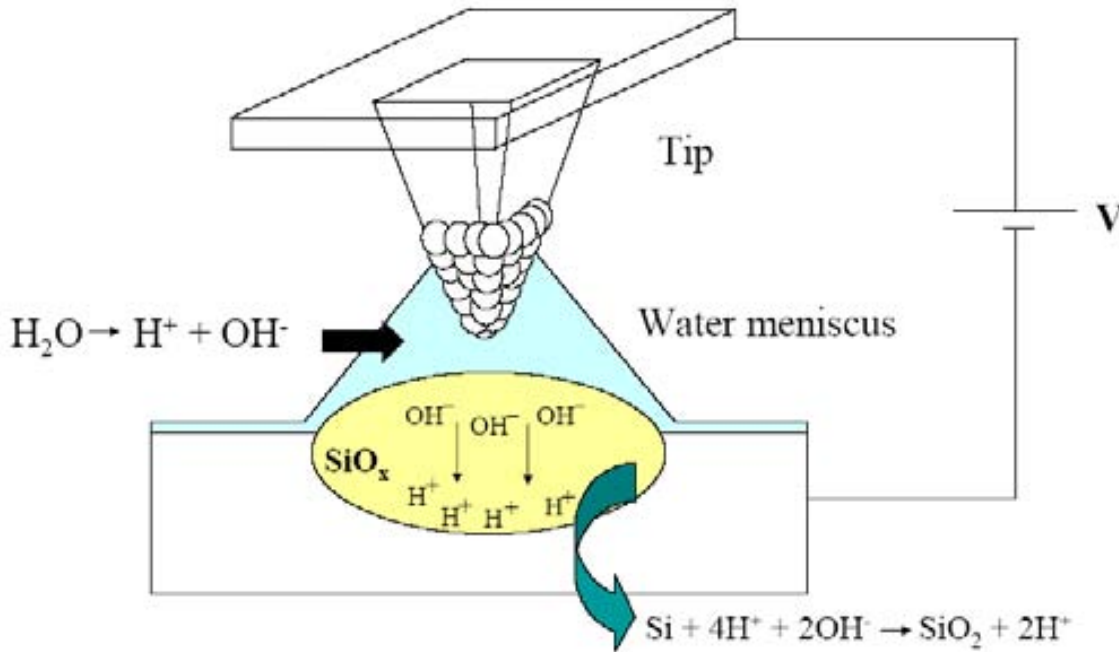
Probe anodic oxidation is one of the earliest and most extensively studied techniques in bias-assisted AFM nanolithography. Since Dagata et al. [18] demonstrated that a sharp conductive tip placed at nanometer-scale separation from the sample induces the anodization of its surface under the appropriate bias conditions, the continuous development of the technique has occasioned several examples of nano-devices fabrication: nanowires [19], MOS transistors [20], field-effect devices [21], nanomechanical devices [22] and SET devices [23].

In this method, the water meniscus formed in the tip–sample gap is dissociated by the negative tip bias, and the O^- and OH^- oxidative ions react with the substrate to form localized oxide nanostructures. Because the molecular volume of the oxides is usually larger than that of the substrate materials, raised nanopatterns are formed after the oxidation reaction. AFM-based anodic oxidation has been applied to produce oxide structures on semiconductors, metals and other materials. In addition, the anodic oxide features can act as reactive sites for the further assembly of molecules and nanoparticles through chemical linkages and affinities. Alternatively, the anodic oxides can also be etched to produce negative structures on the substrates for pattern transfer.

Figure 6.3 shows a conceptual drawing of AFM nano-oxidation mechanism. AFM nano-oxidation is performed in ambient atmosphere. The air humidity provides the adequate environment: when the tip and surface are placed in close proximity, a water meniscus is formed which provides the OH^- ions necessary for the oxidation reaction. Additionally, experiments performed

at different humidity [24] reveal that the extension of the water meniscus constrains the extension at which the oxidation reaction takes places.

Figure 6.3



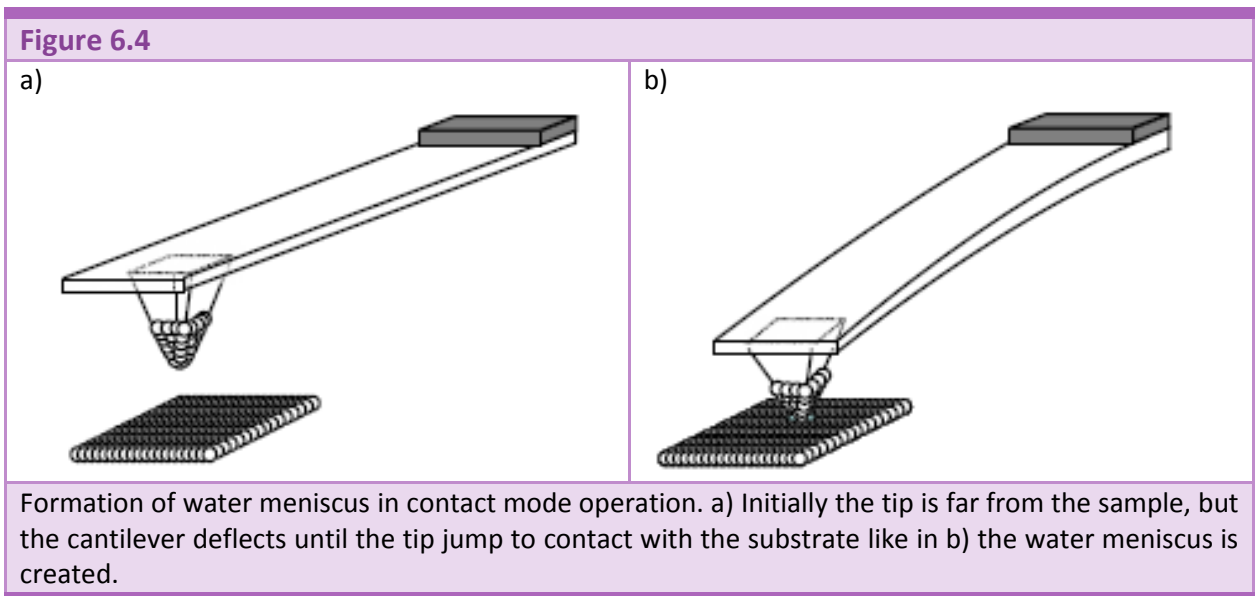
AFM nano-oxidation mechanism. When the tip is close enough from the surface a water meniscus is formed. This water meniscus provides OH^- ions for the oxidation.

One way to improve the aspect ratio of oxide features and control the structural and electrical properties of the AFM oxide is using voltage modulation. Variation of the voltage-pulse parameters confirms that the oxide dimensions can be controlled sensitively over a wide range of pulse parameters. Voltage modulation overcomes the self-limiting character of AFM oxidation by reducing the build-up of space charge within the oxide during growth. This enhancement can be used to increase the writing speed or lower the voltage, both beneficial for practical nanoelectronics fabrication [25].

Local oxidation can be performed in contact and dynamic modes. Contact mode can offer higher resolution but no reproducibility over large areas; because the tip is wearing continuously while performing lithography in contact mode, due to the combined effects of frictional and attractive electrostatic forces [26]. Using dynamic mode, as the tip and sample are separated by a gap of a few nanometers during the oxidation, the effective lifetime of the tip is much longer.

Contact mode

In contact mode the AFM tip is in direct contact with the surface (Figure 6.4). The water meniscus is formed at the same time that the tip touches the surface, due to the condensation of water vapor in the nanometer-size cavities of the tip-surface interface. Then, if a voltage is applied, the surface is locally oxidized because the meniscus allows the current flow [27]. The application of voltage while the tip is scanning the surface results in patterned lines or areas. Surfaces have to be very flat to allow keep the water meniscus during the scanning.



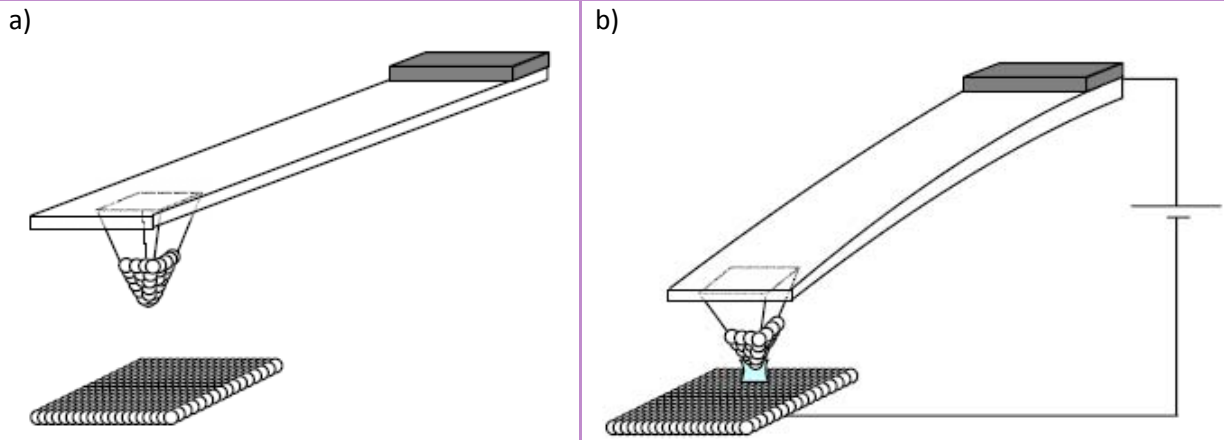
Non-contact mode

In dynamic mode or non contact mode, it is necessary to induce the creation of the water meniscus. It has been found that the water meniscus can be field-induced by applying a threshold voltage between the tip and sample (Figure 6.5) [1, 2, 28]. In silicon, the value of the threshold voltage is 12 V. Once the water meniscus is formed, oxidation can proceed at a lower voltage than the threshold voltage, but usually, higher voltages are required to apply in dynamic mode than in contact mode.

By optimizing the oxidation parameters (i.e., voltage, tip velocity and tip-sample distance) it is possible to control the feature dimensions down to less than 10 nm. This implies that, as the oxidation reaction is constrained by the water meniscus, the dimensions of the water meniscus will be of nanometer scale. In consequence, it is expected that the chemical-physical parameters of the meniscus (like electrical conductivity) will be influenced by its geometry.

In non contact mode, once the liquid bridge has been formed, its lateral dimensions can be decreased by increasing the average tip-sample distance. As smaller water meniscus can be obtained in non contact mode, higher resolution can be achieved.

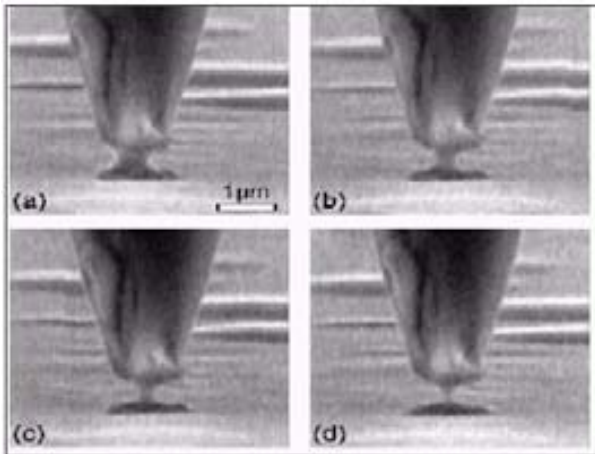
Figure 6.5



Formation of water meniscus in non-contact mode operation. (a) Even if we start far from the sample, the tip approaches to the surface due the application of a voltage, and the water meniscus is formed if the voltage value is high enough and if the tip and the substrate are close enough.

Confirmation of the formation of the water meniscus can be observed in Figure 6.6, where a real view of the water meniscus has been obtained by using an environmental SEM [29].

Figure 6.6

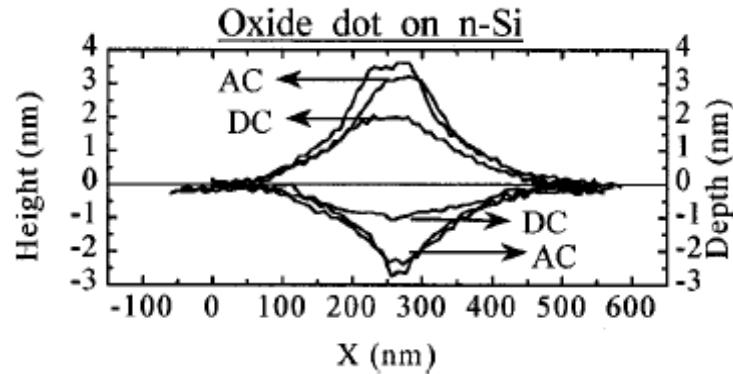


Environmental SEM images of the water meniscus [29].

The mechanism of probe oxidation has been addressed by several authors. The kinetics of the oxidation seems independent of the oxidation method. Generally, as have been commented, it

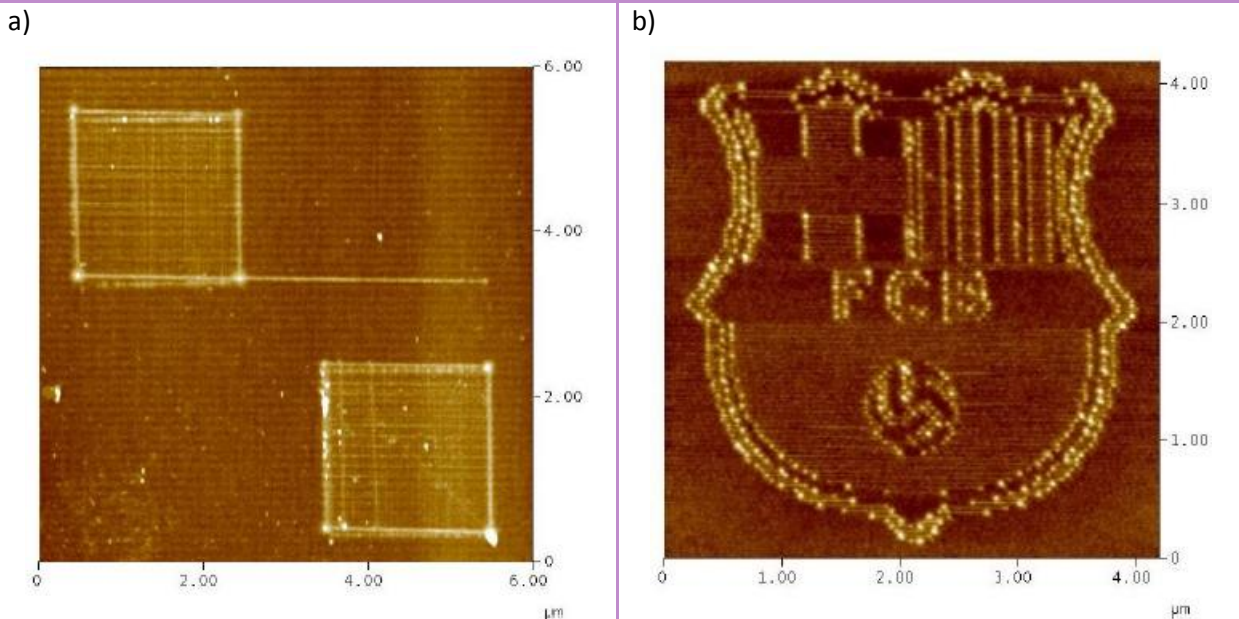
is suggested that the oxidation mechanism and kinetics are closely related to electrical field, surface stress, water meniscus formation, and OH^- diffusion [30, 31]. Specifically, various models including the Cabrera–Mott model, power-law model, direct-log kinetic model, and space charge model have been proposed to account for the oxidation behavior.

Figure 6.7



Oxide dot on Silicon. Enhancement of the aspect ratio and increase in the density by voltage modulation for n-type silicon as determined by SPM/etching. The increase of the height from 2 nm to 3.5 nm coincides with an increase in the consumption of silicon at the centre of the oxide feature [25].

Figure 6.8



Examples of oxidation at finite tip-sample distance. AFM topographic images after local oxidation lithography: a) shows a cantilever and an electrode. b) shows an arbitrary complex image transfer to demonstrate its high resolution and accuracy.

Studying the oxide growth it can be determined that the size of the water meniscus and the tip-sample separation for a fixed time do not imply differences in the vertical growth rate, but it has a strong dependence with the applied voltage. The lateral dimensions of the local oxide depend on several factors, such as the voltage and pulse duration, the relative humidity, the hydrophobicity and dielectric constant of the material to be oxidized, and the tip's size and geometry [32]. Furthermore, when an AFM oxidation is performed, in addition to the growth of the oxide, there is also, silicon consumption. Figure 6.7 displays silicon oxide dots in cross section. It is possible to measure the volume of consumed silicon with an oxide removal by HF etching. The greater silicon consumption and the higher oxide growth occur at the center of the oxide feature [25].

Finally some examples in Figure 6.8 demonstrate the versatility of this technique. In both areas the pattern was performed in non contact mode, using a silicon surface and applying a voltage between 12-28 V while the lines are scanned. The feedback control is deactivated during the time that the voltage is applied.

6.1.2.2 Electrochemical deposition

The AFM based electrochemical deposition involves the direct tip bias application to initiate local electrochemical reactions. The electrochemical deposition technique is an electrochemical version of DPN utilizing meniscus formation and tip bias application during ink deposition. The electrochemical DPN (EDPN) combines the versatility of electrochemistry with the simplicity and power of the DPN method.

6.1.2.3 Electrochemical modification

The ability to directly pattern and write polymers at the nanometer scale is crucial to applications in data storage and molecular electronics. The AFM electrostatic nanolithography (AFMEN) can generate nanoscale polymeric features by Joule heating and mass transport on initially featureless polymer films [33-35]. In this technique, current flow generated by tip biasing produces effective Joule heating which locally softens the polymer film. The extremely non-uniform electric field gradient polarizes the viscoelastic polymer and attracts it towards the tip apex, leading to the formation of protruding structures on the film. When the electrostatic force overcomes the combination of Laplace and viscous pressures, electrostatic deformation of the polymer melt takes place. The optimal polymer film for patterning relies on the materials selection and processing that provides gradual dielectric breakdown under the electric field. Feature size is critically dependent on the thermal characteristics of the polymer.

6.1.3 Force-distance curves

In chapters 2 and 3, force-distance curves have already been introduced as relevant information to elucidate the cantilever behavior. A force-distance curve is, basically, the representation of the changes in the photodiode voltage (for optical detection systems), which means a change of the deflection of the AFM probe cantilever, as a function of the vertical displacement of the piezo actuator. Force-distance is a result of two contributions: the tip-sample interaction and the elastic force of the cantilever.

When acquiring force-distance curves, the piezo must be ramped along the Z axis, i.e. the axis perpendicular to the surface. There are two principal modes of acquisition: contact and dynamic. In contact mode the sample is displaced along the Z axis in discrete steps and the variations in cantilever deflection are collected. In dynamic mode, the cantilever is vibrating while the sample is approached and withdrawn. In this mode both cantilever deflection and amplitude of cantilever oscillations can be collected as a function of tip-sample distance. To sum up, in contact mode force-distance curves can be obtained and in dynamic mode, in addition to the force-distance curve, is it also possible to obtain amplitude-distance curves.

From a distance-force curve we can extract information of the tip-sample interaction forces as a function of the tip-sample distance. Tip-sample force is given by Hooke's law:

$$F = -k \cdot \delta_c \quad (6.1)$$

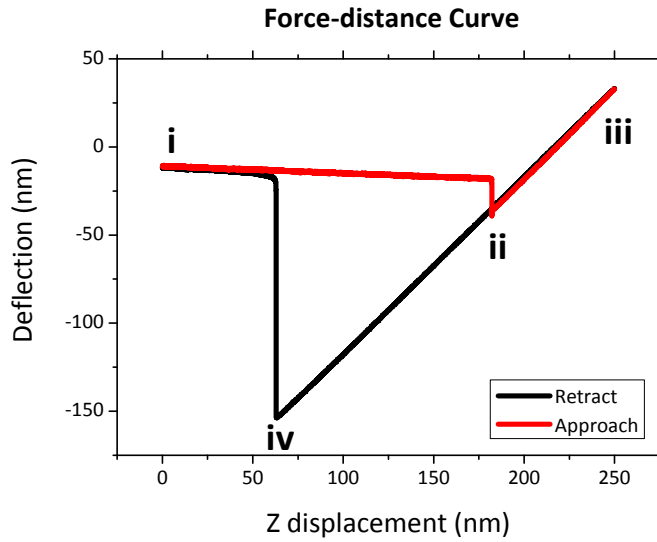
where k is the spring constant of the cantilever and δ_c the cantilever deflection. The parameter Z , i.e. the extension of the piezoelectric, can be directly related to the deflection of the cantilever, when this is in actual contact with the substrate. Being D the distance between the sample and the tip when the piezo is at rest position, it is possible to write (6.2), where δ_s is the sample deformation.

$$D = Z - (\delta_c - \delta_s) \quad (6.2)$$

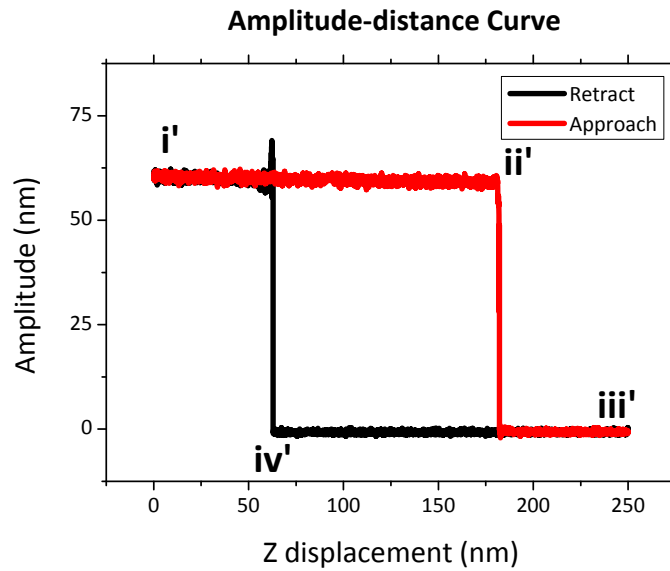
Distance curves, then, can provide information not only about the deflection of the cantilever but also about the amplitude of oscillation, as it can be seen in Figure 6.9.

Figure 6.9

a)



b)



Simultaneous acquisition of distance curves in dynamic mode operation. a) Force-distance curve where the *i* part represents the approach of the cantilever beginning when it is far from the sample. *ii* point corresponds to jump-to-contact and the tip remains in contact with the substrate until the *iv'* point in the retracting part of the curve, that is called jump-off-contact. B) Amplitude-distance curve simultaneously acquired shows that during the approach (*i'* part) the cantilever is oscillating and in the point *ii'* (jump-to-contact) it experiences a sudden change. When the tip enters in contact with the surface it stops to oscillate (part *iii'*) and until it jumps-off-contact (point *iv'*) it cannot oscillate again.

Force-distance curves have two main characteristics: the discontinuities at *ii* and *iv* points (see Figure 6.9a) and the hysteresis between approach and retract curve. The two discontinuities in force values are called “jump-to-contact” (*ii* point) in the approach curve and “jump-off-contact” (*iv* point) in the retract curve. The difference in path between approach and retract curves is usually called “force-displacement curves hysteresis” (zone compressed between *iv* and *ii* points in both curves). Force-distance curves show three equilibrium positions, the *i* part and the *iii* part are stable positions; while the part called “force-displacement curves hysteresis” is unstable.

The *i* part is obtained when the tip is far from the substrate and the deflection is nearly zero. During the approach phase, first, the tip is far from the surface and it advances. When the force gradient is larger than the effective elastic constant, the cantilever becomes unstable and the tip “jumps” to contact in the point *ii*, this discontinuity depends only on the attractive part of the interaction. Then the tip remains in contact with the substrate. The *iii* part represents the contact between tip and substrate. Even when the retract part begins and tip and substrate are still in contact. In point *iv* the tip “jumps” off the contact, leaving the tip far from the substrate again.

The most interesting regions of the force-displacement curves hysteresis are the two non-contact regions, containing the jump-to-contact and the jump-off-contact points. The non-contact region in the approach curve gives information about attractive or repulsive forces before contact. In particular, the maximum value of the attractive force is sampled prior to jump-to-contact. The non-contact region in the retraction curve contains the jump-off-contact where the pull off force equals the adhesion force. To evaluate the adhesion force it is necessary to determine the deformations and the contact area of the sample, and both characteristics are very difficult to obtain.

Amplitude-distance curves are characterized by a mostly horizontal line at the free amplitude (when the cantilever is near the sample surface, surface forces can modify the cantilever vibration); a contact line at zero amplitude after the contact has happened (when the cantilever is in contact with the surface the free end of the cantilever is no longer vibrating); and a step transition between both regions when the tip is contacting the substrate (Figure 6.9.b). During the approaching, the cantilever is oscillating (part *i'*) until the jump-to-contact point (*ii'*), when the tip collapses with the surface. During the contact part *iii'* the cantilever behaves like in contact mode and stops to vibrate giving a zero signal. Finally, during the retract part and at the same distance that the tip jumps-off-contact of the sample (*iv'* point), the cantilever can oscillate again at the same amplitude that was initially.

In amplitude-distance curves, the cantilever may be modeled as a harmonic oscillator with effective mass m^* and spring constant k [36]. When the tip is far away from the surface, the equation of motion of the cantilever is given by (6.3).

$$m^* \frac{d^2 \delta_c(t)}{dt^2} + \gamma \frac{d\delta_c(t)}{dt} + k\delta_c(t) = F_0 e^{i\omega t} \quad (6.3)$$

where γ is the damping coefficient and $F_0 e^{i\omega t}$ is the exciting force exerted by the driving system on the cantilever. Solving this equation, the free amplitude vibration as a function of frequency is obtained:

$$A(\omega) = \delta_c(t) e^{-i(\omega t + \varphi)} = \frac{F_0}{\gamma \omega_0} \frac{\omega_0 / \omega}{\sqrt{1 + Q_0^2 \left[\left(\frac{\omega}{\omega_0} \right) - \left(\frac{\omega_0}{\omega} \right) \right]^2}} \quad (6.4)$$

where $\omega_0 = \sqrt{\frac{k}{m^*}}$ is the resonance frequency and $Q_0 = \frac{m^* \omega_0}{\gamma}$ is the quality factor.

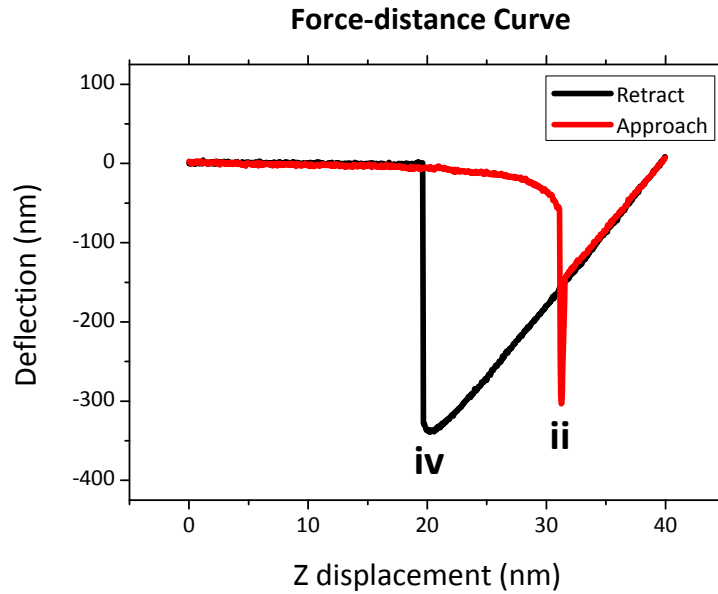
When force-distance curves are acquired in air, meniscus forces exerted by thin layers of water vapor dominate the interaction. Water meniscus force exceeds all other forces, and in particular, it masks the Van der Waals force. Once the meniscus forms and the capillary force onsets, the amplitude of the oscillations abruptly goes from the amplitude to zero via a sharp and strongly discontinuity. Amplitude force-curves are more suitable for the detection of the distance of formation of menisci. Of course this does not occurs when operating in liquid environment.

In addition to the information already exposed about the deflection and amplitude of the cantilever (both providing information about the tip-sample interaction forces) while the probe is approaching to and retracting from the substrate, it is possible to measure other magnitudes that can also be of interest for some applications. For example, characterization of electromechanical sensors can be done [37] by acquiring an external voltage simultaneously to the deformation of the sensor, that would be given by the parameter δ_s is detected.

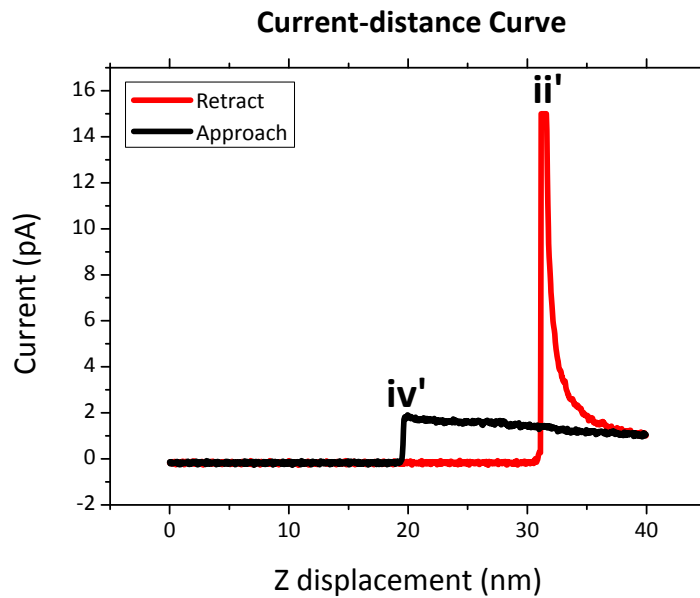
Another possibility is to acquire simultaneously the current flowing through the tip, which can provide information about the oxidation mechanism/dynamics [30]. These data can result crucial for the best understanding of the bias-assisted lithography techniques and also can be used to control and optimized the parameters involved there.

Figure 6.10

a)



b)



Simultaneous acquisition of distance curves under application of 9 V (sample positive) on a p-type silicon (100) sample. a) Force-distance curve and b) current-distance curve representing the current flow through the tip. An increase of the current in point *iv'* is attributed to an increase of the meniscus conductivity when it is enlarged and stretched.

In Figure 6.10 a force-distance curve is represented (Figure 6.10.a) and simultaneously the current through the tip is acquired (Figure 6.10.b). These curves were acquired while applying 9 V to a silicon substrate in ambient conditions. The first sharp increase of current (point *ii'*) in the approach curve appears due to the formation of water meniscus and the onset of electronic and electrolytic processes. As the oxidation reaction is being induced on the silicon substrate, a silicon oxide is growing in the silicon surface, for that reason, the time evolution of the current when tip and surface are in mechanical contact decrease because the oxide isolating properties. A dependence of the current on the tip-surface separation is shown in the retraction part of the force-distance curve (point *iv*) a second increase in current is observed when tip separates from the surface. This second increase in current is thought to be a result of the change of the water meniscus properties, consistent with a reduction of space charge of the tip-surface junction. The increase of the conductivity of the meniscus allows increasing the tip-sample distance without decreasing the oxidation rate. This behavior explains the experimental observation described in Section 6.1.2.1 that, under certain polarization conditions, the oxidation growth rate is higher in non contact mode AFM anodic oxidation as compared to contact mode AFM anodic oxidation.

In [30, 38-41] is provided a comprehensive analysis and study of the electrical current passing through the tip-substrate junction during the oxidation lithography. In this analysis it is revealed that the voltage pulse can produce a transient electronic current, water breakdown and a maximum charge/defect density. Excess charge is channeled into lateral diffusion, keeping the charge density within the reaction zone constant and reducing the aspect ratio of the resulting oxide features. A uniform charge density implies that the oxides contain a fixed defect concentration, in accordance with the space-charge model. It was shown that most of the electrical current involved in high voltage oxidation of Si did not actually induce surface oxide growth, and that lateral diffusion and small aspect ratios are unavoidable aspects under contact-mode conditions.

6.1.4 Experimental conditions

All the experiments showed in this Chapter were performed using a *Dimension 3100* AFM microscope system with a *NanoScope IV* controller. The system is equipped with the *Nanomanipulation* and *Nanolithography* software that provides a very flexible and accurate control of the in-plane position and movement of the AFM probe [42]. In addition, a commercially available electronic module has been used for the acquisition of the current called *TUNA* (Tunnelling current detection) which can map the electrical currents with high sensitivities (< 1 pA) and can be operated either in contact mode or dynamic mode. The AFM

system is operated in a class 100 clean room environment, with a controlled temperature. The relative humidity is not controlled but it is monitored, giving a value around 50 ± 5 %. The probes that have been used were silicon AFM probes without coating (nominal values of 40 N/m for the spring constant and 250 kHz for the resonant frequency).

Atomic force microscopy and lithography are performed, operating the AFM in the dynamic mode. Operation in the contact mode results in damage of the polymer surface by scratching. The process used to perform the lithography in the dynamic mode has been described in [1, 2]. First, the cantilever free oscillation is set to a low amplitude value (<10 nm). This ensures a small average distance between the tip and surface. Before defining a pattern, the AFM control feedback is disabled, and a voltage is applied. When defining a line, first the inclination of the surface with respect to the X–Y piezoscanning plane is captured and subtracted in order to keep a constant separation distance between the tip and surface. It is found that this is not enough when a drift in the Z direction exists, resulting in a non-uniform patterned line because of the change in the separation.

6.2 LOCAL MODIFICATION OF THIN PMMA LAYERS

In this section, we present a new method to perform AFM nanolithography. The method is similar to the previously explained AFM anodic oxidation, but it is applied to modify thin layers of PMMA deposited on silicon substrates. The interest of this approach (besides its fundamental interest to understand the modification mechanism) is that it can be directly combined with electron beam lithography.

The method consists of inducing the local modification of the PMMA by applying a positive voltage between the silicon and an atomic force microscope (AFM) tip. Recently, the electrostatic nanoscale modification of thin layers of polymers by AFM has been reported [33, 35, 43]. For that case, the mechanism has been attributed to the electrical breakdown of the polymer: the flowing of electrical current, which causes the local heating of the polymer. This method, AFMEN, was described in Section 6.1.2.3. For the present experiments, the current that is detected indicates that heating is not a plausible mechanism.

The local modification of the PMMA layers takes place at voltages larger than 28 V, when it is observed that a hole is directly produced on the PMMA. For lower voltages, the resulting modification consists of raised areas. It is interesting to note that the silicon surface is simultaneously oxidized even in the case where a hole has not been created in the PMMA after the AFM lithography.

In addition, the patterns created in the polymers can be used to form metallic nanostructures by performing metal deposition and lift-off processes after the polymer modification, which will ensure the applicability of the technique in the area of nanofabrication.

6.2.1 Additional/Specific experimental details

For sample preparation, 950k molecular weight PMMA (2% dissolved in anisole) is deposited on a silicon (100) surface (p-type, resistivity = 4 Ω cm). Before deposition, the surface is cleaned by dipping the sample for 10 seconds in acetone and 10 seconds in isopropanol (IPA). Then it is rinsed in water and dried with N₂. In order to obtain thin layers (<30 nm thickness) of PMMA, the concentration of PMMA solution is reduced by adding more anisole, to a final concentration of approximately 1%. The PMMA is deposited in a conventional spinner at 4000 rpm for 30 s. Finally, the sample is baked in an oven at 180 °C for 30 minutes. The surface roughness after the PMMA deposition is lower than 0.5 nm rms. The final thickness of the PMMA is measured with

AFM after performing an electron-beam lithography process. Electron beam lithography is performed in an FE-SEM at 10 keV. Selected areas on the surface ($1\ \mu\text{m} \times 1\ \mu\text{m}$) are exposed to an electron dose of $30\ \mu\text{C}/\text{cm}^2$. After the exposure, the development is performed by dipping the sample for 30 seconds in MIBK:IPA, 1:3 (methyl isobutyl ketone and isopropanol), rinsing for 30 seconds in IPA and drying with N_2 .

6.2.2 Results

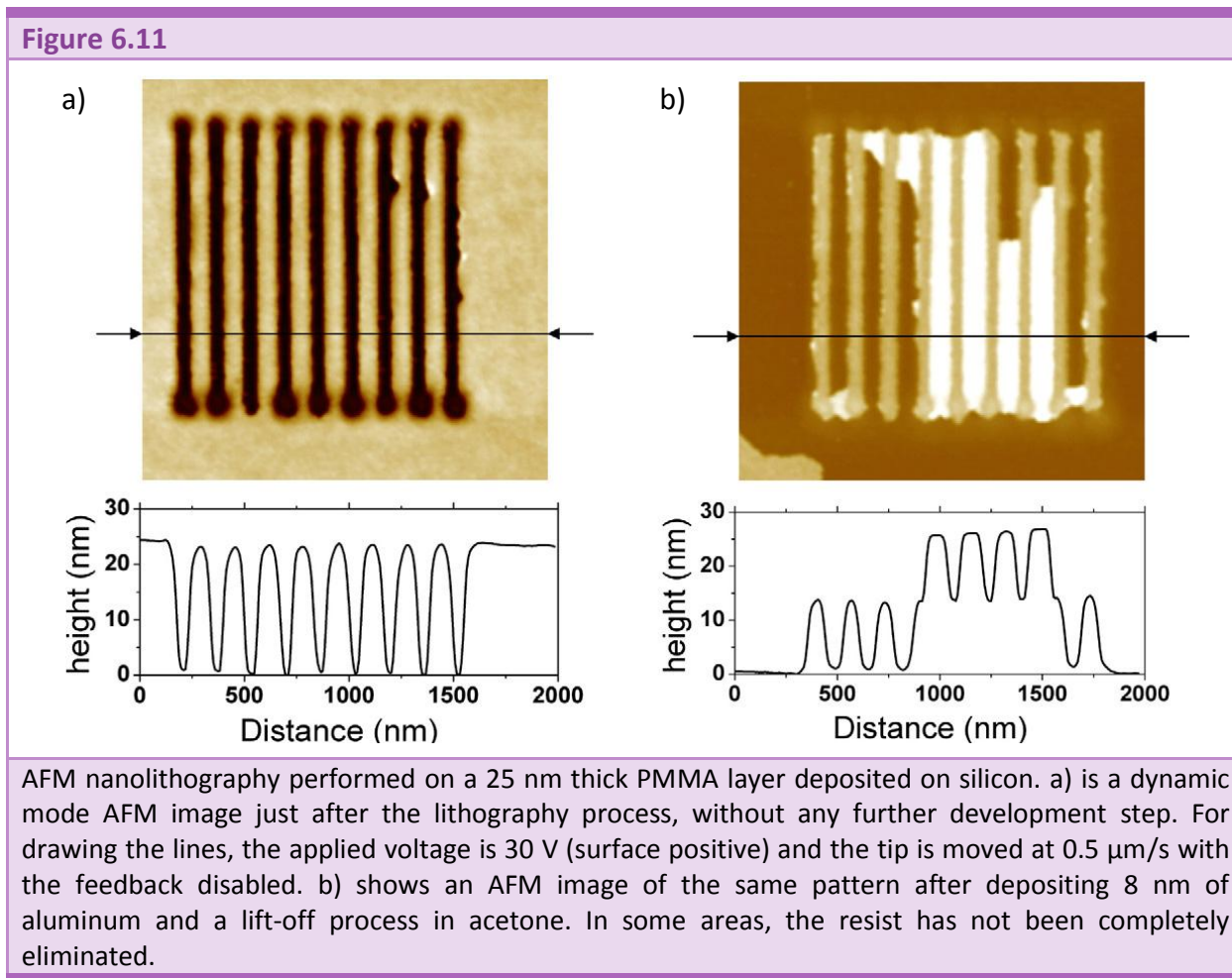


Figure 6.11.a. shows a set of lines obtained in a 25 nm thick PMMA layer deposited on a silicon surface. The tip was moved at a speed of $0.5\ \mu\text{m}/\text{s}$ while applying a voltage of 30 V (tip positive). The profile at the bottom shows that the depth of the lines is 25 nm, which implies that the full thickness of the PMMA has been removed. It is interesting to note that the PMMA in the patterned lines has been eliminated, i.e., a mound corresponding to the removed material does

not appear. Figure 6.11.b. shows an AFM image of the same pattern after the deposition of 8 nm of aluminum by RF sputtering and a lift-off process. After the deposition of the aluminum, the PMMA is removed in acetone. Some of the PMMA has not been completely eliminated in certain areas. As can be observed from the profile at the bottom of part (b), the apparent thickness of the aluminum lines is 12 nm, greater than the thickness of the deposited aluminum.

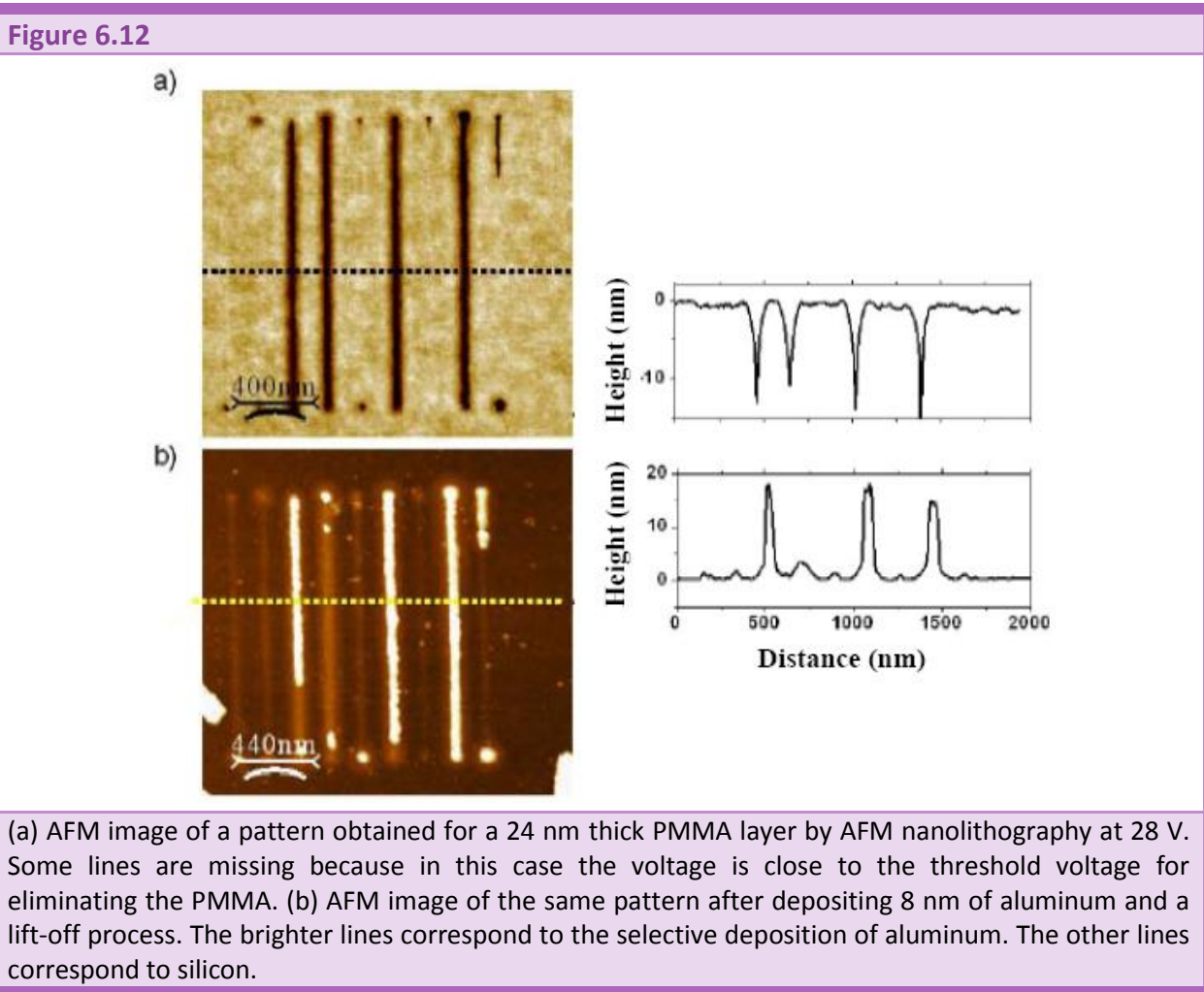
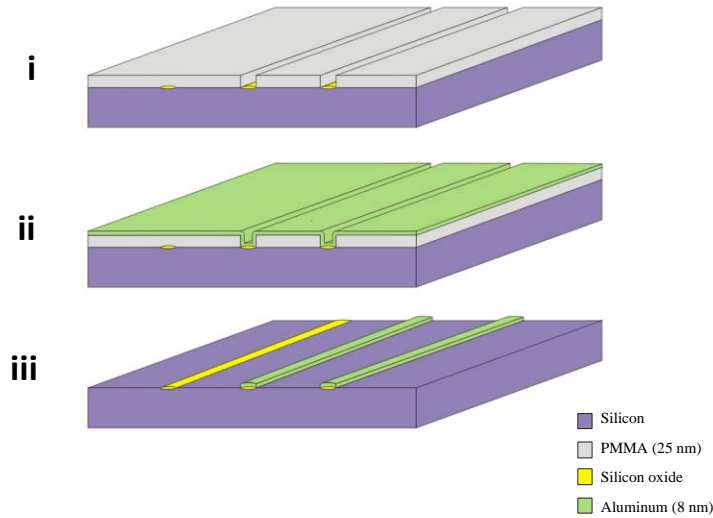


Figure 6.12.a. shows another pattern defined on a 24 nm thick PMMA layer. In this case, the applied voltage was deliberately selected to be close to the threshold voltage required to induce a hole on the PMMA (28 V), so that some lines were not completely patterned. The depth of the lines as shown in the profile appears smaller than the thickness of the PMMA layer due to the effect of convolution with the AFM tip. Figure 6.12.b. shows the same pattern after the aluminum deposition and lift-off processes (same conditions as in Figure 6.11). The image reveals that the aluminum is only partially deposited on some areas but in all the patterned areas a protruded line appears. These lines correspond to the AFM oxidized surface. It is

interesting to note that the silicon surface is oxidized even in the case where trenches are not created in the PMMA after the AFM lithography.

Figure 6.13



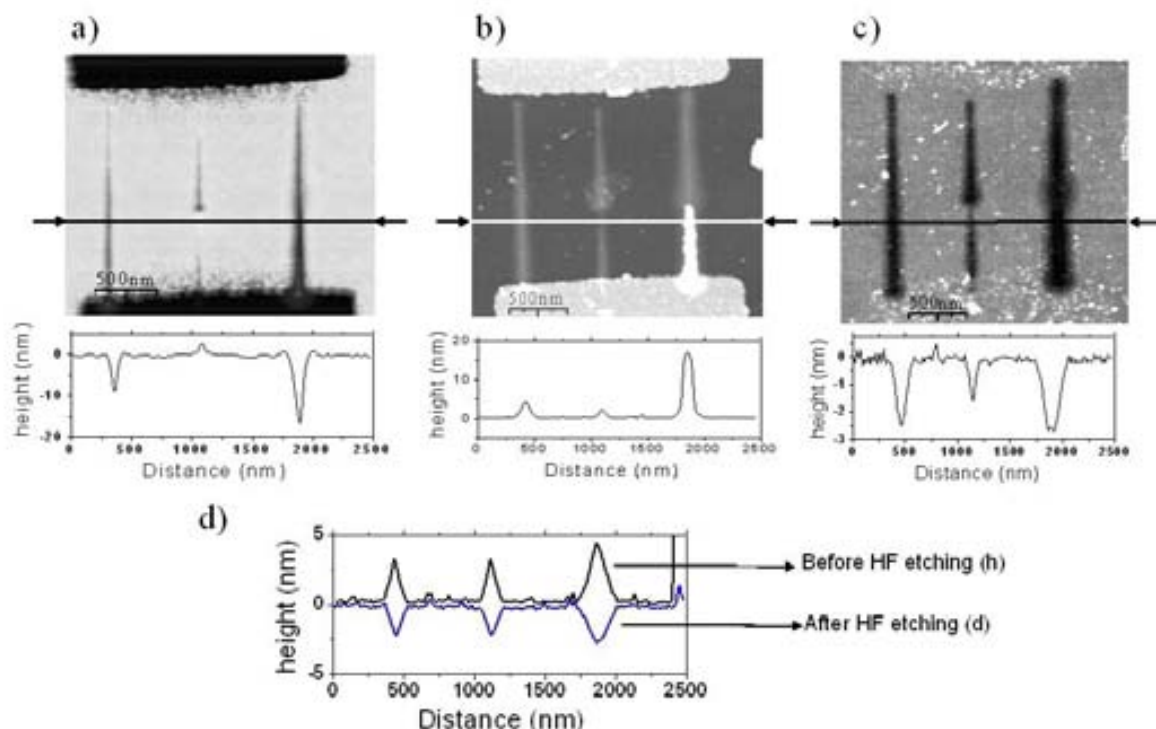
Drawings to illustrate the two phenomena observed in Figure 6.12. (i) Patterning with the AFM. (ii) An aluminum layer is deposited by RF sputtering to make the lift off process. (iii) The apparent thickness of the aluminum lines is greater than the thickness of the deposited aluminum, this is explained due to the silicon surface is oxidized even in the case where trenches are not created in the PMMA after the AFM lithography.

Evidence that the lines in Figure 6.12 correspond to oxidized areas comes from the experiment shown in Figure 6.14. In this case, after the AFM lithography (Figure 6.14.a), metal deposition and lift-off processes (Figure 6.14.b), the sample is immersed in a HF 2 % solution for 10 seconds to remove the silicon oxide. The resulting AFM image (Figure 6.14.c) reveals the lines as depressed areas, indicating that silicon has been consumed. Figure 6.14.d shows the profiles before and after the HF etching for evaluating the proportion of silicon and oxygen in the resulting oxide. The relation between h (height of the oxide line above the native silicon oxide) and d (depth of the line after the HF etching) is found to be $h/d = 1.4 \pm 0.2$, which is within the range usually found in AFM local oxidation [44].

In order to do the experiment described in Figure 6.14, AFM lithography has been combined with electron-beam lithography to facilitate the localization of the patterns with the AFM after the etching experiments. Electron-beam lithography allows to pattern larger areas than AFM lithography and, in consequence, it is convenient to combine the two techniques to overcome the limitation in speed of AFM lithography. Another advantage of the combination of AFM and electron-beam lithography compared to the use of electron-beam lithography alone is the

absence of the proximity effect, which will facilitate for example the fabrication of arrays of lines with small pitch. As a demonstration of the potential for combining AFM and electron-beam lithography, we have used both processes to fabricate a nanometre scale gap between two metal electrodes (Figure 6.15).

Figure 6.14



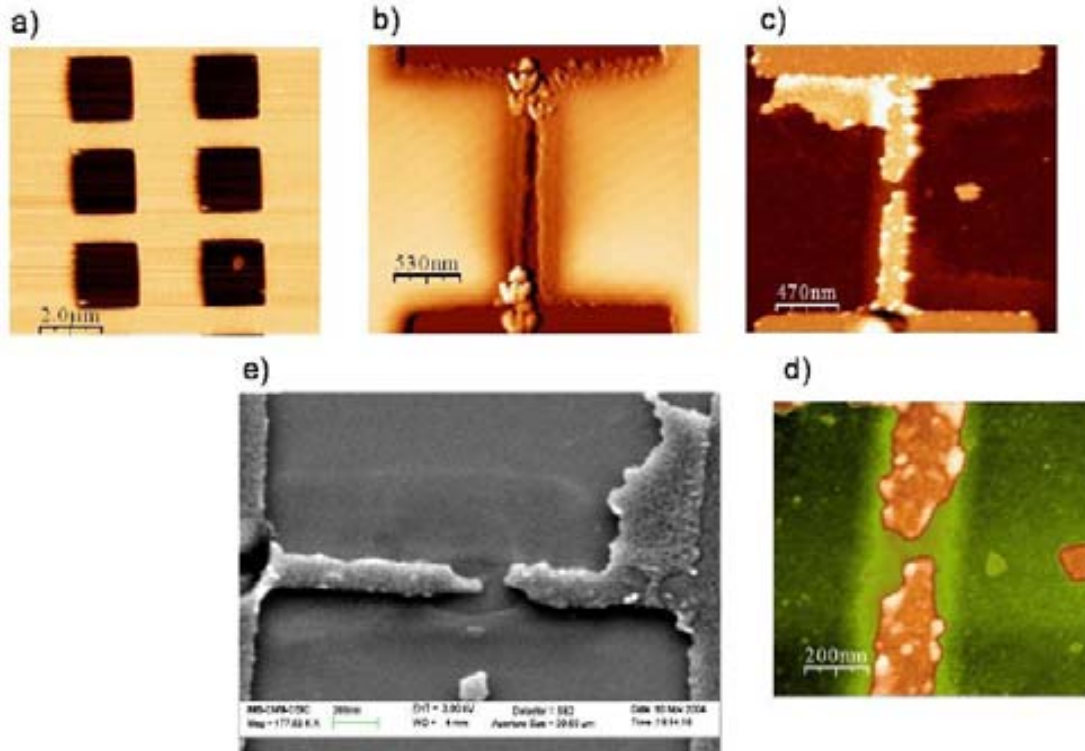
a) Examples of lines created by AFM nanolithography on a 25 nm thick PMMA at 30 V. The lines are not uniform because the separation between the tip and surface did not remain constant. The larger areas are patterned by electron-beam exposure and development. b) AFM image of the same area after depositing 8 nm of aluminum and lift-off. Aluminum is visible on the e-beam patterned areas and partially in one of the lines defined by AFM nanolithography. c) AFM image of the same area after etching the silicon oxide by dipping the sample in 2% HF. The holes show the consumption of silicon, indicating that the AFM nanolithography process induces the oxidation of the silicon. d) Profiles extracted from b) and c) to show the relation between oxide height (h) and silicon consumption (d) before and after the HF etching respectively. The relation h/d is found to be 1.4 ± 0.2 .

First, micrometre size squares are patterned on the PMMA by electron-beam lithography exposure and development in MIBK:IPA. The resulting pattern is shown in Figure 6.15.a As shown in the profile, the thickness of the PMMA layer is 26 nm. Next, the AFM lithography process is performed (Figure 6.15.b) to draw two lines from two of the squares while leaving a non-patterned area in the middle. The line becomes narrower in the middle, which is enough to avoid the formation of a continuous line during the lift-off process. The mounds at the ends of

the lines correspond to tip-induced contamination due to the high voltage applied. Later, an 8 nm thick layer of aluminum is deposited and the PMMA is eliminated by a dip in acetone. The resulting pattern is shown in Figure 6.15.c. Figure 6.15.d is an AFM zoom to show that the gap between the two electrodes is around 70 nm. Figure 6.15.e is a 30° tilted SEM image of the area of the gap. It shows that the raised area beside the top electrode in Figure 6.15.c corresponds to PMMA that has not been eliminated.

In the experiments, we have found that at present, the most important limiting factor for improving the resolution of the patterned features is the lift-off process. The minimum dimensions of the metal patterns can be decreased by optimizing the lift-off process and using electron-beam evaporated metal instead of RF sputtering.

Figure 6.15



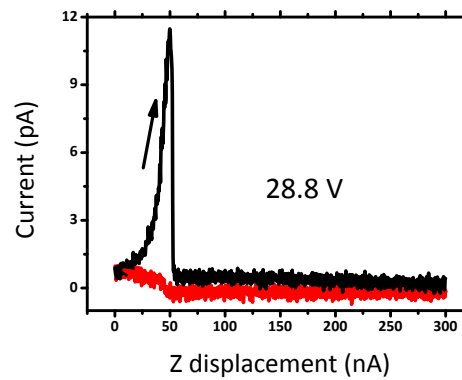
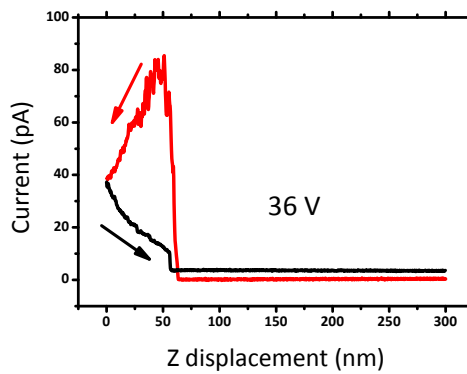
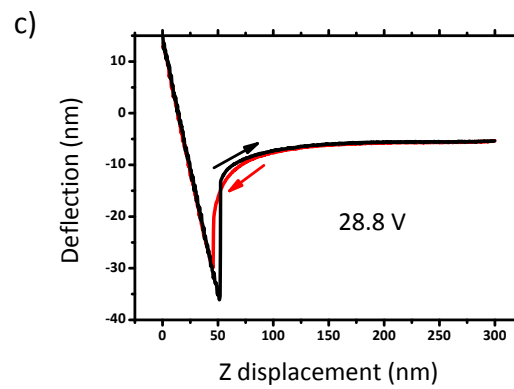
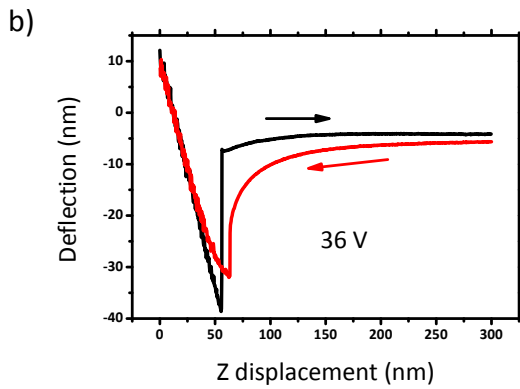
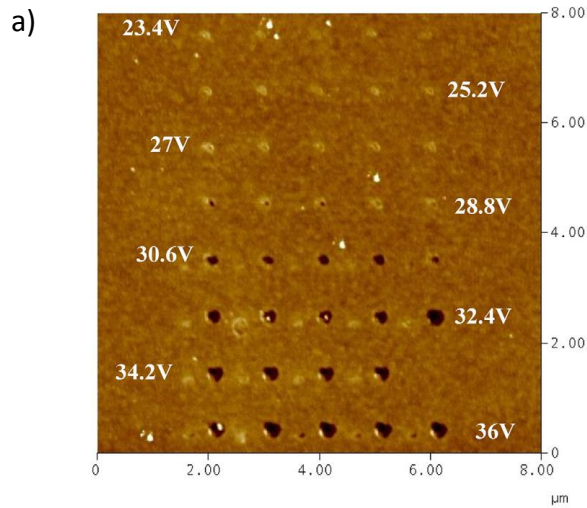
Example of combination of AFM nanolithography with e-beam lithography. a) $2 \times 2 \mu\text{m}^2$ squares are defined by e-beam lithography and development. b) After this, two lines are drawn by AFM lithography leaving a small gap between them. c) AFM image after depositing 8 nm of aluminum and a lift-off process. Remaining resist is observed in some areas. The thickness of aluminum appears higher in the AFM defined lines because of the selective oxidation of silicon. d) AFM image of a zoom in the area of c) to allow better appreciation of the gap. e) SEM image of the same pattern.

6.2.3 Discussion

In order to gain more information about the mechanism of AFM lithography on PMMA, we have monitored the flow of electrical current during the lithography experiments. We have used the technique previously presented in [30] and summarized in section 6.1.3. It consists of detecting the electrical current through the tip while obtaining a force versus distance curve. The voltage is applied before starting the approaching of the tip towards the surface, so that the presence of a displacement current is avoided and the electrical (ionic and electronic) current can be analyzed with short time resolution. Figure 6.16.a shows an AFM image of PMMA after obtaining a set of force versus distance curves at different voltages. For a voltage larger than 28 V, a hole is produced after the realization of a curve, while at lower voltage, a slightly raised area can be seen, which appears due to the combined effects of accumulated charge in the PMMA and the topographic effect of the grown silicon oxide underneath. Holes and mounds in each row are obtained at the voltage indicated in the picture. In this figure, one can observe a sharp voltage threshold for producing a hole. It is important to note that when a hole is created is always observed that it goes through the full thickness of the PMMA layer. Figure 6.16.b and Figure 6.16.c show two force/distance and current/distance curves at 36 V and at 28.8 V. At 36 V, it can be observed from the force versus distance curve that the formation of the hole begins right after the jump to contact (slope of the curve smaller than 1). The corresponding current versus distance curve reveals a sharp increase of current right after the jump to contact which decreases afterwards. In contrast, at 28.8 V the formation of the hole cannot be observed in the force versus distance curve (slope is equal to unity all the time that the tip and surface are in contact). In this case, the current versus distance curve reveals that the current is increasing all the time that the tip and surface are in contact.

Current evolution as a function of time is plotted in Figure 6.17 for different voltages. Data are extracted from the current measurements while obtaining force versus distance curves, as in Figure 6.17.b shows the current evolution for the lowest range of voltages, which cannot be seen with the Y scale of Figure 6.17.a. Initial time ($t = 0$ ms) refers to the jump to contact. The increase of current is more pronounced after some time of the tip and surface being in contact. The current jump to zero corresponds to the moment at which the tip and surface separate. It happens at different times because of the different excursions of the tip while obtaining the approach/retraction curves. Figure 6.17 reveals that the increase of the electrical current depends on the applied voltage: at high voltage, the current increases very fast at the beginning, while at lower voltages there is a fast increase of current which is delayed with respect to higher voltages.

Figure 6.16

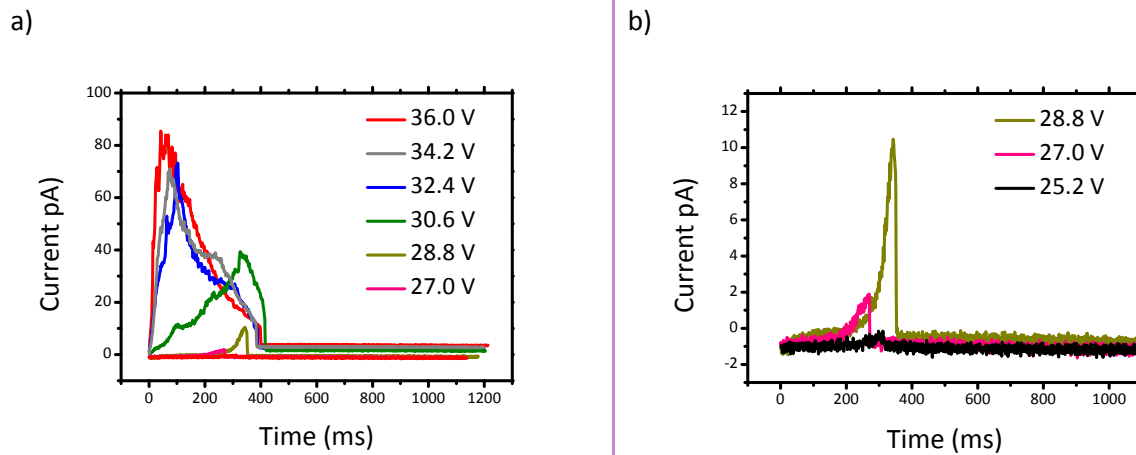


a) AFM image of an $8\ \mu\text{m} \times 8\ \mu\text{m}$ area of a 26 nm thick PMMA layer deposited on silicon. Each dot is produced by obtaining a force/distance curve with the AFM while applying the voltage indicated in the figure for each row. During the production of the force versus distance curves, the electrical current through the tip is simultaneously detected, as shown by the bottom curves of the figure. The two sets of curves correspond to modifications obtained at 36 in b) and 28.8 V in c). The arrows indicate the approach (right to left) and retraction (left to right) parts of the curves. The value of the constant force of the cantilever is around 25 N/m.

From the present data, it is difficult to completely elucidate the mechanism responsible for the elimination of PMMA during the AFM lithography process. The current level is relatively low (less than 10 pA at 29 V) for attributing the elimination of the PMMA to a thermal effect induced by the breakdown of the PMMA, as in the conditions of [43]. Under the present experimental conditions, the existence of surface oxidation even when a hole is not produced on the PMMA indicates the presence of ionic transport (OH^- ions) through the PMMA. The high ion concentration during the voltage pulse induces an electrochemical reaction of the PMMA, involving the elimination or evaporation of the reaction products. An important observation here is that, similar to what it is found in AFM local oxidation of silicon, the extension of the electrochemical reaction is confined to below the tip, probably by the extension of the water meniscus. It is known that the diameter of the oxide features on silicon surfaces in AFM nano-oxidation depends on the shape of the water meniscus [28] and that the current flowing during AFM nano-oxidation of silicon depends on the extension of the water meniscus [40]. We observe a similar effect in Figure 6.12, where the non-uniformity of the line width observed is due to the change in the separation between the tip and surface. Then, as is already known from AFM local oxidation experiments [28], the resolution of the patterns can be improved by the manipulation of the water meniscus (i.e., increasing the tip-sample distance and reducing the ambient humidity).

The evolution of current during the application of the pulse (Figure 6.17) also corroborates this framework: at the highest voltages (between 36 and 30 V), one finds an increase of current until a maximum current is reached, and after this the current decreases. We interpret the existence of a maximum in the current to the fact that almost all the PMMA below the area covered by the water meniscus has already been eliminated: as the reaction is confined by the water meniscus, the electrochemical reaction ceases and, in consequence, the electrical (ionic) current decreases. The curves in Figure 6.17 also indicate that the rate of the reaction increases with the voltage: as the voltage becomes higher, the ionic concentration becomes equally higher, increasing the electrochemical reaction. In this case, it takes less than 10 ms to write a dot, which, assuming a dot diameter of 200 nm, implies a writing speed of approximately 20 $\mu\text{m/s}$. This also explains the current evolution at lower voltages (from 28 to 25 V): a minimum concentration of OH^- ions is necessary to trigger the onset of the electrochemical reaction, which delays the start of the reaction and so the elimination or evaporation of PMMA.

Figure 6.17



Current as a function of time extracted from the experiment shown in Figure 6.15. It shows that the onset of the current is delayed when the voltage is lowered. Time = 0 ms corresponds to the jump to contact instant. The time at which the current jumps to zero depends on the excursion of the corresponding force/distance curve.

The current increases slowly (silicon oxidation) until a certain point, when it starts to increase fast (PMMA removal). This fast increase of current makes it very difficult to stop the reaction just when the PMMA is partially removed. At higher voltages (Figure 6.17.a) the PMMA removal starts just at the beginning of the application of the voltage pulse. In addition, also from Figure 6.17, we obtain a low current level (in the pA range) which makes it difficult to attribute the removal to a thermal effect. In addition, it has been found that the polarization of the voltage is relevant for the elimination of the PMMA: we have only succeeded in fabricating holes at positive sample voltage.

6.3 LOCAL MODIFICATION OF THIN EPOXY BASED RESIST LAYERS (NON EXPOSED)

In this section, it is repeated the method presented in the previous section using a negative epoxy based resist. Thin layers of epoxy based resist were obtained by dissolving a special very low viscosity resist developed for EBL (mr-EBL 6000.1 XP, also used to fabricate the hydrophobic barriers in chapter 5) [45]. The interest of this approach is clarifying the local modification mechanism by studying the behavior of another polymer to compare with PMMA results.

Negative epoxy based resist processing have to be performed with more care because white light expose it, as there is a contribution of the entire spectrum wavelengths. The employment of equipments that are not used to work with photosensitive resist is delicate because they have sources of white light without filters (for example, from optical microscopes, cameras, windows or lamps). In consequence, one ease and simple solution consists of turning off all the lights and working in darkness, complicating the positioning. The combination with the EBL have been not performed in this case, due to the inconveniences of working with this negative resist and because it is already demonstrated its feasibility [45].

The method consists of inducing the local modification of the epoxy based resist, without been exposed but soft baked, by applying a positive voltage between the silicon and the AFM tip.

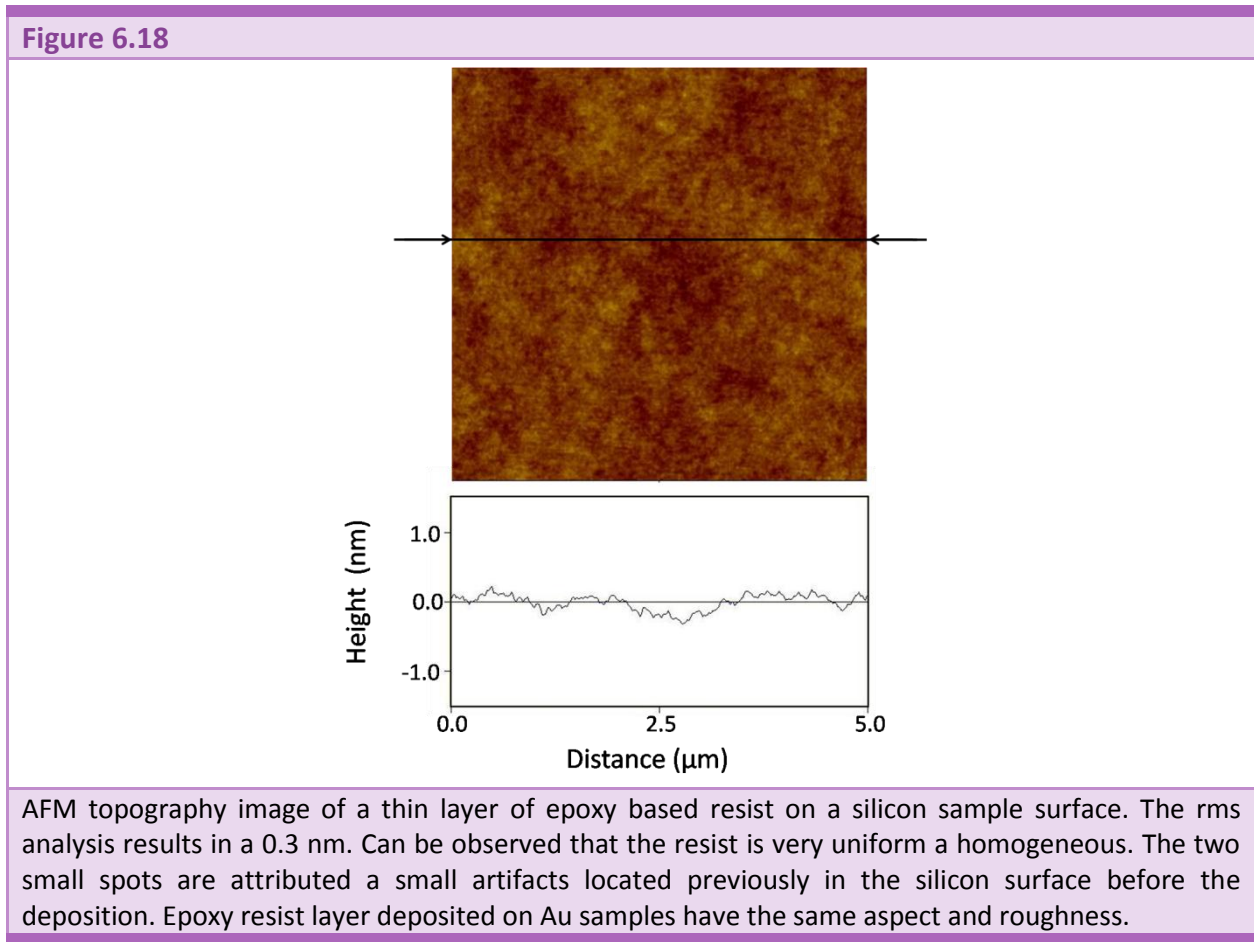
Similar results than in the previous case have been obtained; a hole is also directly produced on the epoxy based resist and silicon surface is simultaneously oxidized even in the case where a hole has not been created. The most remarkable difference is that the threshold voltage for the epoxy based resist is higher than for PMMA.

6.3.1 Additional/Specific experimental details

Very low viscosity resist (mr-EBL 6000.1 XP) which is optimized to obtain 100 nm thickness layers is dissolved in PGMEA. Before deposition, the surface is cleaned by dipping the sample for 1 minute in acetone and 1 minute in isopropanol (IPA). Then it is rinsed in water and dried with N_2 , and finally dehydrated during 30 minutes at 200 °C in a convection oven. The deposition on a silicon (100) surface (p-type, resistivity = 4 Ω cm) sample is performed by spinning coating at 3000 rpm during 45 seconds with an acceleration of 400 rpm/sec, as has been wider explained in previous chapters. The resist is soft baked during 15 minutes to be cured (ramp temperature from 65 °C to 95 °C in a hot plate). In some samples a 50 nm thick Au layer is deposited on the silicon before the resist deposition. The Au layer is deposited by e-beam evaporation (ambient

temperature, $2 \cdot 10^{-4}$ Pa, 2 \AA/s). Under the Au layer a 2 nm thick Cr layer is deposited to improve the Au adhesion to the substrate using the same conditions described for the Au layer deposition.

In order to obtain thin layers (<30 nm thickness) of epoxy based resist, the concentration of mr-EBL 6000.1 XP resist is reduced by adding more PGMEA. The new mixture has a proportion of 1:2 mr-EBL 6000.1 XP:PGMEA.

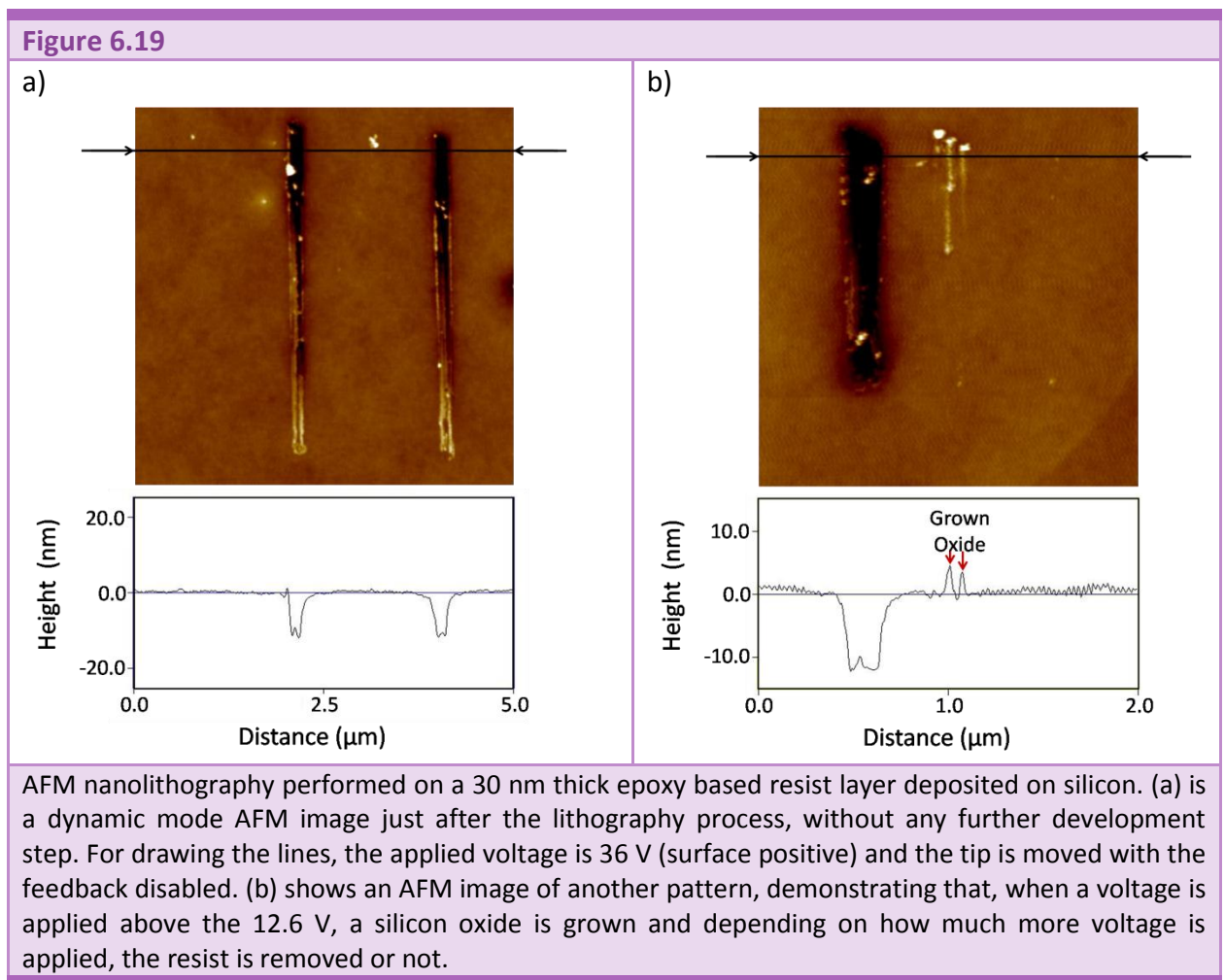


Epoxy based deposited resist roughness after the deposition on the silicon sample is lower than 0.5 nm rms and very uniform and homogeneous (Figure 6.18). The final thickness of the epoxy based resist is measured with AFM after performing UV lithography on the thin layer. UV lithography is performed using a mask aligner with an Hg lamp working in I line at 9.1 mW/cm^2 . Although the resist is very thin, at least 36.4 mJ/cm^2 are needed as a minimum value to activate the PAG. Higher concentrations on PAG can allow a better sensitivity. In the cases that the sample has been UV lithographed (to allow the measurement of the deposited resist thickness) is PEB and developed using PGMEA as the usual procedure.

The same process, of applying a voltage while the tip is defining a line, is used to perform the lithography on PMMA.

6.3.2 Results on Si surfaces

The behavior is very similar to the PMMA films. Figure 6.19.a shows AFM lithographed lines obtained in a 15 nm thick epoxy based resist layer deposited on a silicon surface. The tip was moved while applying a voltage of 36 V (tip positive). The profile at the bottom measured that the depth of the lines is 12 nm.



Operating in this way, a local modification of the polymer is performed where the polymeric layer is completely removed and no bulge appears at the sides of the created trenches. The fact that the measured depth (12 nm) is different than the real thickness of the resist (30 nm) can be

attributed to the combination of two phenomena. First, it is possible that the convolution of the actual trench with the tip is causing the loss of vertical resolution. This convolution can be caused directly by the initial tip geometry but also because the tip can result damaged during the lithography. However, the final outcome is that the dimensions of the trench do not allow the tip to get fully inside. In Figure 6.20 is schematized how the convolution can affect to the measuring of the steps. In Figure 6.20.a, a sharp tip is resolving nicely the two spheres whereas if the tip becomes blunter (less sharp), the resolution is worse as shown in Figure 6.20.b. In addition, there will be a silicon oxide growing on the silicon surface while applying voltage. Although typical values for this oxide thickness range between 4 and 8 nm, some thicker artifacts can be also grown if the applied voltage is very high.

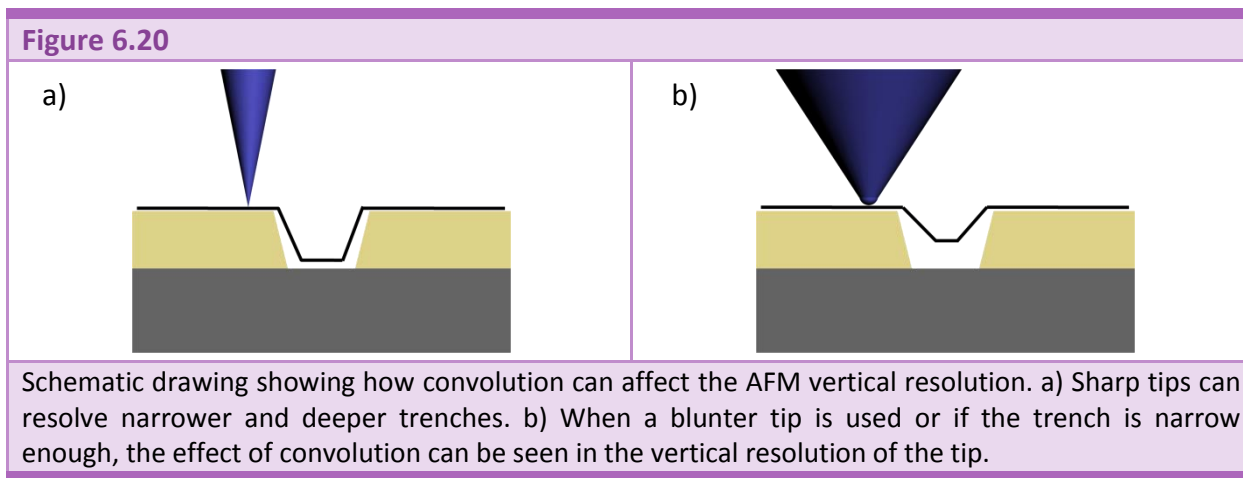


Figure 6.19.b shows another pattern defined on a 30 nm thick epoxy based resist layer. In this case, the applied voltage was deliberately selected to be close to the threshold voltage required to induce a hole on the epoxy based resist (30 V). Next to the lithographed line, where the resist have been removed, there are three small lines that have been also lithographed using the same method. In this case, the lines are raised. These lines correspond to the AFM oxidized surface. The same result as for PMMA is repeated again, silicon surface is oxidized even in the case where trenches are not created in the epoxy based resist after the AFM lithography.

One missing experiment is the confirmation of the grown silicon oxide induced by applying a voltage. This is assumed because the sample is silicon as in the PMMA case. When a higher voltage than the needed to make local oxidation on silicon is applied for the lithography of lines, if the epoxy based resist is not removed, there is a silicon oxide grown between the silicon surface and the epoxy based resist. The resist layer increase it thickness 2-3 nm in the performed lines. In the bottom part of Figure 6.19.b, two spikes are marked corresponding to the higher height lines.

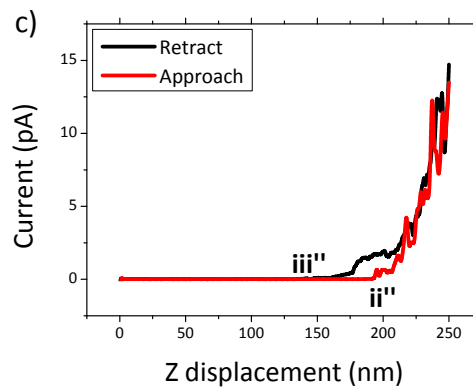
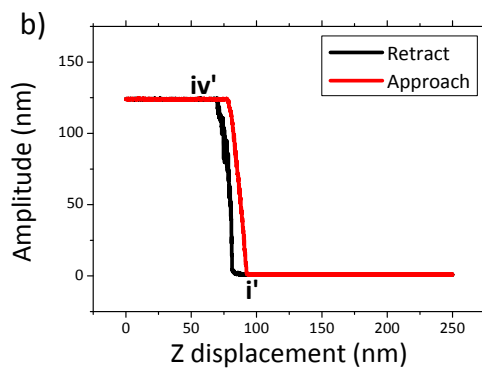
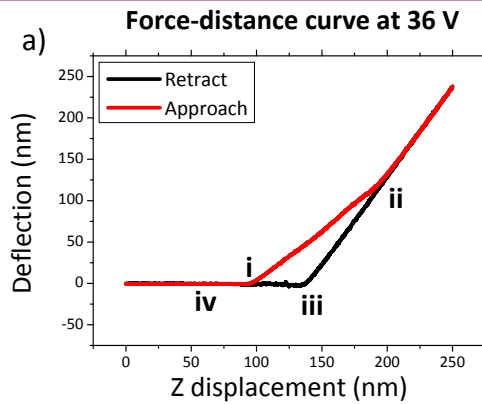
The most important issue for realization of the HF experiment is the alignment. Epoxy based resist is a negative resist what means that the exposed areas remain and the non exposed are dissolved in PGMEA when it is developed. For this reason, the combination with another lithographic technique (i.e. UV lithography or EBL) in order to pattern alignment marks is not possible. Developing the samples to obtain the alignment marks will make disappear all the non exposed resist and, in consequence, in nowhere will be possible to perform the AFM lithography.

Patterns performed using AFM lithography are very small and almost impossible to find once the sample is get out from the AFM stage. The best strategy is to etch some alignment marks on to the silicon surface. Small steps in the silicon surface can give enough contrast to focus with the AFM optical camera and ease the determination of the position and rotation of the sample. Then, after performing the HF, coordinates can be repeated and patterns founded. It has to be taken into account that after the HF etch, the patterns should be holes inside the silicon due to the silicon consumption for silicon oxide formation.

To finally compare the results obtained between the two polymeric resist, force plots of the lithographed process have been performed measuring the current simultaneously. In Figure 6.21 is represented force-distance (Figure 6.21.a), amplitude-distance (Figure 6.21.b) and current-distance (Figure 6.21.c) curves took while applying 36 V (the minimum voltage required to make a hole in the non exposed epoxy based resist).

Comparing with the Figure 6.9.a force-distance curve, the force-displacement curves hysteresis (zone compressed between i and iv points in the approach and retract curves) is very different. Firstly is remarkable that the jump-to-contact point is missing. The tip seems to get gradually inside the polymer due to its softness. In point ii the tip enters in contact with silicon, arriving to a harder material. In the retracting part, as the hole in the epoxy based resist have been already done, the jump-off-contact takes place in iii point and the tip fully separates from the substrate in iv point, due to the epoxy based thickness. This information can be contrasted with the amplitude-distance curve, which indicates that once the tip enters in contact with the polymer in the point i' it stops to vibrate. This result can be explain due to the fact that the tip starts to be trapped into the soft polymer preventing the vibration of the cantilever. The cantilever cannot start to vibrate again until it gets out of the polymer hole, in point (iv'). The hysteresis showed in the amplitude-distance curve is due to the fact that the cantilever cannot start to vibrate at the same point that it stopped due to the thickness of the epoxy based resist removed, i.e. the cantilever stops to vibrate as soon as it touches the polymer but it cannot vibrate again until it is fully out of the polymer hole even it have already started to jump-off-contact.

Figure 6.21



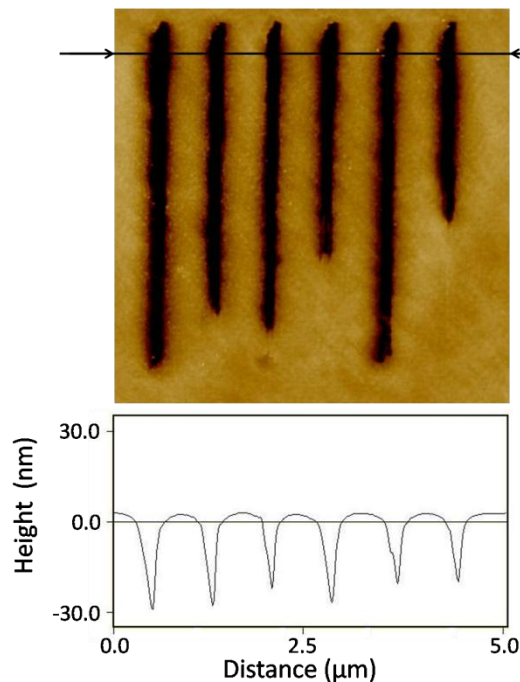
Force-distance curves simultaneously acquired while applying 36 V. a) Force-distance curve demonstrating that the tip gets inside the polymer layer (travel from point *i* to *ii*) and finally reaches the silicon surface (point *ii*) until it is jumped-off-contact (point *iii*). b) Amplitude-distance curve evidences that when the tip starts to be trapped in the polymer, the cantilever cannot vibrate (point *i'*), just only when the tip is far from the surface it can vibrate again (point *iv'*). c) Current-distance curve elucidates the growth of a silicon oxide in the silicon surface. Once the tip reaches the silicon substrate, a current starts to flow (point *ii''*).

Finally the detection of current confirms the behavior explained and gives some information about what is happening in the silicon interface. As the sample surface is not contacted until the tip arrives at point *ii*, no current is detected until *iii'*. The current decrease can be explained by a combined effect of oxide growth and water meniscus thinning.

6.3.3 Results on Au surfaces

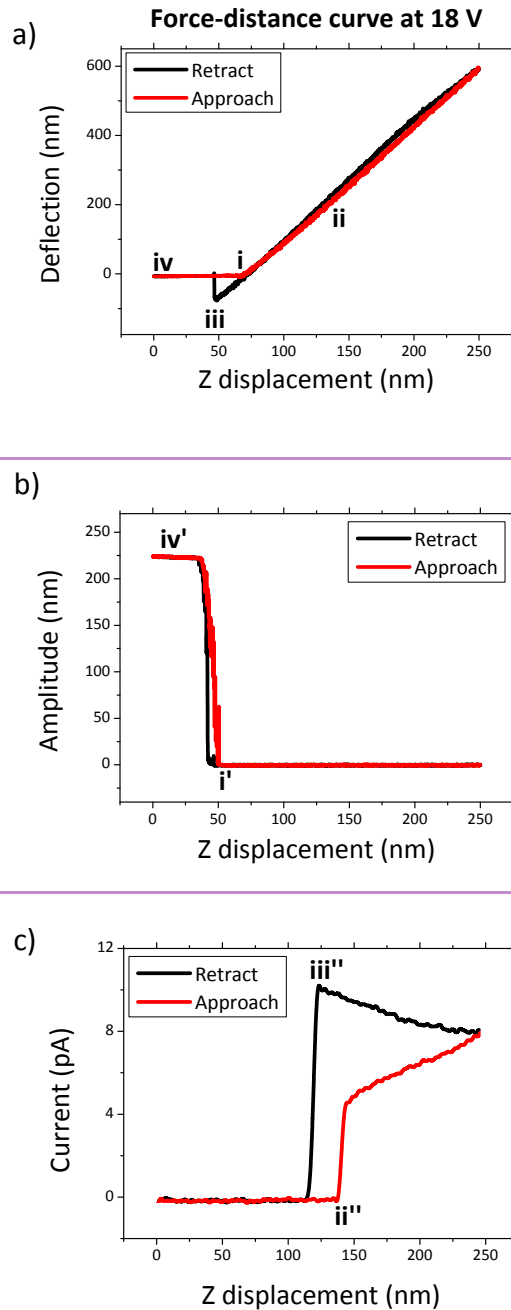
By depositing an Au layer on the Si sample before the epoxy based resist allows to improve the conduction of current and to avoid the growing of an oxide. Local modifications have been successfully performed by removing the resist (Figure 6.22). No development step is required; the application of a voltage is enough to completely remove the epoxy based resist. In this case, as the samples cannot be oxidized only a hole is transferred to the resist. The enhancement of the conductivity, due to the gold layer, makes the electrical current more uniform and constant. Consequently the lithography is easier to perform and more homogeneous. For that reason, the threshold voltage to perform the local modification in this case is decreased until 18 V.

Figure 6.22



AFM nanolithography performed on a 30 nm thick epoxy based resist layer deposited on gold. The dynamic mode AFM image shows the pattern just after the lithography process, without any further development step. For drawing the lines, the applied voltage was 36 V (surface positive) and the tip is moved with the feedback disabled. The full thickness of the resist is removed.

Figure 6.23



Force-distance curves simultaneously acquired while applying 18 V. a) Force-distance curve showing the travel of the tip during its approach retracts (travel from point *i* to *iv*). b) Amplitude-distance curve evidences that when the tip starts to be trapped in the polymer, the cantilever cannot vibrate (point *i'*), just only when the tip is far from the surface it can vibrate again (point *iv'*). c) Current-distance curve elucidates that the tip does not enters in contact with the Au surface until point *ii* because a 4 pA current start to flows at the same moment in point *ii''*. Due to the conductivity of the Au layer, the current increases till 10 pA and finally it stops to flow (point *iii''*).

The only drawback that can be attributed to gold coated samples is that, as the current is larger than in the case of silicon; larger patterns are obtained, meaning that line widths or spots diameters of the patterns are bigger than for non coated samples. Further optimization of the applied voltage conditions for each tip and surface have to be done to not diminish the resolution.

In Figure 6.23 is plotted one of the force-distance curves studied to elucidate the mechanism of the lithography when the non exposed epoxy based resist is on a gold coated silicon sample. Force-distance curve (Figure 6.23.a) presents a force-displacement hysteresis very similar to the Figure 6.9.a. As in the previous case, the jump-to-contact point is missing, but in these conditions, the tip gets inside the polymer more abruptly due to the high conductivity of the Au layer. Until the point *ii*, the tip does not enter in contact with the Au surface and, as a consequence, a 4 pA electrical current starts to flow as it is remarked in point *ii''* in the current-distance curve (Figure 6.23.c). Even the current detected in Figure 6.23.c increases from 4 pA to 10 pA, it is more homogeneous and stable than in the previous case. It is also important to note that current flow is stopped in point *iii''* when the tip has not yet arrived to the jump-off-contact (point *iii*). This result can be explained due to a transient non-contact between the tip and the sample. Epoxy based resist is a very hydrophobic material, hence the formation of the water meniscus is less probable. The existence of a water meniscus would kept the electrical current flow until the jump-off-contact point or its break.

In gold coated silicon surfaces, no oxide is grown and if a force-distance curve is repeated in this position more than once, a similar level of current is always detected.

6.3.4 Discussion

What is expected of applying voltage with the AFM on a polymeric resist is a very local exposition caused by the incident electrons as it is reported in [46] with PMMA. However, in the experiments presented in this section, it has not been possible to find the value of applied voltage to expose without removing the resist.

The applied voltages needed to perform the local modification of the resists depend on the polymer thickness and properties but also in the sample conductivity. Gold coated surfaces cannot be oxidized, therefore current flow between tip and surface is almost constant during the application of voltage. On the other hand, while applying voltage in a silicon surface, a silicon dioxide grows decreasing the current flow. In addition, it has been observed that, at

same polymer thickness on silicon, PMMA is easier to remove. Probably this is related with the polymer structure.

The main differences between the local modification of PMMA layers and epoxy based layers can be summarized in two. First, the PMMA layer seems to break easily, provoking an abrupt jump-to-contact point showed in the force-distance curve. This can be due to a higher presence of porous in PMMA layer which also justifies both the lower threshold voltage than in the epoxy based case and the rapid appearance of flowing current that can make grown a silicon oxide in the interface even before the hole is created. In epoxy based resist layers, the tip enters gradually inside the polymer performing a hole and the current does not start to flow until the tip touches the silicon surface.

The second difference relies in the fact that, while PMMA is a positive resist for EBL that by AFM lithography also behaves as positive (the exposed areas are removed), the epoxy based resist is a negative resist for UV lithography and EBL that behaves as a positive resist when it is AFM lithographed.

For that reason, non exposed epoxy base resist AFM lithography is a difficult process to be combined with others techniques. Furthermore, working with a negative resist with equipment not prepared to, adds the drawback of solving the accidental possible exposing of the resist by the effect of white light sources, like optical microscopes and cameras illumination or the standard illumination of the laboratories (without the yellow filters that are used in photolithography areas). Thus, complicates its processing and makes not possible the alignment.

These disadvantages make this lithography method less interesting and just useful in very specific applications. Elaborate process flows afterwards the lithography to fabricate a device may be possible but a lot of careful with light source must be taken. The most important fact is that the same advantages that can bring in the use of this resist can be much easier reproduced using PMMA.

Therefore, in order to simplify complete the study, AFM lithography on exposed epoxy based resist thin layers has been tested.

6.4 LOCAL MODIFICATION OF THIN EPOXY BASED RESIST LAYERS

Experiments are performed in an epoxy based resist that it is completely processed. The resist is patterned using UV lithography and the solvent is evaporated, the polymer chains are cross-linked, and it is also hard baked. The resist behavior is found to be different than for the non exposed case, which is attributed to the fact that the cross-link changes the characteristics of the resist completely.

6.4.1 Additional/Specific experimental details

Two different surfaces have been used to perform these experiments. Silicon (100) (p-type, resistivity = $4 \Omega \text{ cm}$) surface and the second is the same silicon surface but coated with 2 nm thick chromium layer (as adhesion layer) and 50 nm thick gold layer. Both layers were evaporated at room temperature at $2 \cdot 10^{-4} \text{ Pa}$.

The samples are cleaned by dipping for 1 minute in acetone and 1 minute in isopropanol (IPA). Then it is rinsed in water and dried with N_2 , and finally dehydrated during 30 minutes at $200 \text{ }^\circ\text{C}$ in a convection oven. Epoxy based resist (mr-EBL 6000.1 XP) was dissolved in PGMEA with a ratio of (mr-EBL 6000.1 XP):PGMEA 1:2, resulting in 15-20 nm thickness layers. The mixture is spin coated on the samples at 3000 rpm during 45 seconds with an acceleration of 400 rpm/sec. After the deposition, the samples are soft baked in a hot plate during 10 minutes (ramp temperature from $65 \text{ }^\circ\text{C}$ to $95 \text{ }^\circ\text{C}$) and exposed when it is cooled with a dose of 91 mJ/cm^2 . Following the standard fabrication steps of the resist a PEB is performed in a hot plate during 20 minutes and 24 hours later the samples are developed in PGMEA. Finally they are hard baked during 2 hours in at $120 \text{ }^\circ\text{C}$ and in an atmosphere saturated of nitrogen.

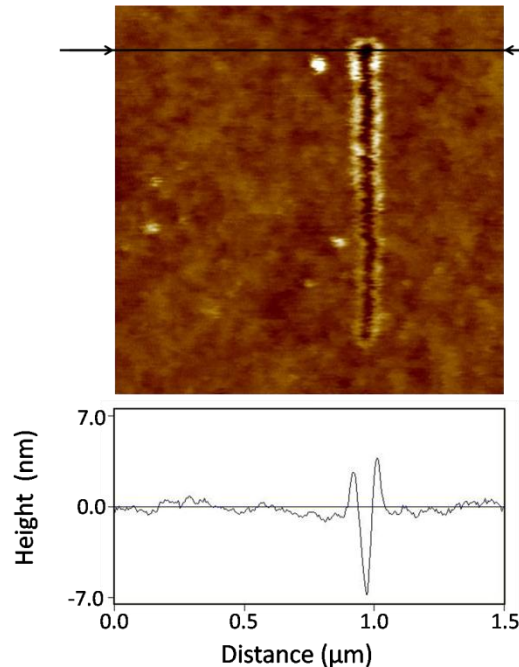
The process used to perform the lithography in dynamic mode has been described previously in section 6.1.4. In this case, the local modification of the resist could be done either applying voltage or just applying a force from the tip to the surface.

6.4.2 Results on silicon surfaces

Experiments performed on exposed and cured epoxy based resist show that the polymer conductivity changes with respect to the non-exposed version. The cross-linking process of the polymer modifies its chemical structure avoiding the flow of electrical current. These well

known isolating properties of epoxy resists arise also during AFM local modification while applying a voltage. The polymer is not removed; it is just moved and piled up. The bulges showed at the edges of the line patterned in Figure 6.24 confirm that this effect involves just the displacement of polymer and not its removal. Therefore, this local modification of the polymer consists in a penetration of the AFM tip inside the polymer and it is known as mechanical indentation [6, 11] and was introduced previously in Section 6.1.1.1.

Figure 6.24

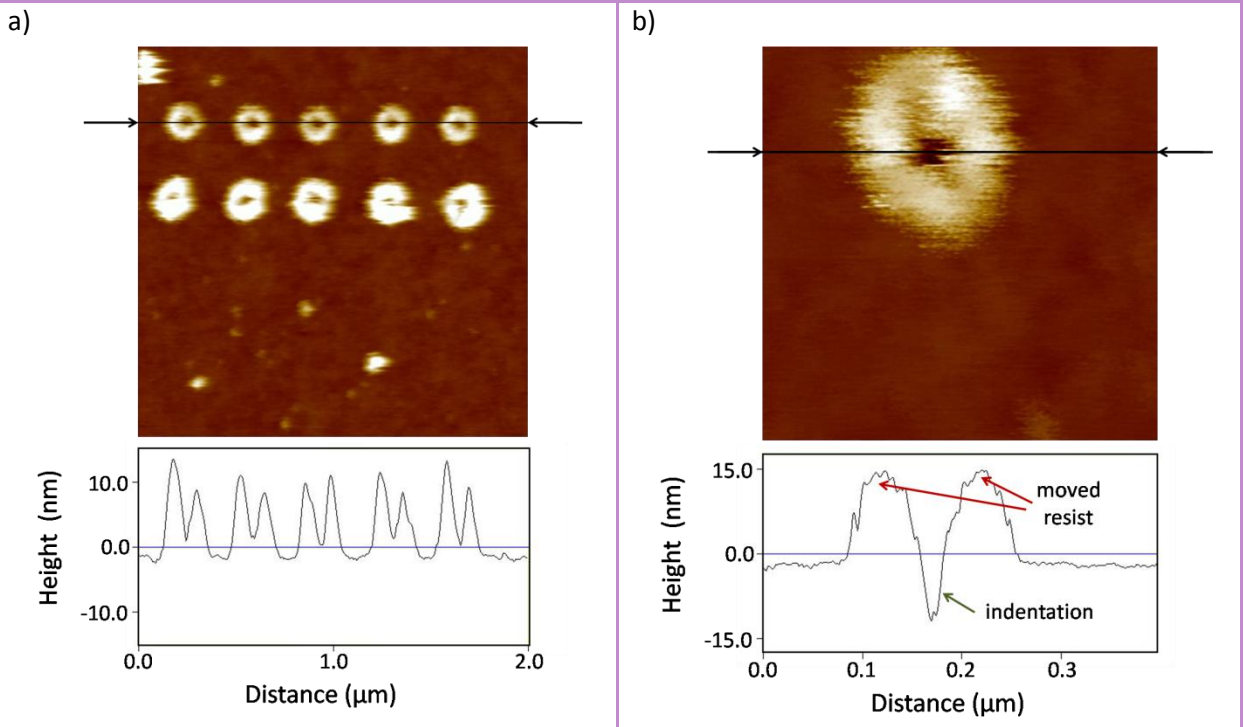


Topography AFM images. Lines were tried to be made by applying 36 V while displacing the AFM tip. The profile shows that the resist is moved on to the edges and, as it is accumulated, it is very difficult to pattern long lines.

Patterning using the mechanical indentation is more complicated because the resist is not eliminated while the tip is advancing inside the resist, therefore the resist is accumulated. This effect impedes the patterning of long lines or big patterns.

Figure 6.25 is a topography image taken just after performing 10 force curve plots in different positions. The five first rings (in the top of the image) are performed while applying 9 V, and the second row of rings is performed at 18 V. Higher voltages provoke more amount of resist moved. Even the profile of Figure 6.25.a seems that the tip is not indenting the resist, Figure 6.25.b, a zoom of a selected ring, clearly demonstrates that it is an issue of resolution. In addition, the tip radius limits the evaluation of the hole size. It can be assumed that the diameter of the hole is the same or slightly bigger than the diameter of tip.

Figure 6.25

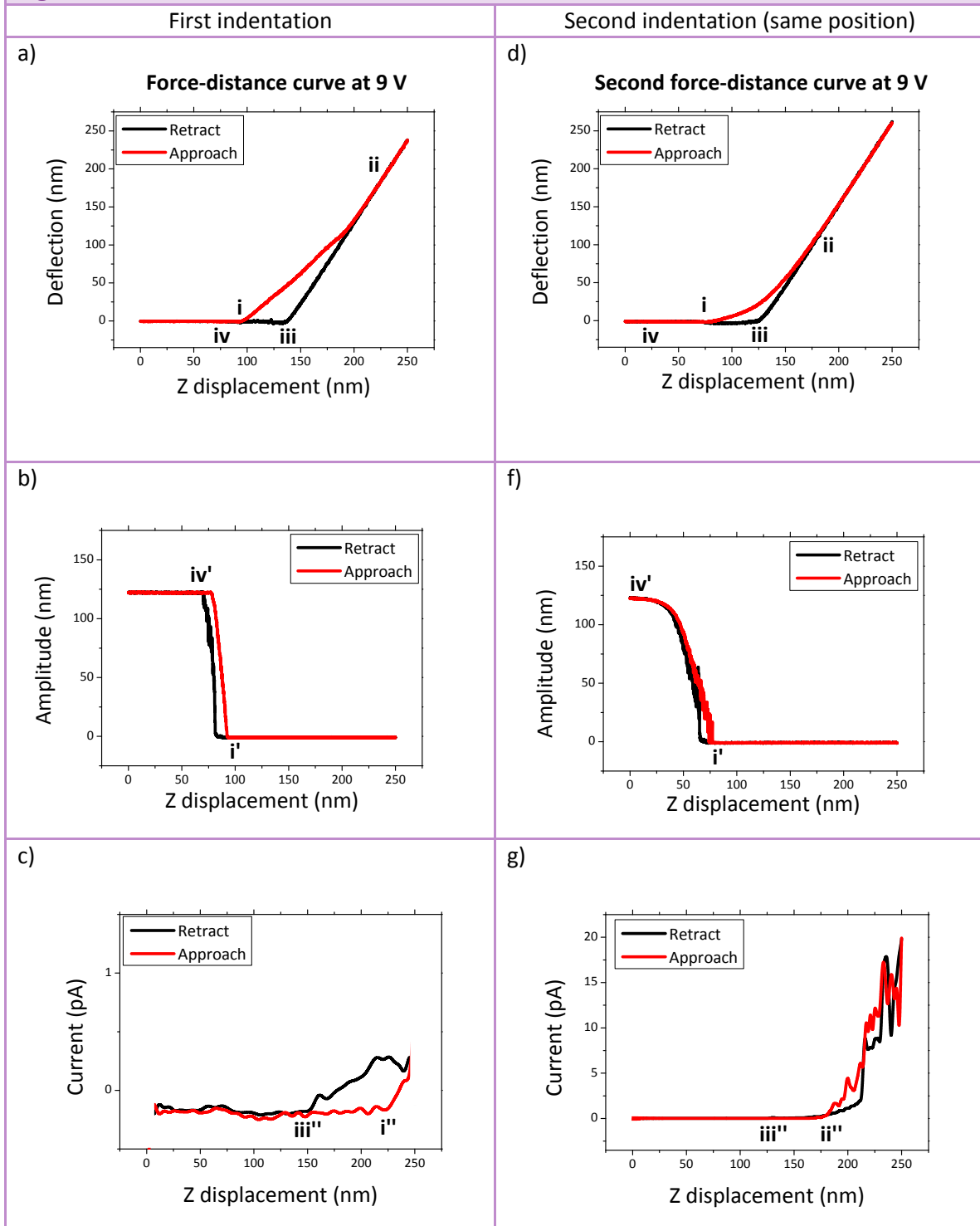


b) Scanned surface after performing force curves applying voltage and detecting simultaneously the current. Up line holes are performed at 9 V and second line at 18 V. Even the profile shows that the hole is not going inside the resist, making a zoom of one of the patterns it is clear that the resist moved comes from inside.

Imaging resolution is a problem in order to fully understand the effect produced in the exposed resist. Neither topography images nor profiles can elucidate if an amount of resist is compressed at the bottom of the tip or it is fully moved on to the sides and if a silicon oxide is grown or not.

The acquisition of force curve plots while applying voltage again helps in the comprehension of the phenomena occurred during the lithography. In Figure 6.26 is represented the simultaneous acquisition of force-distance curves performed in the same position at the same voltage. The applied voltage, 9 V, corresponds to the usual threshold voltage to obtain an anodic oxidation of the surface. First mechanical indentation curves are in the left column of the Figure 6.26 and the second are in the right column.

Figure 6.26



Force-distance curves acquired while applying 9V. Right column corresponds to the first indentation made on the resist, left column is a second indentation in the same position.

First indentation shows a well known force-distance curve from the previous sections (Figure 6.26.a). The force-displacement hysteresis corresponds to the travel of the tip inside the polymer (from *i* to *ii* points) arriving to the substrate. The tip jumps-off-contact and gets far from the surface from *iii* to *iv* points. In this case that the layer below the epoxy based resist is silicon, a tiny current is detected at point *ii''* and flows until the tip jumps-off-contact (points *iii''* and *iii* respectively).

When a second indentation is performed in the same position the force-distance curve (Figure 6.26.d) presents a shorter force-displacement hysteresis. This can be attributed that in the previous curve, not all the depth of the polymer thickness has been removed in the first indentation. With the second indentation it is really achieved the silicon surface at point *ii* allowing the flowing of current as it is remarked in point *ii''*. The silicon oxide is grown from *ii''* point to *iii''* point (Figure 6.26.g). The value of the electrical current returns to zero when the tip jumps-off-contact in point *iii*.

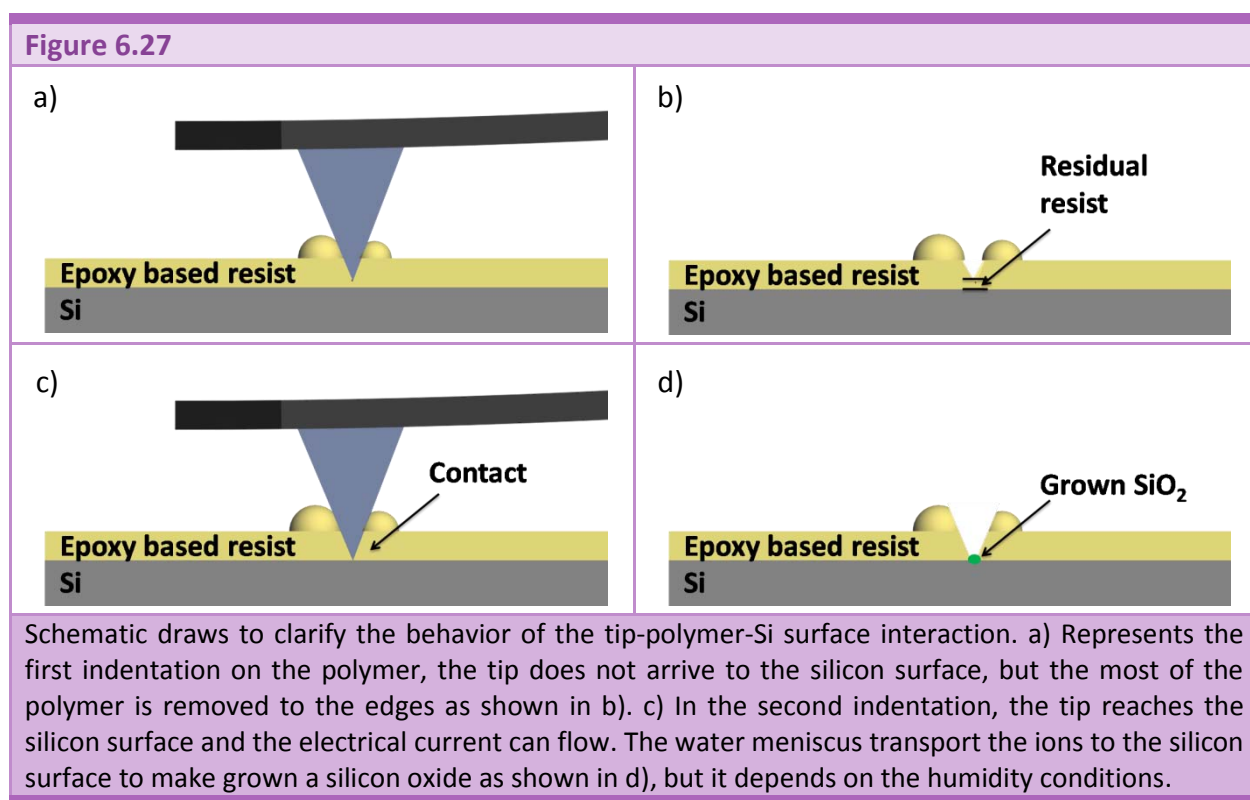


Figure 6.27 consists in schematic draws to ease the comprehension of the information obtained from Figure 6.26 curves. During the first indentation the tip does not remove all the polymer thickness (Figure 6.27.a), leaving a very thin layer of resist that allows the transport of a very low current flow. If a second indentation is performed in the same position, the polymer

thickness is fully removed, a physical contact between tip and silicon occurs (Figure 6.27.c) and an oxide dot is grown on the silicon surface (Figure 6.27.d).

If a third indentation is performed in the same position, as the oxide dot is already grown, no current can be detected. Even though, the force-distance curve stills present a small force-displacement hysteresis due to the drift of the AFM equipment.

6.4.3 Results on Au surfaces

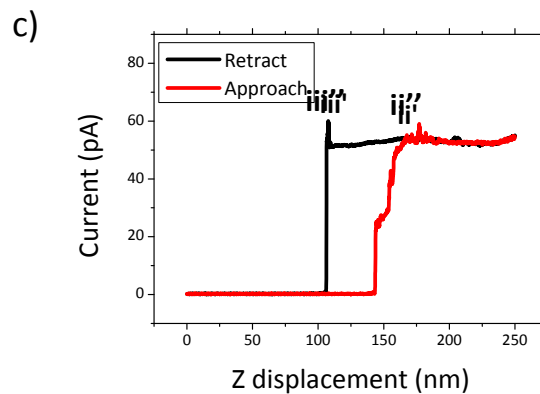
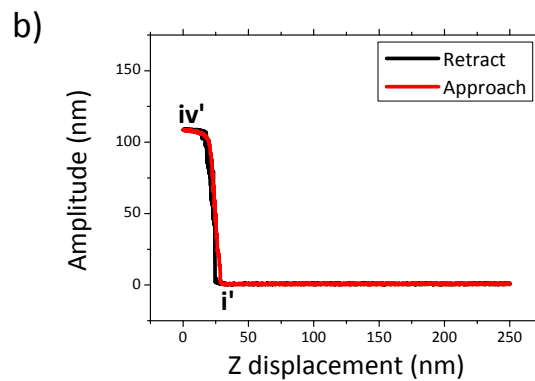
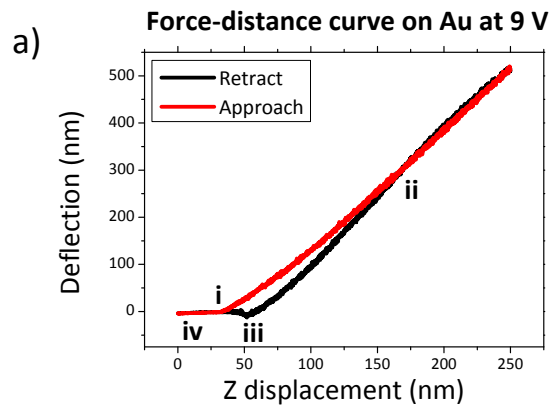
Doing the same experiment on gold coated silicon surfaces, complementary information has been obtained. Gold is interesting from the point of view of its high conductivity and, as it is a noble metal, its resistance to oxidation. Like in the previous section, where the epoxy based resist was not exposed, the expected electrical current detected while performing force-distance curves should be higher than in silicon, without decreasing at any time due the absence of oxide. Also the detection of the current should be possible as times as the curve is performed in the same place.

In Figure 6.28, the force-distance curves on gold coated silicon surfaces are presented. To compare the curves with the silicon surfaces without coating, same voltages have been used. When exposed resist is used, the local modification consists in an indentation, meaning that the voltage applied is not relevant for the lithography itself but can bring information about the conductivity and the process of modification.

Figure 6.28.a is the force-distance curve showing the characteristic behavior of an indentation. At the same time, the amplitude-distance curve (Figure 6.28.b) reveals when the cantilever is oscillating and when it is stopped due to the influence of the polymer. Current-distance curve (Figure 6.28.c) confirms what it was expected: higher currents than for silicon surfaces (~ 50 pA), currents more homogeneous and stables (due to the absence of a growth oxide) and repeatability even if the performance is at the same point.

Thus confirms that the epoxy based resist is fully removed by the indentation and the tip and gold surface enters in contact in point *ii*, allowing. When tip and sample are in contact, the current can start even if no water meniscus is formed (point *ii''*) and it stops when, at the retracting part, tip and surface starts to not be in contact (point *iii''*).

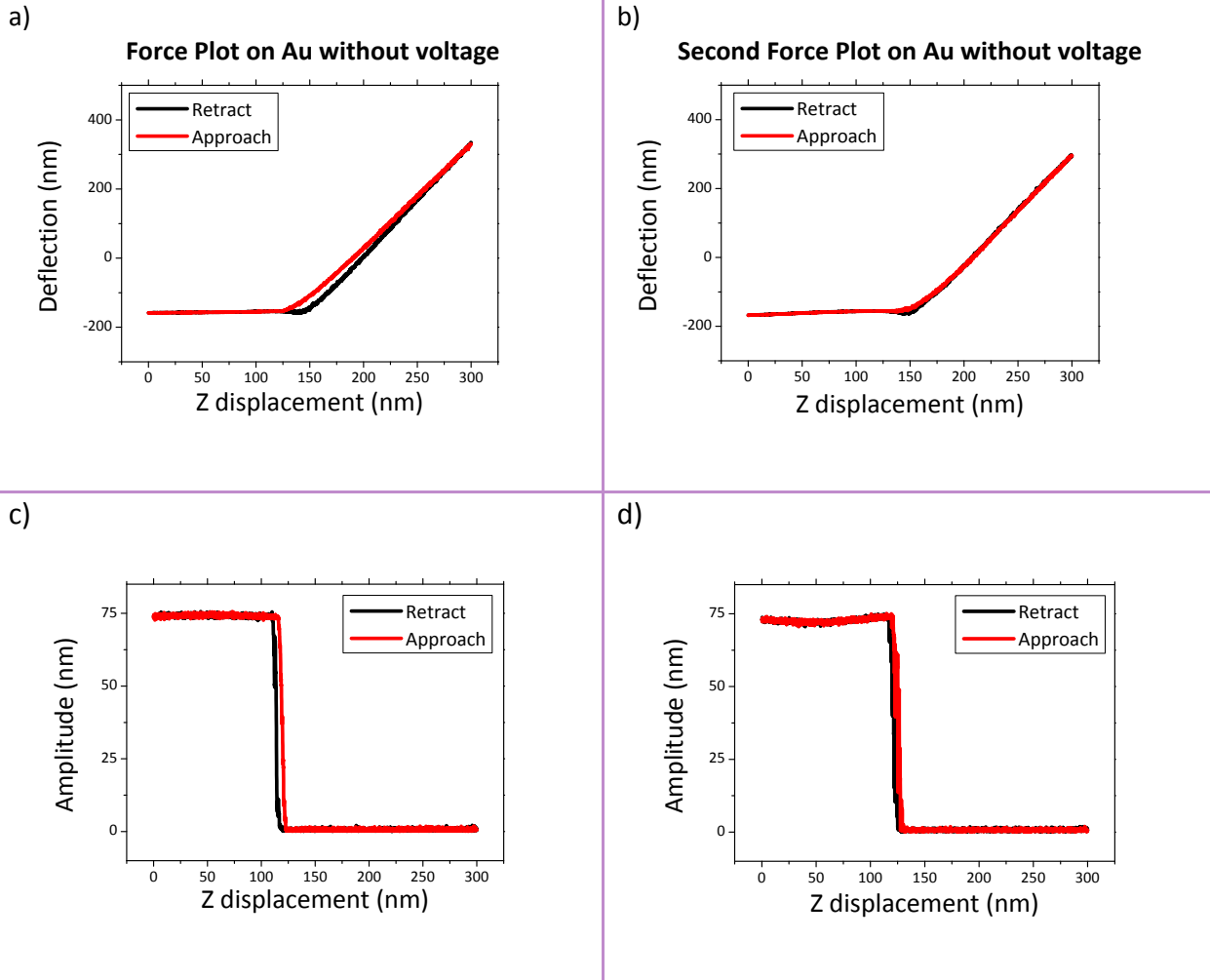
Figure 6.28



Force-distance curves simultaneously acquired while applying 9 V. a) Force-distance curve showing the travel of the tip during its approach and until it fully retracts (travel from point *i* to *iv*). b) Amplitude-distance curve evidences that the cantilever cannot vibrate (point *i'*) when the tip starts to be trapped in the polymer. When the tip is fully retracted from the surface, it can vibrate again (point *iv'*). c) Current-distance curve elucidates that the tip does not enters in contact with the Au surface until point *ii* because a 50 pA current start to flows at the same moment in point *ii''*. Due to the conductivity of the Au layer, the current is kept constant till it stops to flow (point *iii''*).

Indentation on polymers is a non reversible lithography. Once the hole is created it is not possible to make it disappear by the effect of the AFM tip. Repeating indentations in the same point, without changing the position of the tip respect to the sample (Figure 6.29), as the hole has been created, no force-displacement hysteresis is observed (Figure 6.29.b).

Figure 6.29



Consecutive force-distance curves applied in the same position. a) and b) force-distance curves showing the travel of the tip. In a) takes place the modification of the polymer, b) demonstrates that a small aperture have already been open and the paths are equal. c) and d) are amplitude-distance curves, c) evidences that the point where the tip stops to vibrate is different from the point it starts again due to the polymer removal. s) As the polymer have been removed, the cantilever stops to vibrate and starts again at the same point.

6.5 APPLICATIONS

From the above described experiments, two relevant properties of the epoxy based resist have been evidenced; its feasibility to be patterned using different techniques and its insulating behavior once it is exposed and cured.

Using these results, two applications can be suggested. The first one consists on the fabrication of nanocontacts by indentation like is reported in [47]. An ultrathin exposed and cured epoxy based resist layer can be deposited on a conductive structure. An AFM can be then used as a nanoindenter. In [47], conductive tips are employed, therefore a continuous measurement of the resistance between the conductive tip and the conductive layer can be obtained while indenting. Thus, the measured resistance is the trigger parameter to stop the indentation allowing a very accurate control of the process. The indented hole is subsequently filled by a metal to create the contact on the underlying layer. Nanocontacts in the range of 1 to 10 nm² can be created with this technique.

A second application for the AFM local modification of polymers is the fabrication of nanopore arrays useful for ultrasmall electrodes. Ultrasmall electrodes (micrometer size or smaller) offer a number of advantages when are employed in electrochemical studies and applications [48]. Nanoelectrodes may be defined as electrodes with a critical dimension in the nanometer range. By critical dimension is meant the dimension which controls the electrochemical response [49].

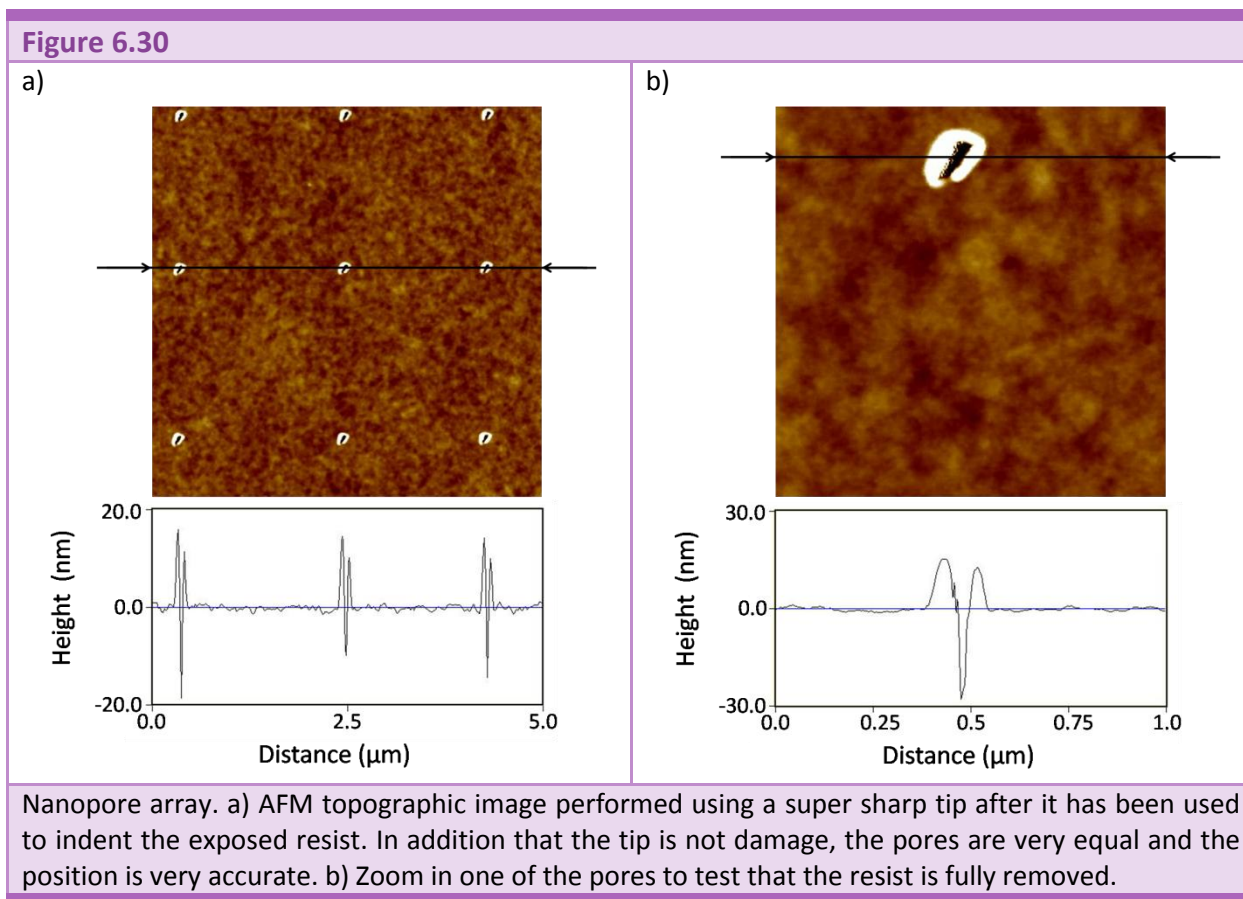
The interest in nanoelectrodes comes from three main reasons: the rapid establishment of steady-state limiting currents, which are essentially convection independent; the increased current densities that are observed as the electrode radius is reduced, and the significant improvement in the Faradaic-to-capacitive current ratios obtained [50]. Nanoelectrodes detect very small electrical current; typically it is ranged in the order of a few pA, for that reason appears the motivation of fabricate nanoelectrode arrays. Nanoelectrode arrays operates as a set of nanoelectrodes connected in parallel, thus allows the amplification of the signal.

In this Thesis, the fabrication of a nanopore array electrode is considered to estimate the utility of this lithographic method. Previously reported nanopore arrays have been fabricated by using the Focused Ion Beam (FIB) [51]. In addition, planar nanoelectrodes can be fabricated by EBL [52, 53].

By AFM indentation of exposed epoxy based resists, it is possible to define a large number (>100) of nanoapertures in the insulating resists. We have found that indentation on this resist is very stable. The fabrication of the nanopore array can be automated by the NanoScope IV

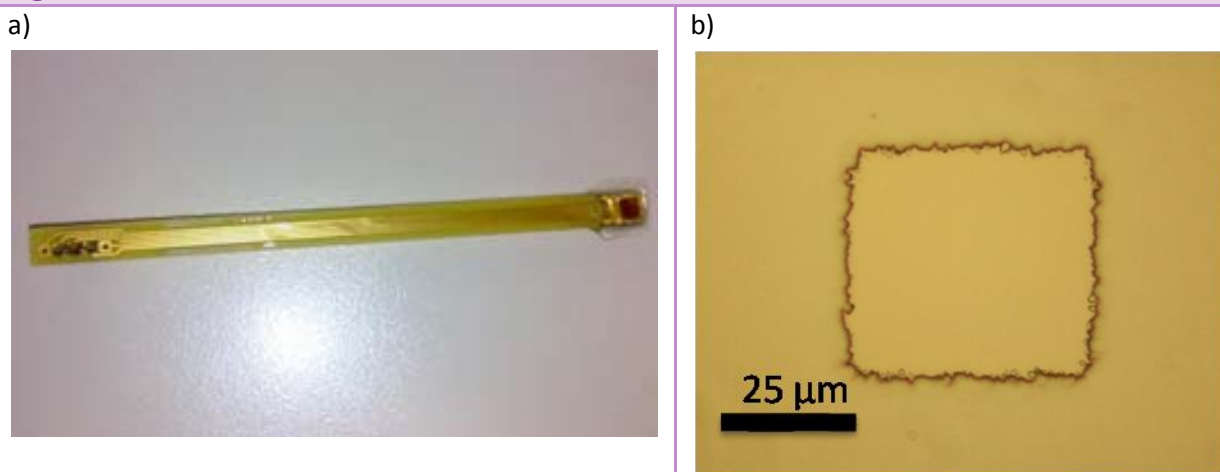
software with the NanoMan application of the Dimension 3100 system. This control on the dimensions and positions of each nanoelectrode is very important in the field of the electrochemistry to study the behavior of the nanoelectrodes nets, which is a very recent research field.

Figure 6.30 demonstrates the feasibility of this technique to perform several indentations on the exposed epoxy based resist. Figure 6.30.a is a partial view of a 15x15 nanopore array. The good positioning of the AFM allows to exactly locating each pore and the indentation allows to fully penetrating inside the resist as shown in a bigger zoom in Figure 6.30.b, where the pore is 30 nm deep at least. This experiment was performed using super sharp silicon tips in order to obtain smaller electrodes.



Epoxy based resist insulating properties have been tested for nanoelectrode application. Gold coated silicon surfaces have been spin coated with a thin (~25 nm) layer of resist. The resist is exposed with a mask to leave a small area of gold without covering with the resist after the development. This area is needed for the wire bonding. After that, the chip is encapsulated leaving a 50x50 μm^2 area to be in contact with the chemical solution (Figure 6.31).

Figure 6.31



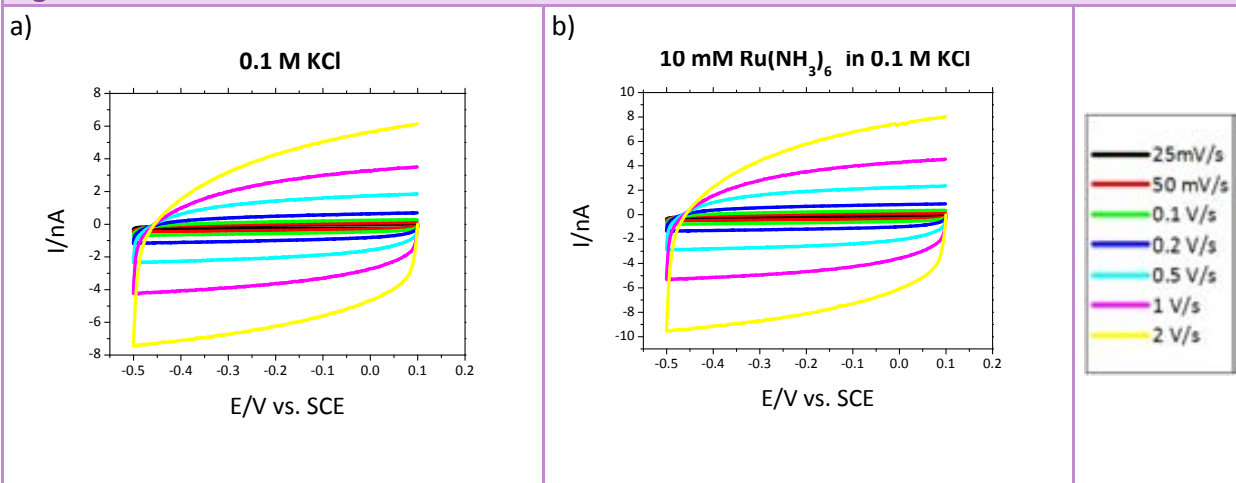
Chemical electrode. a) Picture of a wire bounded and encapsulated electrode. b) Optical image of the $50 \mu\text{m}^2$ square of thin epoxy based resist. In this areas is where is designed to pattern the nanopore array by AFM indentation.

Some electrodes have been tested by cyclic voltammetry immersing them in of 10 mM of $\text{Ru}(\text{NH}_3)_6^{3+}$ in 0.1 M KCl after their precious electrochemical activation in 0.1 M KCl. $\text{Ru}(\text{NH}_3)_6^{3+}$ was chosen because it is a reversible redox couple perfectly characterized which allows the activity of the surface electrodes. For a redox reversible couple, the current registered as a response of applying a triangle voltage function over the electrode (voltammogram) follows a well-known theoretical model. This is advantageous because knowing the concentration of the solution and the scan rate, it is possible to calculate the active area of the electrode.

In Figure 6.32 some voltammograms are shown. Note that any chemical reaction is registered through the epoxy based resist. Consequently, the information that can be extracted from them is that the insulating properties of the epoxy based resist, using a thin layer of ~ 25 nm, are good enough in order to perform electrochemistry measurements.

Array of nanopores are already designed to be patterned, in a near future, in this areas of thin epoxy based resist. More experiments and measurements are planned to perform in order to study the behavior of the nanoelectrodes.

Figure 6.32



Voltammograms of a gold substrate coated with a thin film of epoxy based resist (around 25 nm in thickness) without nanopores. The behavior under both KCl (a) and $\text{Ru}(\text{NH}_3)_6^{3+}$ (b) solution implies that the layer is completely insulating so it can be used as a passivation layer for the metal substrate and then the nanopores can be patterned in it to fabricate a nanoelectrode.

6.6 CONCLUSIONS

In summary, in this chapter, it has been presented two methods for fabricating nanometre scale structures by AFM lithography. The methods are applicable to PMMA and epoxy based resist. Nanometer scale patterns on PMMA and non exposed epoxy based resist can be created by applying a voltage between an AFM tip and the surface. The result is that the resist is locally eliminated. Simultaneously with the removal of the polymer, the silicon surface is locally oxidized. The second method consists in removing/displacing the exposed polymers films by indenting with the AFM tip, without the requirement of applying voltage.

Information from AFM electrical current measurements indicates that the mechanism of PMMA and non exposed epoxy based resist elimination is likely to be caused by a local electrochemical reaction involving the transport of OH^- ions through the polymer. This transport of ions is possible because the polymer is not cross-linked. Once the polymer is exposed and cured, it is completely insulating. For that reason, when the polymer is exposed the AFM electrical current measured simultaneously with the indentation, shows no flowing current until the hole is fully defined.

Both methods are useful for making high resolution structures. In comparison with other well-known approaches of AFM lithography, the present methods have the advantages of its direct combination with electron-beam lithography and UV lithography, and, as it is a direct method, there is no need of polymer development after AFM lithography [54]. Both, the electrochemical reaction and the indentation on soft polymers, preserves the tip condition and in consequence its lifetime, and the robustness of the process.

The influence of the substrate has been studied. Performing the experiments in silicon substrate originates the growth of silicon oxide. Electrical current measurements demonstrate that the flow of current in gold coated surfaces is higher and more stable, because substrate oxidation does not occur.

Applications have been presented. The direct removal of PMMA can be combined with EBL to fabricate nanometer scale gaps between two metal electrodes. The mechanical indentation on exposed epoxy based resist can used for the fabrication of nanoelectrode arrays taking profit of the good insulating properties of the resist, the capability to open very small pores and the reproducibility and high resolution of the AFM.

Even there are still a few challenges faced by AFM nanolithography, the mass production of patterns by AFM nanolithography needs to be optimized since it is essentially a serial process,

the high resolution of the fabricated AFM structures and its feasibility to be combined with parallel lithographic process represents valuable advantage in these methods.

6.7 REFERENCES

1. F. Perez-Murano, G. Abadal, N. Barniol, X. Aymerich, J. Servat, P. Gorostiza, and F. Sanz
"Nanometer-Scale Oxidation of Si(100) Surfaces by Tapping Mode Atomic-Force Microscopy".
Journal of Applied Physics, 1995, **78**(11), 6797-6801.
2. R. Garcia, M. Calleja, and F. Perez-Murano
"Local oxidation of silicon surfaces by dynamic force microscopy: Nanofabrication and water bridge formation".
Applied Physics Letters, 1998, **72**(18), 2295-2297.
3. M. Calleja and R. Garcia
"Nano-oxidation of silicon surfaces by noncontact atomic-force microscopy: Size dependence on voltage and pulse duration".
Applied Physics Letters, 2000, **76**(23), 3427-3429.
4. S.C. Minne, S.R. Manalis, A. Atalar, and C.F. Quate
"Independent parallel lithography using the atomic force microscope".
Journal of Vacuum Science & Technology B, 1996, **14**(4), 2456-2461.
5. S.C. Minne, S.R. Manalis, and C.F. Quate
"Parallel atomic force microscopy using cantilevers with integrated piezoresistive sensors and integrated piezoelectric actuators".
Applied Physics Letters, 1995, **67**(26), 3918-3920.
6. M.R. VanLandingham, S.H. McKnight, G.R. Palmese, J.R. Elings, X. Huang, T.A. Bogetti, R.F. Eduljee, and J.W. Gillespie
"Nanoscale indentation of polymer systems using the atomic force microscope".
Journal of Adhesion, 1997, **64**(1-4), 31-59.
7. W.P. King, T.W. Kenny, K.E. Goodson, G. Cross, M. Despont, U. Durig, H. Rothuizen, G.K. Binnig, and P. Vettiger
"Atomic force microscope cantilevers for combined thermomechanical data writing and reading".
Applied Physics Letters, 2001, **78**(9), 1300-1302.
8. T.R. Ramachandran, C. Baur, A. Bugacov, A. Madhukar, B.E. Koel, A. Requicha, and C. Gazen
"Direct and controlled manipulation of nanometer-sized particles using the non-contact atomic force microscope".
Nanotechnology, 1998, **9**(3), 237-245.
9. R.D. Piner, J. Zhu, F. Xu, S.H. Hong, and C.A. Mirkin
"Dip-pen" nanolithography".
Science, 1999, **283**(5402), 661-663.
10. Y. Kim and C.M. Lieber
"Machining oxide thin-films with an atomic force microscope - pattern and object formation on the nanometer scale".
Science, 1992, **257**(5068), 375-377.

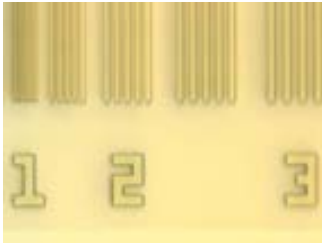
11. M.R. VanLandingham, J.S. Villarrubia, W.F. Guthrie, and G.F. Meyers
"Nanoindentation of polymers: An overview".
Macromolecular Symposia, 2001, **167**, 15-43.
12. G. Binnig, M. Despont, U. Drechsler, W. Haberle, M. Lutwyche, P. Vettiger, H.J. Mamin, B.W. Chui, and T.W. Kenny
"Ultra-high-density atomic force microscopy data storage with erase capability".
Applied Physics Letters, 1999, **74**(9), 1329-1331.
13. P. Vettiger, J. Brugger, M. Despont, U. Drechsler, U. Durig, W. Haberle, M. Lutwyche, H. Rothuizen, R. Stutz, R. Widmer, and G. Binnig
"Ultra-high density, high-data-rate NEMS-based AFM data storage system".
Microelectronic Engineering, 1999, **46**(1-4), 11-17.
14. P. Vettiger, M. Despont, U. Drechsler, U. Durig, W. Haberle, M.I. Lutwyche, H.E. Rothuizen, R. Stutz, R. Widmer, and G.K. Binnig
"The "Millipede" - More than one thousand tips for future AFM data storage".
IBM Journal of Research and Development, 2000, **44**(3), 323-340.
15. H.J. Mamin and D. Rugar
"Thermomechanical writing with an atomic force microscope tip".
Applied Physics Letters, 1992, **61**(8), 1003-1005.
16. D. Fotiadis, S. Scheuring, S.A. Muller, A. Engel, and D.J. Muller
"Imaging and manipulation of biological structures with the AFM".
Micron, 2002, **33**(4), 385-397.
17. J. Hu, Y. Zhang, H.B. Gao, M.Q. Li, and U. Hartmann
"Artificial DNA patterns by mechanical nanomanipulation".
Nano Letters, 2002, **2**(1), 55-57.
18. J.A. Dagata, J. Schneir, H.H. Harary, C.J. Evans, M.T. Postek, and J. Bennett
"Modification of Hydrogen-Passivated Silicon by a Scanning Tunneling Microscope Operating in Air".
Applied Physics Letters, 1990, **56**(20), 2001-2003.
19. P.M. Campbell, E.S. Snow, and P.J. McMarr
"Fabrication of nanometer-scale conducting silicon wires with a scanning tunneling microscope".
Solid-State Electronics, 1994, **37**(4-6), 583-586.
20. S.C. Minne, H.T. Soh, P. Flueckiger, and C.F. Quate
"Fabrication of 0.1- μ m metal-oxide-semiconductor field-effect transistors with the atomic-force microscope".
Applied Physics Letters, 1995, **66**(6), 703-705.
21. P.M. Campbell, E.S. Snow, and P.J. McMarr
"Fabrication of nanometer-scale side-gated silicon field-effect transistors with an atomic-force microscope".
Applied Physics Letters, 1995, **66**(11), 1388-1390.
22. Z.J. Davis, G. Abadal, O. Hansen, X. Borise, N. Barniol, F. Perez-Murano, and A. Boisen
"AFM lithography of aluminum for fabrication of nanomechanical systems".
Ultramicroscopy, 2003, **97**(1-4), 467-472.

23. K. Matsumoto, Y. Gotoh, T. Maeda, J.A. Dagata, and J.S. Harris
"Room-temperature single-electron memory made by pulse-mode atomic force microscopy nano oxidation process on atomically flat alpha-alumina substrate".
Applied Physics Letters, 2000, **76**(2), 239-241.
24. H. Sugimura, T. Uchida, N. Kitamura, and H. Masuhara
"Tip-induced anodization of titanium surfaces by scanning-tunneling-microscopy - a humidity effect on nanolithography".
Applied Physics Letters, 1993, **63**(9), 1288-1290.
25. F. Perez-Murano, K. Birkelund, K. Morimoto, and J.A. Dagata
"Voltage modulation scanned probe oxidation".
Applied Physics Letters, 1999, **75**(2), 199-201.
26. K. Birkelund, M. Mullenborn, F. Grey, F. Jensen, and S. Madsen
"Combined AFM and laser lithography on hydrogen-passivated amorphous silicon".
Superlattices and Microstructures, 1996, **20**(4), 555-560.
27. H.C. Day and D.R. Allee
"Selective Area Oxidation of Silicon with a Scanning Force Microscope".
Applied Physics Letters, 1993, **62**(21), 2691-2693.
28. R. Garcia, M. Calleja, and H. Rohrer
"Patterning of silicon surfaces with noncontact atomic force microscopy: Field-induced formation of nanometer-size water bridges".
Journal of Applied Physics, 1999, **86**(4), 1898-1903.
29. M. Schenk, M. Futing, and R. Reichelt
"Direct visualization of the dynamic behavior of a water meniscus by scanning electron microscopy".
Journal of Applied Physics, 1998, **84**(9), 4880-4884.
30. F. Perez-Murano, C. Martin, N. Barniol, H. Kuramochi, H. Yokoyama, and J.A. Dagata
"Measuring electrical current during scanning probe oxidation".
Applied Physics Letters, 2003, **82**(18), 3086-3088.
31. J.A. Dagata, F. Perez-Murano, G. Abadal, K. Morimoto, T. Inoue, J. Itoh, and H. Yokoyama
"Predictive model for scanned probe oxidation kinetics".
Applied Physics Letters, 2000, **76**(19), 2710-2712.
32. M. Tello and R. Garcia
"Nano-oxidation of silicon surfaces: Comparison of noncontact and contact atomic-force microscopy methods".
Applied Physics Letters, 2001, **79**(3), 424-426.
33. S.F. Lyuksyutov, P.B. Paramonov, S. Juhl, and R.A. Vaia
"Amplitude-modulated electrostatic nanolithography in polymers based on atomic force microscopy".
Applied Physics Letters, 2003, **83**(21), 4405-4407.
34. S.F. Lyuksyutov, P.B. Paramonov, R.A. Sharipov, and G. Sigalov
"Induced nanoscale deformations in polymers using atomic force microscopy".
Physical Review B, 2004, **70**(17), 174110.

35. S.F. Lyuksyutov, R.A. Vaia, P.B. Paramonov, S. Juhl, L. Waterhouse, R.M. Ralich, G. Sigalov, and E. Sancaktar
"Electrostatic nanolithography in polymers using atomic force microscopy".
Nature Materials, 2003, **2**(7), 468-472.
36. A.S. Paulo and R. Garcia
"Unifying theory of tapping-mode atomic-force microscopy".
Physical Review B, 2002, **66**(4), 041406.
37. G. Villanueva, F. Perez-Murano, M. Zimmermann, J. Lichtenberg, and J. Bausells
"Piezoresistive cantilevers in a commercial CMOS technology for intermolecular force detection".
Microelectronic Engineering, 2006, **83**(4-9), 1302-1305.
38. J.A. Dagata, F. Perez-Murano, C. Martin, H. Kuramochi, and H. Yokoyama
"Current, charge, and capacitance during scanning probe oxidation of silicon. II. Electrostatic and meniscus forces acting on cantilever bending".
Journal of Applied Physics, 2004, **96**(4), 2393-2399.
39. J.A. Dagata, F. Perez-Murano, C. Martin, H. Kuramochi, and H. Yokoyama
"Current, charge, and capacitance during scanning probe oxidation of silicon. I. Maximum charge density and lateral diffusion".
Journal of Applied Physics, 2004, **96**(4), 2386-2392.
40. H. Kuramochi, K. Ando, Y. Shikakura, M. Yasutake, T. Tokizaki, and H. Yokoyama
"Nano-oxidation and in situ faradaic current detection using dynamic carbon nanotube probes".
Nanotechnology, 2004, **15**(9), 1126-1130.
41. H. Kuramochi, F. Perez-Murano, J.A. Dagata, and H. Yokoyama
"Faradaic current detection during anodic oxidation of the H-passivated p-Si(001) surface with controlled relative humidity".
Nanotechnology, 2004, **15**(3), 297-302.
42. Veeco
"Veeco Instruments Webpage".
<http://www.veeco.com>, 2007.
43. S.F. Lyuksyutov, P.B. Paramonov, R.A. Sharipov, and G. Sigalov
"Induced nanoscale deformations in polymers using atomic force microscopy".
Physical Review B, 2004, **70**(17), -.
44. K. Morimoto, F. Perez-Murano, and J.A. Dagata
"Density variations in scanned probe oxidation".
Applied Surface Science, 2000, **158**(3-4), 205-216.
45. C. Martin, G. Rius, A. Llobera, A. Voigt, G. Gruetzner, and F. Perez-Murano
"Electron beam lithography at 10 keV using an epoxy based high resolution negative resist".
Microelectronic Engineering, 2007, **84**(5-8), 1096-1099.
46. A. Majumdar, P.I. Oden, J.P. Carrejo, L.A. Nagahara, J.J. Graham, and J. Alexander
"Nanometer-scale lithography using the atomic force microscope".
Applied Physics Letters, 1992, **61**(19), 2293-2295.

47. K. Bouzehouane, S. Fusil, M. Bibes, J. Carrey, T. Blon, M. Le Du, P. Seneor, V. Cros, and L. Vila
"Nanolithography based on real-time electrically controlled indentation with an atomic force microscope for nanocontact elaboration".
Nano Letters, 2003, **3**(11), 1599-1602.
48. D.W.M. Arrigan
"Nanoelectrodes, nanoelectrode arrays and their applications".
Analyst, 2004, **129**(12), 1157-1165.
49. J. Wang
"Analytical Electrochemistry".
 Ed. Wiley-VCH, 2001, ISBN: 0471282723.
50. A.J. Bard and L.R. Faulkner
"Electrochemical methods: Fundamentals and Applications".
 Ed. Wiley, 2001, ISBN: 9780471043720.
51. Y.H. Lanyon, G. De Marzi, Y.E. Watson, A.J. Quinn, J.P. Gleeson, G. Redmond, and D.W.M. Arrigan
"Fabrication of nanopore array electrodes by focused ion beam milling".
Analytical Chemistry, 2007, **79**(8), 3048-3055.
52. P. Visconti, A. Della Torre, G. Maruccio, E. D'Amone, A. Bramanti, R. Cingolani, and R. Rinaldi
"The fabrication of sub-10 nm planar electrodes and their use for a molecule-based transistor".
Nanotechnology, 2004, **15**(7), 807-811.
53. P. Visconti, G. Maruccio, E. D'Amone, A. Della Torre, A. Bramanti, R. Cingolani, and R. Rinaldi
"Fabrication of sub-10 nm planar nanotips for transport experiments of biomolecules".
Materials Science & Engineering C-Biomimetic and Supramolecular Systems, 2003, **23**(6-8), 889-892.
54. E. Dubois and J.L. Bubbendorff
"Nanometer scale lithography on silicon, titanium and PMMA resist using scanning probe microscopy".
Solid-State Electronics, 1999, **43**(6), 1085-1089.
55. J.H. Hsu, C.Y. Lin, and H.N. Lin
"Fabrication of metallic nanostructures by atomic force microscopy nanomachining and lift-off process".
Journal of Vacuum Science & Technology B, 2004, **22**(6), 2768-2771.
56. X.N. Xie, H.J. Chung, C.H. Sow, and A.T.S. Wee
"Nanoscale materials patterning and engineering by atomic force microscopy nanolithography".
Materials Science & Engineering R-Reports, 2006, **54**(1-2), 1-48.

Chapter 7. CONCLUSIONS



The main outcome of this Thesis has been the development of new fabrication methods for polymer-based devices using different techniques, and the demonstration of the applications of novel polymers, e.g. doped polymers, in the area of micro- and nano-systems.

It has been demonstrated the processability of different kind of polymeric materials. From the optimization and development of processing methods, it has been shown the feasibility of fabricating devices, including AFM probes, optothermal actuators and nanoelectrodes. In the following, we summarize the main specific results.

Epoxy based resist has been used to fabricate AFM probes using very low cost production technique. The fabrication process flow has been optimized in order to obtain proper and usable probes, i.e. maximizing the fabrication yield and the endurance of the probes, required for an eventual possible commercialization of the product. Two main issues were addressed and solved: tip sharpness and cantilever bent in deflection.

AFM tips are defined from silicon moulds. For obtaining sharp tips, an oxidation process of the moulds at 950°C was found to be optimal, yielding tips radii typically below 20 nm. In order to obtain flat cantilevers, hard bake (120 minutes at 120°C) and release conditions (buffered HF solution for 20 hours) were found to be necessary and optimum for the subsequent performance of the probes. In addition, the initial deflection has been found to be stable during more than one year, proving a long lifetime for the devices.

Finally, characterization of the fabricated AFM probes, in different commercial AFM equipments has proved that they are valid for contact and non-contact mode operation, and the latter both in air and liquid. In addition, obtained AFM images showed that the resolution of the tip compares well with a commercial Si probes.

Epoxy based resist doped with inorganic nanoparticles ($\gamma\text{-Fe}_2\text{O}_3$) was used for the fabrication of AFM probes with enhanced functionality. An increase of the Young's modulus up to 7.5 GPa was observed together with a reduction of the initial deflection angle (below 0.5°) in all the cantilevers, evidencing a reproducible and huge reduction of the intrinsic stress gradient. In addition, the quality factor for the first resonant mode is at least doubled compared to standard epoxy based resist probes. Sharp tips with typical radius below 25 nm were obtained. These probes have been tested for dynamic mode AFM in air and liquid media, resolving similar structures as commercial probes in air and obtaining better results when operating in liquid.

Using an epoxy based resist doped with a black-colored polymer, polyaniline emeraldine base (PANI-EB), opto-thermal actuators were fabricated using one layer of standard epoxy based resist, another layer of PANI-EB doped epoxy based resist and, in some cases, a thin metal layer.

Theoretical calculations were performed taking into account a multi-layer cantilever in order to understand the actuation mechanism when a thermal load is uniformly applied to the structure, when is applied only in a partial region and when a constant power is applied locally.

The experimental results showed that the actuation principle works. Furthermore, using the theoretical calculations to analyze the experimental results it was possible to determine the coefficient of thermal expansion and the thermal conductivity of the doped resists.

Soft lithography has been used to define hydrophobic barriers in a previously fabricated microfluidic network. The network, dedicated to the selective load of an array of cantilevers for dispensing of liquid at the nanoscale, was showing cross-contamination if no barriers were present in between different dispensing holes. After the addition of the barriers, validation tests were performed showing that the barriers avoid cross-contamination and allow a completely selective deposition.

Finally, very low-viscosity epoxy based resist was used to generate submicrometer thick films that can be directly removed with nanometer resolution. Two different mechanism of modification has been identified. The first mechanism is caused by a local electrochemical reaction involving the transport of OH^- ions through the polymer, similar to the situation in AFM local oxidation of anodizable surfaces. This is the dominant mechanism for PMMA and non-exposed epoxy based resists under the application of a voltage between the AFM tip and the surface. The second mechanism was found to be working for exposed and non-exposed films, the application of voltage is not required and it is based on a mechanical indentation. Using this technique, nanoelectrode arrays have been fabricated on gold surfaces with a 30 nm thick resist on top. Preliminary tests show that the insulating properties of the layer are good enough as to perform electrochemistry experiments with the electrodes.

Summing up, the work described in this Thesis represents an advance in the knowledge and use of polymers for micro- and nano- fabrication, given that several techniques have been optimized and developed for different polymers. In addition, the performance of different polymeric devices has been described, showing equivalent behavior than its silicon-based counterpart for the case of AFM probes. In other cases (polymeric hydrophobic barriers, nanoelectrodes, etc.), it has been presented new approaches for specific applications of polymers for micro- and nano- systems. It is expected that all the work performed will serve as a basis for future developments in the field of polymer based MEMS-NEMS.

LIST OF PUBLICATIONS

The following publications have been published in international journals:

1. F. Perez-Murano, C. Martin, N. Barniol, H. Kuramochi, H. Yokoyama, and J.A. Dagata
"Measuring electrical current during scanning probe oxidation".
Applied Physics Letters, 2003, **82**(18), 3086-3088.
2. J.A. Dagata, F. Perez-Murano, C. Martin, H. Kuramochi, and H. Yokoyama
"Current, charge, and capacitance during scanning probe oxidation of silicon. I. Maximum charge density and lateral diffusion".
Journal of Applied Physics, 2004, **96**(4), 2386-2392.
3. J.A. Dagata, F. Perez-Murano, C. Martin, H. Kuramochi, and H. Yokoyama
"Current, charge, and capacitance during scanning probe oxidation of silicon. II. Electrostatic and meniscus forces acting on cantilever bending".
Journal of Applied Physics, 2004, **96**(4), 2393-2399.
4. M. Villarroya, F. Perez-Murano, C. Martin, Z. Davis, A. Boisen, J. Esteve, E. Figueras, J. Montserrat, and N. Barniol
"AFM lithography for the definition of nanometre scale gaps: application to the fabrication of a cantilever-based sensor with electrochemical current detection".
Nanotechnology, 2004, **15**(7), 771-776.
5. C. Martin, G. Rius, X. Borrise, and F. Perez-Murano
"Nanolithography on thin layers of PMMA using atomic force microscopy".
Nanotechnology, 2005, **16**(8), 1016-1022.
6. C. Martin, G. Rius, A. Llobera, A. Voigt, G. Gruetzner, and F. Perez-Murano
"Electron beam lithography at 10 keV using an epoxy based high resolution negative resist".
Microelectronic Engineering, 2007, **84**(5-8), 1096-1099.

7. M. Villarroya, N. Barniol, C. Martin, F. Perez-Murano, J. Esteve, L. Bruchhaus, R. Jede, E. Bourhis, and J. Gierak
"Fabrication of nanogaps for MEMS prototyping using focused ion beam as a lithographic tool and reactive ion etching pattern transfer".
Microelectronic Engineering, 2007, **84**(5-8), 1215-1218.
8. A. Voigt, M. Heinrich, C. Martin, A. Llobera, G. Gruetzner, and F. Perez-Murano
"Improved properties of epoxy nanocomposites for specific applications in the field of MEMS/NEMS".
Microelectronic Engineering, 2007, **84**(5-8), 1075-1079.

The succeeding publications have been accepted for publication in international journals:

9. N. Berthet-Durore, T. Leïchlé, J.B. Pourciel, C. Martin, J. Bausells, E. Lora-Tamayo, F. Perez-Murano, J.M. François, E. Trévisiol, and L. Nicu
"Interaction of biomolecules sequentially deposited at the same location using a microcantilever-based spotter".
Biomedical Microdevices, 2008.
10. C. Martin, A. Llobera, T. Leïchlé, G. Villanueva, A. Voigt, V. Fakhfour, J.Y. Kim, N. Berthet, G. Gruetzner, L. Nicu, J. Brugger, and F. Perez-Murano
"Novel Methods to pattern polymers for microfluidics".
Microelectronic Engineering, 2008.

ABSTRACT

Polymers have been gaining interest for microengineering because they offer a fast, flexible and low-cost alternative of producing Micro/Nanosystems, substituting silicon as a structural material. In addition, they can be doped, acquiring new functionalities and properties, which improves their performance for device manufacturing. Chemically amplified epoxy based negative resists, e.g. SU-8, is an



example of material to fabricate polymer-based micro/nano systems. Epoxy based resist devices can be fabricated by a combination of multi-layer spin-coating, molding and lithographic processing of the resist. This Thesis comprises the establishment of polymer MEMS technology processing at the CNM-IMB-CSIC and the fabrication and characterization of AFM probes either using non-doped (standard) or a doped version with iron oxide nanoparticles to overcome their operation and performance. In addition, by doping the epoxy based resist with a black-colored polymer, the absorption spectrum has been modified giving the possibility to use this new material for optothermal actuators. A specific form of the epoxy based resist has been used for the fabrication of hydrophobic barriers, useful in microfluidics to avoid the intermixing of liquids in a network. Finally, obtaining extremely thin polymer layers by decreasing its viscosity makes possible its local modification by AFM, improving the resolution of the patterning.